FUNDAMENTAL STUDY OF THE FABRICATION OF ZINC OXIDE NANOWIRES AND ITS DYE-SENSITIZED SOLAR CELL APPLICATIONS

A Dissertation
Presented to
The Academic Faculty

by

Mallarie DeShea McCune

In Partial Fulfillment
of the Requirements for the Degree
Doctor of Philosophy in the
School of Chemical and Biomolecular Engineering

Georgia Institute of Technology
August 2012

FUNDAMENTAL STUDY OF THE FABRICATION OF ZINC OXIDE NANOWIRES AND ITS DYE-SENSITIZED SOLAR CELL APPLICATIONS

Approved by:

Dr. Yulin Deng, Advisor
School of Chemical & Biomolecular Engineering
Georgia Institute of Technology

Dr. Sue Ann Bidstrup Allen
School of Chemical & Biomolecular Engineering
Georgia Institute of Technology

Dr. Tom Fuller
School of Chemical & Biomolecular Engineering
Georgia Institute of Technology

Dr. Preet Singh
School of Materials Science & Engineering
Georgia Institute of Technology

Dr. Zhong Lin Wang
School of Materials Science & Engineering
Georgia Institute of Technology

Date Approved: May 3, 2012

To my wonderful parents, Albert & Linda McCune, for their love and support

ACKNOWLEDGEMENTS

I would first like to thank my advisor, Professor Yulin Deng, for providing strong academic and research guidance as well as outstanding mentorship during my time at Georgia Tech. Additionally, I want to acknowledge my thesis committee members, Professor Sue Ann Bidstrup Allen, Professor Tom Fuller, Professor Preet Singh, and Professor Zhong Lin Wang for helping me to establish an advanced chemical engineering foundation through their course offerings as well providing advice on my thesis. I would also like to thank several of my former and current group members that I've collaborated with including Dr. Zeshan Hu, Yinhua Li, Xihong Zu, Wenji Zhang, Wei Mu, Wei Zhang, Xiaodan Zhang, and Zhengzhi Zhou. I would also like to recognize all of the members of the Yulin Deng group from 2007-2012, who have provided me with strong support and advice continuously. I would like to acknowledge my undergraduate student, Nadia Wilf, who brought enthusiasm and valuable insight to the lab each time I asked her to assist me with a project.

I would like to acknowledge Dr. Cornelia Gillyard, my Spelman College advisor, for all of the mentoring, teaching, and support she has given me along the way.

I would especially like to thank my parents, Albert and Linda McCune, for their tireless support during my entire academic matriculation. They have provided me with encouragement and motivation to excel in school no matter how daunting the challenges seemed. Lastly, I want to thank my brother, Keshun McCune, and other family members, friends, and fellow graduate students who gave incredible support, encouraging words, and tons of laughter during my graduate studies.

TABLE OF CONTENTS

	Page
ACKNOWLEDGEMENTS	iv
LIST OF TABLES	viii
LIST OF FIGURES	x
LIST OF ABBREVIATIONS	xvii
LIST OF SYMBOLS	xix
SUMMARY	xxi
CHAPTER 1: INTRODUCTION	1
1.1 Thesis Motivation	1
1.2 Thesis Overview	5
CHAPTER 2: LITERATURE REVIEW	6
2.1 Zinc Oxide	6
2.1.1 Zinc Oxide Properties	6
2.1.2 Zinc Oxide Crystal Structure	8
2.2 Zinc Oxide Nanomaterials	9
2.2.1 Synthesis Techniques for Zinc Oxide Nanowires	9
2.2.2 Morphology Control of Zinc Oxide Nanostructures from Aqueous Solution	14
2.3 Photovoltaic Principles and Concepts	22
2.3.1 History of Photovoltaics	22

2.3.2 Principles of Dye-Sensitized Solar Cells 27

2.3.3 Characterization of Dye-Sensitized Solar Cells 33

2.3.4 Factors that Govern the Performance of Dye-Sensitized Solar Cells 35

2.4 Thesis Hypotheses 40

2.5 Thesis Objectives 41

CHAPTER 3: FABRICATION OF ZINC OXIDE NANOWIRES 42

3.1 Introduction 42

3.2 Fabrication Procedure 46

3.3 Zinc Oxide Nanowire Synthesis and Characterization Results 49

3.4 Brief Summary 57

CHAPTER 4: MATHEMATICAL MODEL FOR ZINC OXIDE NANOWIRE DYE-SENSITIZED SOLAR CELLS 58

4.1 Introduction 58

4.2 Device Geometry and Modeling Physics 61

4.3 Model Results and Discussion 69

4.4 Brief Summary 82

CHAPTER 5: ZINC OXIDE NANOWIRE DYE-SENSITIZED SOLAR CELL DESIGNS FOR ENHANCED PERFORMANCE 84

5.1 Block Layer Zinc Oxide Nanowire Dye-Sensitized Solar Cell Design 84

5.1.1 Introduction 84

5.1.2 Experimental Procedure 90

5.1.3 Experimental Results and Characterization 95

5.1.4 Brief Summary 102

5.2 Three-Dimensional Zinc Oxide Nanowire Dye-Sensitized Solar Cell Designs 103

5.2.1 Introduction 103

5.2.2 Experimental Procedure 107

5.2.3 Experimental Results and Characterization 108

5.2.4 Brief Summary 118

5.3 Ultra Dense Hierarchal Design of Zinc Oxide Nanowire Dye-Sensitized Solar Cells 119

5.3.1 Introduction 119

5.3.2 Experimental Procedure 124

5.3.3 Experimental Results and Characterization 127

5.3.4 Brief Summary 139

CONCLUSIONS 140

APPENDIX A: ADSORBED N719 DYE CONCENTRATION 143

REFERENCES 146

VITA 156

LIST OF TABLES

Page

Table 2.1	Summary of Different Results and Methods for Aqueous Solution Growth	17
Table 2.2	Effect of the Reactant Concentrations on the Morphology of Zinc Oxide Particles (from Zinc Nitrate Solution)	18
Table 2.3	Effect of the Reactant Concentrations on the Morphology of Zinc Oxide Particles (from Zinc Chloride Solution)	18
Table 2.4	Operation parameters of ZnO-based DSSCs made with different photelectrodes	39
Table 3.1	Analysis of 1D ZnO NW Array at 10 mM Precursor Concentration	53
Table 3.2	Analysis of 1D ZnO NW Array at 25 mM Precursor Concentration	53
Table 4.1	Constant Model Parameters	69
Table 4.2	Case I Model Results of DSSC performance characteristics at varying lengths of the ZnO nanowires with the radius and density set constant to 50 nm and 1 x 10^9 /cm^2 of projected surface area, respectively	71
Table 5.1	Physical Characteristics of ZnO NW used in DSSC and its Photovoltaic Characteristics	96
Table 5.2	Photovoltaic Characteristics of ZnO NW based DSSCs incorporating Block Layers	101
Table 5.3	Photovoltaic Characteristics of DSSCs based on layers of flower-like ZnO NW arrays	110
Table 5.4	Photovoltaic characteristics of DSSCs based on 5 layers of ZnO NWs using different equimolar concentrations of Zinc Nitrate Hexahydrate and HMTA	113
Table 5.5	Photovoltaic characteristics comparison of DSSCs based on 5 layers of ZnO NWs using 50 mM equimolar concentrations of Zinc Nitrate Hexahydrate and HMTA that are with or without the BL	115
Table 5.6	ZnO NW Characteristic Data	116

Table 5.7 Photovoltaic Characteristics of multilayered NW arrays grown using LBL method with electrospun ZnO NF as seed and a 50 mM precursor solution 136

Table 5.8 Photovoltaic Characteristics of multilayered NW arrays grown using LBL method with electrospun ZnO NF as seed and a 75 mM precursor solution 137

LIST OF FIGURES

Page

Figure 2.1 Stick and ball representation of ZnO crystal structures: (a) cubic rocksalt (*B*1), (b) cubic zinc blende (*B*3), and (c) hexagonal wurtzite (*B*4). The shaded gray and black spheres denote Zn and O atoms, respectively 8

Figure 2.2 (a) SEM image of aligned ZnO nanowires grown on sapphire substrate using a thin layer of gold as catalyst. (b) SEM images of gold catalyst patterns using PS sphere monolayer as mask. (c) SEM image of aligned ZnO nanowires grown with a honeycomb pattern 10

Figure 2.3 SEM images of ZnO nanorods formed on sapphire (0001) substrates. (a) Images observed from a cleaved surface. (b) Images taken with a tilt angle. (c) Image of the top of a single ZnO nanorods 12

Figure 2.4 SEM image of the hydrothermally grown ZnO nanowires was taken at a 45° tilt. The inset is the top-view SEM image 14

Figure 2.5 Relationship between supersaturation in deposition baths, rate of crystal growth and morphology 15

Figure 2.6 SEM images of ZnO films from aqueous solution (25mM Zinc Acetate and 25mM HMTA, pH 5, 90 °C, 1 hour) on a) Au-coated TO(F) glass; b) ZnO template layers on TO(F) glass; c) TO(F) glass; and d) crystalline (0001) sapphire 16

Figure 2.7 SEM of ZnO crystal structures obtained at 100°C after 30min of ageing from: (a) 20 mM $ZnC1_2$- 50 mM HMT to produce the needle shape; (b) 50 mM $Zn(NO_3)_2$ -50 mM HMT to produce the prism shape 19

Figure 2.8 Comparison of wire growth by using the preferential growth process developed in this study and the bulk liquid-phase deposition method reported in the literature. The wire length is plotted as a function of growth time at different growth conditions 21

Figure 2.9 SEM images of arrays of ZnO nanowires in varied lengths via a preferential growth method. Scale bar, 10 μm. Wire length (a) 11 μm, (b) 17 μm, (c) 22 μm, (d) 27 μm, (e) 33 μm 21

Figure 2.10 (a) Schematic cell design with crystalline n-Si NW core in brown, the polycrystalline p-Si shell in blue, and the back contact in black. (b) Cross-sectional SEM of vertically aligned NWs used in the device 24

Figure 2.11 Best researched solar cell energy conversion efficiencies from 1976-2011(from National Renewable Energy Laboratory (USA)) 26

Figure 2.12 Schematic illustrating the operation principle of DSSCs 29

Figure 2.13 Functional diagram of DSSC illustrating 8 fundamental processes 30

Figure 2.14 Illustration of a ZnO nanowire-based DSSC 31

Figure 2.15 (Left) Standard I-V curve used to determine η after inverting the raw data 34

Figure 2.16 UV-Vis absorption spectrum of N719 in 1:1 acetonitrile and tert-butanol. The inset shows the molecular structure of N719 36

Figure 2.17 The effect of ZnO film thickness on the DSSC efficiency for ZnO films sensitized with Rose Bengal and with Rhodamine B 38

Figure 2.18 IPCE spectra of ZnO-based DSSCs annealed at different temperatures 39

Figure 3.1 Schematic showing role of hexamethylenetetramine as a capping agent to promote 1-D growth 43

Figure 3.2 Density varied with concentration. (Circle) Plot of ZnO nanowire density in a 100 mm^2 area; (Triangle) Plot of area percentage covered by ZnO nanowires. Each data point was obtained from 4 different areas. Inset is a typical image of ZnO nanowires grown at 5 mM 44

Figure 3.3 Image of P-6000 Spin Coater (Technologies Integrated, Inc.) 47

Figure 3.4 Schematic of synthesis setup 47

Figure 3.5 Solution-based synthesis vessel consisting of 50 mL Pyrex bottle filled with precursor solution 48

Figure 3.6 (Left) Vacuum Oven (1400E, VWR Scientific); (Right) Muffle Furnace (Fischer Scientific) 48

Figure 3.7 a) SEM images of ZnO nanostructures; b) close up SEM image of same ZnO nanostructures 50

Figure 3.8 SEM images of 1D ZnO NW array. a) 10 mM @ 70°C for 24h on Si substrate using 4 coats of seed layer solution; b) 10 mM @ 70°C for 24h on Si substrate using 6 coats of seed layer solution 51

Figure 3.9 SEM images of 1D ZnO NW array. a) 10 mM @ 80°C for 12h on FTO substrate using 4 seed layers; b) 10 mM @ 80°C for 12h on FTO substrate using 6 seed layers 52

Figure 3.10 SEM images of 1D ZnO NW array. a) 25 mM @ 90°C on FTO substrate using 5 seed layers for 12.5h (refreshing the growth solution every 2.5h); b) 25 mM @ 90°C on FTO substrate using 5 seed layers for 12.5h in the same growth solution 55

Figure 3.11 XRD spectrum of 1D ZnO nanowire sample 56

Figure 4.1 Illustration of a certain film thickness, d, of ZnO nanowires on the glass substrate and electron diffusion processes of the DSSC 61

Figure 4.2 Illustration of the ZnO nanowire array-based DSSCs 62

Figure 4.3 Schematic of nanowire dimensions to calculate surface area 64

Figure 4.4 Effect of length of the ZnO nanowires on the IPCE of the DSSC at constant radius of 50 nm and constant density of $1x10^9$ /cm^2 of projected surface area (or ~10% surface coverage) 70

Figure 4.5 Effect of length of the ZnO nanowires on the IPCE of the DSSC at a constant density of $3x10^9$ /cm^2 of projected surface area and varying constant radii 73

Figure 4.6 Effect of length of the ZnO nanowires on the IPCE of the DSSC at a constant radius of 50 nm and varying densities 74

Figure 4.7 Effect of length of the ZnO nanowires on the IPCE of the DSSC at a constant radius of 50 nm and constant density of 1 $x10^9$ /cm^2 of projected surface area for different dye loadings 75

Figure 4.8 Effect of length of the ZnO nanowires on the IPCE of the DSSC at a constant radius of 50 nm and constant density of 1 $x10^9$ /cm^2 of projected surface area 76

Figure 4.9 Schematic of dye molecules absorbing various degrees of light based on its distance from the light source 81

Figure 5.1 Schematic of ideal process in traditional DSSCs based on 1D ZnO nanowires 85

Figure 5.2 Illustration demonstrating the major drawback of a traditional DSSC based on 1D ZnO nanowires 86

Figure 5.3 Schematic demonstrating the use of a block layer as a solution to minimize electron back transfer in the traditional DSSC based on 1D ZnO nanowires 87

Figure 5.4 Schematic illustration of the nanoring array fabrication using a PS-b-P4VP block copolymer thin film as a template 88

Figure 5.5 (Left) AFM image of the PS-b-P4VP film before methanol vapor treatment; (Middle) 3D AFM image of the PS-b-P4VP film exposed to the vapor of methanol at 40°C for 2h (500 nm x 500 nm); (Right) SEM image of ZnO nanoring arrays by using PS-b-P4VP block copolymer thin film as a template (scale bar = 100 nm) 89

Figure 5.6 Schematic illustration of the experimental process of applying the polymer block layer based on the PS-b-P4VP diblock copolymer 91

Figure 5.7 Schematic of homemade apparatus for the spray pyrolysis of TAA to form TiO_2 block layer 92

Figure 5.8 (Top) Solar Cell; (Middle) Characterization System; (Bottom) Experimental Apparatus with SoLux Solar Simulator 94

Figure 5.9 J-V curve of DSSC based on an unmodified assembly of 1D ZnO NW array using 25 mM equimolar concentrations of Zinc Nitrate Hexahydrate and HMTA 95

Figure 5.10 SEM image of ZnO nanowires grown from on seed layer sites with the PS polymer block layer 97

Figure 5.11 SEM image of TiO_2 BL 97

Figure 5.12 SEM images of ZnO NWs grown on TiO_2 BL coated FTO substrates. a) zoomed out image; b) zoomed in image; c) zoomed in image of NWs on BL surface; d) zoomed in image of NWs on FTO surface 99

Figure 5.13 J-V curves of DSSCs based on 1D ZnO NW arrays incorporating block layers. (Pink) TiO_2/P4VP BL; (Blue) TiO_2 BL; (Orange) PS Polymer BL 100

Figure 5.14 Illustration displaying the transforming of a 1D ZnO NW array to a 3D ZnO NW array 104

Figure 5.15 (a) Cross-sectional SEM image and (b) optical image of NW arrays on a 2 in. p-type Si wafer (etched for 5 min). (c) 45° view SEM micrographs of the ZnO/Si branched nanowire heterostructures at low magnification. (d) 89° view and (e) top view SEM micrographs of the ZnO/ Si branched nanowire heterostructures at high magnification. (f) LR-TEM image on a single Si/ZnO branched NW. (g) 45° view SEM image of a photodetector device with top ITO contact 105

Figure 5.16 Schematic LBL growth procedure of 1D ZnO NWs into 3D ZnO NWs 106

Figure 5.17 SEM images of 3D ZnO NW arrays. a) 2 layers; b) 3 layers; c) 4 layers 109

Figure 5.18 J-V curves of devices prepared with different numbers of ZnO nanowire array layers using 25 mM equimolar concentrations of Zinc Nitrate Hexahydrate and HMTA 110

Figure 5.19 Dependence of overall power conversion efficiency with different numbers of ZnO nanowire array layers using 25 mM equimolar concentrations of Zinc Nitrate Hexahydrate and HMTA 111

Figure 5.20 SEM images of 5 layered ZnO NW arrays. a) 25 mM equimolar precursor solution concentration; b) 50 mM equimolar precursor solution concentration 112

Figure 5.21 J-V curves of devices prepared using 5 layers of ZnO nanowire arrays using various equimolar concentrations of Zinc Nitrate Hexahydrate and HMTA.(Blue) 25 mM; (Pink) 50 mM 113

Figure 5.22 SEM image of 5 layered ZnO NW arrays using 50 mM equimolar precursor solution concentration with the hybrid TiO_2/P4VP block layer 114

Figure 5.23 J-V curves of devices prepared using 5 layers of ZnO nanowire arrays using 50 mM equimolar concentrations of Zinc Nitrate Hexahydrate and HMTA. (Blue) without the BL; (Pink) with the TiO_2 BL; (Green) with the TiO_2/P4VP BL 115

Figure 5.24 Schematic process for synthesizing a two-layer assembly of ZnO NW arrays on transparent conducting oxide, green represents NWs and pink represents SAM 120

Figure 5.25 SEM images. (a) First layer ZnO NW array, scale bar 10 μm; inset-optical image of a water droplet on the array after it was coated with a SAM; (b) Two-layer assembly of ZnO NW arrays, scale bar 10 μm; (c) Junction between the first and second layer of ZnO NWs, scale bar 500 nm 120

Figure 5.26 Schematic of Hierarchal ZnO Nanoforest and SEM of the ZnO Nanoforest 121

Figure 5.27 (Top) Schematic displaying limitations with using the spin coating method to reapply ZnO seeds to form subsequent layers of ZnO NW array; (Bottom) SEM image of large crystal seeds clustered on NW sidewalls 122

Figure 5.28 Schematic of design process for ultra dense multilayers of ZnO NW arrays via the electrospinning of ZnO nanofiber seeds 123

Figure 5.29 Schematic illustration for the electrospinning apparatus used in the fabrication of ZnO nanofibers 125

Figure 5.30 Setup for Electrospinning ZnO nanofiber seed layers 125

Figure 5.31 Images of the ZnO NF. (a) Microscopic image before calcination at 600°C; (b) SEM image after calcination at 600°C 127

Figure 5.32 SEM images of one layer of ZnO NW arrays grown on electrospun ZnO NF as seed at various magnifications. a) 186 X magnification; b) 695 X; c) 3.09K X; d) 9.41K X 128

Figure 5.33 SEM image of the 2 layers of ZnO NW arrays grown using LBL method with electrospun ZnO NF as seed 129

Figure 5.34 SEM images of 2 layer-branched ZnO NWs. a) Side view; b) top view 129

Figure 5.35 SEM images of 3D "caterpillar-like" ZnO NWs grown from ZnO NF seeds. (a) view of 3 layers of multiple "caterpillar-like" ZnO NW structures; (b) close up view of NWs grown from NF seeds to form "caterpillar-like" structure 130

Figure 5.36 a) 1D ZnO NW array with density ~2 x10^{9}/cm^{2} and diameter ~90 nm; b) 3D ZnO NW array with density ~1 x10^{11}/cm^{2} and diameter ~50 nm 131

Figure 5.37 SEM images of 4 layers of ZnO NWs grown from ZnO NF seeds. a) front view; b) side view; c) side view tilted at 60° 132

Figure 5.38 SEM images of 5 layers of ZnO NWs grown from ZnO NF seeds at various magnifications. a) 900 X magnification; b) 2.03K X; c) 2.81K X; d) 3.57K X 133

Figure 5.39 XRD spectrum of 3D multilayered array of ZnO nanowires 134

Figure 5.40 J-V curves of multilayered NW arrays grown using LBL method with electrospun ZnO NF as seed and a 50 mM precursor solution 136

Figure 5.41 J-V curves of multilayered NW arrays grown using LBL method with electrospun ZnO NF as seed and a 75 mM precursor solution 137

Figure A.1 Absorbance spectra for N719 dye samples 143

Figure A.2 Calibration curve for N719 dye samples at 515 nm along with the best fit curve 144

LIST OF ABBREVIATIONS

AFM	Atomic Force Microscope
BL	Block Layer
CNT	Carbon Nanotube
DC	Direct Current
DSSC	Dye-Sensitized Solar Cell
FE	Field Emission
FTO	Fluorine Tin Oxide
HMTA or HMT	Hexamethylenetetramine
ITO	Indium Tin Oxide
LBL	Layer-By-Layer
NF	Nanofiber
NP	Nanoparticle
NW	Nanowire
PEDOT	Poly(3,4-ethylenedioxythiophene)
PEG	Polyethylene Glycol
PL	Photoluminescence
PS	Polystyrene
PSS	Poly(styrenesulfonate)
PVC	Polyvinylchloride
P4VP	Polyvinyl4-pyridine
Pt	Platinum
PVP	Polyvinylpyrrolidone
SC	Solar Cell

SAM	Self-Assembled Monolayer
SEM	Scanning Electron Microscope
SS	Supersaturation
TAA	Di-iso-propoxy titanium bis(acetylacetonate)
UV	Ultra-Violet
XRD	X-ray Diffraction
ZnO	Zinc Oxide

LIST OF SYMBOLS

α	light absorption coefficient [cm^{-1}]
β	Ideality Factor or Field Enhancement Factor [dimensionless]
ε	Molar Extinction Coefficient [$M^{-1}cm^{-1}$]
η	Overall Power Conversion Efficiency [%]
n_c	Charge Collection Efficiency [%]
λ	Wavelength [nm]
σ	absorption cross section [cm^2/mol]
τ	Excited–State Electron Lifetime [s]
τ_{IMPS}	Intensity Modulated Photocurrent Spectroscopy Time Constant [s]
ϕ	Porosity [dimensionless]
Φ	Work Function [eV]
ϕ_{inj}	Electron Injection Efficiency [%]
ω	Circular Frequency of the Light Modulation [cycles/s]
Γ	mol dye per projected surface area [mol/cm^2]
k_{inj}	Rate Constant for Electron Injection [s^{-1}]
k_r	Rate Constant for Recombination [s^{-1}]
n	Total Electron Density [cm^{-3}]
n_{cb}	Electron Density in Conduction Band[cm^{-3}]
n_t	Electron Density in Trap States [cm^{-3}]
m	Ratio of n_{cb}/n [dimensionless]
q	Electron Charge [C]
r	Nanowire Radius [cm]
d	Film Thickness [cm]

APCE	Absorbed Photon-Current-Efficiency [%]
A_a	Active Area [cm^2]
A_{array}	Surface Area of Nanowire Array [cm^2]
A_{NW}	Surface Area of Nanowire [cm^2]
D_{cb}	Electron Diffusion Coefficient [cm^2/s]
E	Macroscopically Applied Electric Field [V/cm]
FF	Fill Factor [dimensionless]
IPCE	Incident Photon-To-Electron Conversion Efficiency [%]
I	Current [A]
I_o	Incident Photon Flux [$cm^{-2}s^{-1}$]
J	Current Density [A/m^2]
J_{MP}	Current Density at Maximum Power [A/cm^2]
J_{sc}	Short Circuit Current Density [A/cm^2]
L	Electron Diffusion Length [cm]
LHE	Light Harvesting Efficiency [%]
N	Density of Nanowires [number of wires/cm^2]
P_{in}	Input Power [mW/cm^2]
R	Resistance [Ω]
R_{SH}	Shunt Resistance [Ω cm^2]
V	Voltage [V]
V_{NW}	Nanowire Volume [cm^3]
V_{MP}	Voltage at Maximum Power [V]
V_{oc}	Open Circuit Voltage [V]

SUMMARY

Because of its excellent and unique physical properties, ZnO nanowires have been widely used in numerous scientific fields such as sensors, solar cells, nanogenerators, etc. Although it is believed that single crystal ZnO has a much higher electron transfer rate than TiO_2, it was found that ZnO nanowire-based dye-sensitized solar cells (DSSCs) have lower efficiencies than TiO_2 nanoparticle-based DSSCs because the density and surface area of ZnO nanowires are usually lower than that of TiO_2 nanoparticles, limiting the cell's light absorption, and because the open-root structure of ZnO nanowires results in electron back transfer that causes charge shortage of the cell. Here, experimental studies were performed that utilize strategic manipulations of the design of the ZnO nanowire based DSSCs in efforts to address and solve its key challenges. It was shown that by incorporating various blocking layers into the design of the cell, the performance of the DSSC can be improved. Specifically, by placing a hybrid blocking layer of TiO_2-P4VP polymer between the substrate and the ZnO nanowires, the conversion efficiency of the cell is 43 times higher than that of a cell without this blocking layer due to the reduction of electron back transfer. Furthermore, in efforts to improve the surface area of the ZnO nanowire array, unique three dimensional structures of ZnO nanowires were fabricated. It was found that by significantly improving the overall density and surface area of the ZnO nanowire array through distinctive hierarchal nanowire structures, the light harvesting efficiency and electron transport were enhanced allowing the DSSC to reach 5.20%, the highest reported value for 3D ZnO NW based DSSCs. Additionally, the development of a theoretical model was explored in efforts to investigate how the geometry of ZnO nanowires affects the incident photon-to-current conversion efficiency of 1D ZnO nanowire-based N719-sensitized solar cells at the maximum absorption wavelength of 543 nm.

CHAPTER 1

INTRODUCTION

1.1 Thesis Motivation

Recently, there has been an increasing concern regarding the international energy crisis and many researchers and politicians have acknowledged that the mismatch between the energy demand and energy supply is the most challenging issue that our planet faces today. Richard Smalley, the 1996 recipient of the Noble Prize in Chemistry, will be remembered most for his commitment to increasing global awareness about the terawatt challenge. The term "terawatt challenge" comes from the astounding statistic of 2004, in which the world used approximately 220 million barrels of oil per day (i.e., approximately 14.5 terawatts (TW)) of energy in one single year [1, 2]. Most of this consumed energy came from the use of oil, coal, and gas which leads to significant environmental concerns with the high levels of CO_2 emissions into the air. It is predicted that the world energy needs will increase at an annual rate of 2%; therefore there has to be a collective effort to provide an annual production of energy that is twice the demand using renewable sources of energy [2, 3].

Today, investing in renewable energy sources has been at the forefront of scientific and political conversions. Moreover, solar energy is the most abundant renewable energy source that we have with its continuous supply of about 1.2×10^5 TW from the sun to planet Earth [4]. In fact, the sun delivers 4.6×10^{20} Joules of energy to Earth in one single hour, which equals the annual rate of world energy consumption [4]. In 2007 at the Materials Research Society Meeting in San Francisco, Nate Lewis acknowledged the fact that six land farms of solar cells with 10% efficiency supplying about 3.3 TW of energy could be strategically placed around the world to adequately supply the current global energy needs [5]. However, this large scale project would

undoubtedly be too costly since it would require an average of $0.30 per kilowatt-hour for this solar technology [5]. Yielding to the teachings of Smalley and Lewis, many researchers around the globe have dedicated much time to investigating ways to make renewable energy sources economically feasible. Before his death in 2005, Smalley declared that "innovations in nanotechnology and other advances in materials science would make it possible to transform our vision of plentiful, low-cost energy into a reality [2]."

In particular, dye-sensitized solar cells of the third generation of solar cells have become a very interesting and practical alternative for advances in solar cell technology. The working mechanism of the dye-sensitized solar cell is unique in that it does not follow the principles of the traditional p-n junction solar cell. The dye sensitizer absorbs the photons, while the role of the semiconductor film is to facilitate charge transport to the collecting transparent conductive oxide glass substrate. Since its introduction into the science community in 1991, the nanocrystalline photoanode in dye-sensitized solar cells have predominantly been comprised of titanium (TiO_2) nanoparticles. With efficiencies reaching a plateau of 11-12% for TiO_2 nanoparticle-based dye sensitized solar cells [6, 7], many researchers became very interested in studying the dye-sensitized solar cell performance of alternative semiconducting nanomaterials. Specifically, Zinc Oxide (ZnO) has been an ideal alternative to TiO_2 because ZnO has a similar conduction band edge that is appropriate for proper electron injection from the excited dyes; moreover, ZnO provides better electron transport due to its higher electronic mobility [8].

Over the past decade, there has been a heightened interest in using ZnO nanowires as the semiconducting photoanode in dye-sensitized solar cells. Utilizing wide-band gap semiconductor nanowires (e.g., ZnO nanowires) instead of TiO_2 nanoparticles has been thought to be very advantageous because i) the nanowire morphology allows for electrons to travel a more direct

conduction path from the point of injection to the point of collection, and ii) the nanowires possess a large enough surface area for adequate dye adsorption [9]. The nanowire photoanode has a very fast electron injection rate and the electron diffusivity in crystalline wires (specifically ZnO nanowires) has been reported as several orders of magnitude larger than electron diffusivity within TiO_2 nanoparticles [10-13]. The superior electron transport within the nanowire photoanode can be attributed to its higher crystallinity and the presence of an internal electric field that facilitates electron transport to the collecting glass substrate by effectively separating the injected electrons from the oxidized species of the electrolyte; this, in turn, improves the charge collection efficiency [10]. Furthermore, nanowires can be synthesized at low temperatures, which allow the use of various substrates including polymers, and the employment of low temperatures greatly reduces energy costs. However, researchers have yet to fabricate ZnO nanowire-based DSSCs with efficiencies similar or higher than TiO_2 nanoparticle-based DSSCs. Although the vertical nanowire morphology has many advantages, there is also a critical disadvantage. Compared to the closely packed nanoparticle thin film, more uncovered substrate surface between the nanowires is present in the vertical nanowire array. These open spaces lead to direct contact between the electrons at the conducting glass substrate and either the oxidized dye molecules or oxidized species in the electrolyte during the charge transport process. This phenomenon is known as either electron recombination or electron back transfer. Interestingly, many have referred to the occurrence of electron back transfer as the most crucial limitation of dye sensitized solar cells as it severely affects its performance by short-circuiting the cell. It is thought that by placing a barrier layer between the conducting glass substrate and the nanowires, the contact at the conducting substrate-electrolyte interface can be significantly reduced or avoided completely.

Another major challenge of ZnO nanowire-based dye sensitized solar cells stems from the lower surface area of the ZnO nanowire array to that of the network of TiO_2 nanoparticles on the substrate. By having a larger surface area, the nanocrystalline photoanode is able to absorb a greater amount of the incoming light. Thus, improvements in the surface area of the ZnO NW array used for the dye-sensitized solar cell will significantly enhance the light harvesting efficiency, which in turn results in an overall increase in the power conversion efficiency of the cell. In addition to providing better charge collection, the use of very long and dense ZnO nanowire arrays results in a greater surface area that is necessary for an increase of adsorbed dye molecules, which leads to improved light harvest efficiency [10]. As an alternative to synthesizing longer nanowires, the concept of producing dense hierarchal nanowire structures should also yield larger surface areas needed to improve the conversion efficiency of ZnO nanowire-based dye-sensitized solar cells.

1.2 Thesis Overview

The following is a general outline of this thesis. Chapter 2 will provide an extensive literature review that will serve as a guide for understanding the following chapters. This detailed review will be based primarily on i) the properties, characteristics, and attractive uses of ZnO and its nanomaterials; and ii) the fundamental principles of photovoltaics and particularly advancements of dye-sensitized solar cells within the nanotechnology field. Chapter 3 will focus on i) the fabrication of ZnO nanowires based on a hydrothermal process synthesis; and ii) an investigative study of ZnO morphology based on varied synthesis conditions. Chapter 4 will discuss in detail a mathematical model that approximates the incident photon-to-current conversion efficiencies of 1D ZnO nanowire-based dye-sensitized solar cells under various conditions. Chapter 5 will examine various methodologies to improve the overall power conversion efficiencies of ZnO nanowire-based dye-sensitized solar cells via i) a blocking layer incorporated into the solar cell design; and ii) the fabrication of a three-dimensional solar cell design. Lastly, Chapter 6 will then conclude all major findings and rationalizations from this research project.

CHAPTER 2

LITERATURE REVIEW

2.1 Zinc Oxide

2.1.1 Zinc Oxide Properties

Zinc Oxide (ZnO) is an inorganic binary compound belonging to the II-VI semiconductor materials group. Because of its many unique qualities, there has been an overwhelming amount of research studies dedicated to ZnO and its applications in a wide arrange of scientific fields [14]. One of the most attractive properties of this semiconductor is its wide bandgap of ~3.37 eV at room temperature. A semiconducting material with a wide band gap has the ability to be effective during processes at high temperature and power, and also with operations applying large electric fields [15]. Moreover, there has been a recent interest in the field emission characteristics of ZnO. Researchers believe that ZnO nanomaterials are desirable electron emitters because, like carbon nanotubes (CNT), they have large aspect ratios that can attain high electric fields at the tips of the nanostructure for electron emission under conditions of reasonable applied voltages [16]. ZnO nanostructures also have turn-on and threshold field values comparable to CNTs as well. The turn-on field and the threshold field are defined as the macroscopic fields required to produce a current density of 10 $\mu A/cm^2$ and 10 mA/cm^2, respectively [17]. The emission current density can be evaluated by applying Equation 2.1, the Fowler-Nordheim equation [17]:

$$J = \left({}^{AE^2\beta^2}\!/_{\Phi} \right) \exp\left(-B\Phi^{\frac{3}{2}} \Big/ {}_{\beta E} \right) \ , \qquad \textbf{(2.1)}$$

where J is the emission current density (A/cm^2), E is the macroscopically applied electric field in V/cm, and β is the field enhancement factor, A and B are both constants with values of 1.56×10^{10} ($A \cdot V^{-2} \cdot eV$) and 6.83×10^3 ($V \cdot eV^{-3/2} \cdot \mu m^{-1}$), respectively, and Φ is the emitter work function, which is around 5.4 eV for ZnO [17].

Other desirable characteristics of ZnO include its near UV emission, large exciton binding energy around 60 meV that allows sufficient excitonic emission within the UV range at 298K, visible light transparency, transparent conductivity and piezoelectricity, biocompatibility, structure and property controllability, and simplicity of synthesis process [14, 16]. Some of the many applications that utilize the distinctive properties of ZnO (particular ZnO nanowires) include sensors [18-21], UV photodetectors [22-26], light-emitting device arrays [27], field-effect transistors [28], p-n junction diodes [29], Schottky diodes [30], optoelectronic nanocircuits [31], dye-sensitized solar cells [32], biomedical sciences [33, 34], and spintronics [35].

2.1.2 Zinc Oxide Crystal Structure

ZnO can take on three of the following crystal structures: wurtzite (*B*4), zinc blende (*B*3), and rocksalt (*B*1), as schematically shown in Figure 2.1 [15]. ZnO crystallizes into the rocksalt (NaCl) structure at relatively high pressures, while the zinc blende ZnO structure exists only upon growth on substrates with the proper cubic lattice [15]. The most thermodynamically stable structure for ZnO, however, is the wurtzite structure. The wurtzite structure has a hexagonal unit cell with space group C6mc and lattice parameters a = 0.3296, and c = 0.52065 nm, where the O^{2-} and the Zn^{2+} create alternating planes of tetrahedral coordinated units [14].

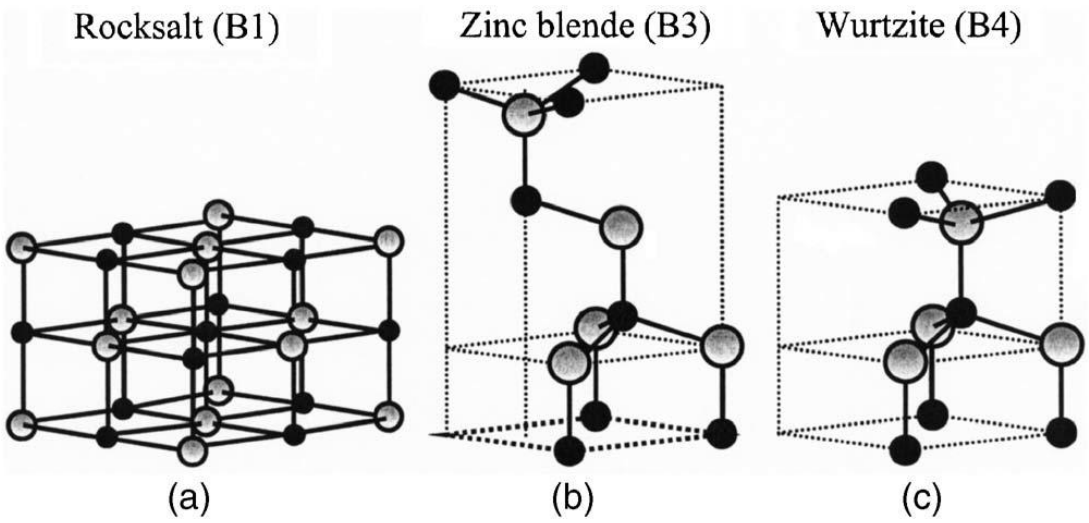

Figure 2.1 Stick and ball representation of ZnO crystal structures: (a) cubic rocksalt (*B*1), (b) cubic zinc blende (*B*3), and (c) hexagonal wurtzite (*B*4). The shaded gray and black spheres denote Zn and O atoms, respectively [15].

2.2 Zinc Oxide Nanomaterials

2.2.1 Synthesis Techniques for Zinc Oxide Nanowires

Of all the various morphologies of ZnO nanostructures, ZnO nanowires have become increasing popular for various scientific functions. There are numerous techniques used to synthesize vertically aligned ZnO nanowires including vapor-liquid-solid processes (VLS), solution-based processes, electrodeposition, sol-gel, and polymer-assisted growth [36-46]. VLS procedures operating at rather high temperatures between 900-1400°C have been a very popular and proficient means of synthesizing aligned ZnO nanowires. Additionally, the vertical alignment of ZnO nanostructures can be assisted by either an electric field [47] or through the use of lithographic patterning techniques [48]. Moreover, desirable alignment is achieved by proper lattice matching between ZnO and the epitaxial substrate [46, 49].

It is very important to have aligned nanowires for specific applications such as light-emitting diodes, field-effect transistors, and lasers [14]. In VLS, there is a metal (e.g., Au, Fe, or Sn) that serves as a catalyst to promote the reaction between the specific nanowire component(s) and the liquid alloy drops that form for preferred site deposition [15]. Au is most commonly used as the catalyst for VLS- based one-dimensional ZnO growth. Once the liquid is supersaturated with the reactants, nanowire growth is initiated [15]. Nanowire growth is terminated when either the reactants are completely used or when the catalyst is no longer in the liquid state due to temperature cooling below its eutectic temperature [15]. Moreover, during growth, the aligned growth of nanowires perpendicular to the substrate can be achieved when there is a negligible lattice mismatch between the nanowire array and the substrate [14, 15]. The SEM images of aligned nanowires grown on AlGaN substrates via the VLS process using a gold catalyst are provided in Figure 2.2.

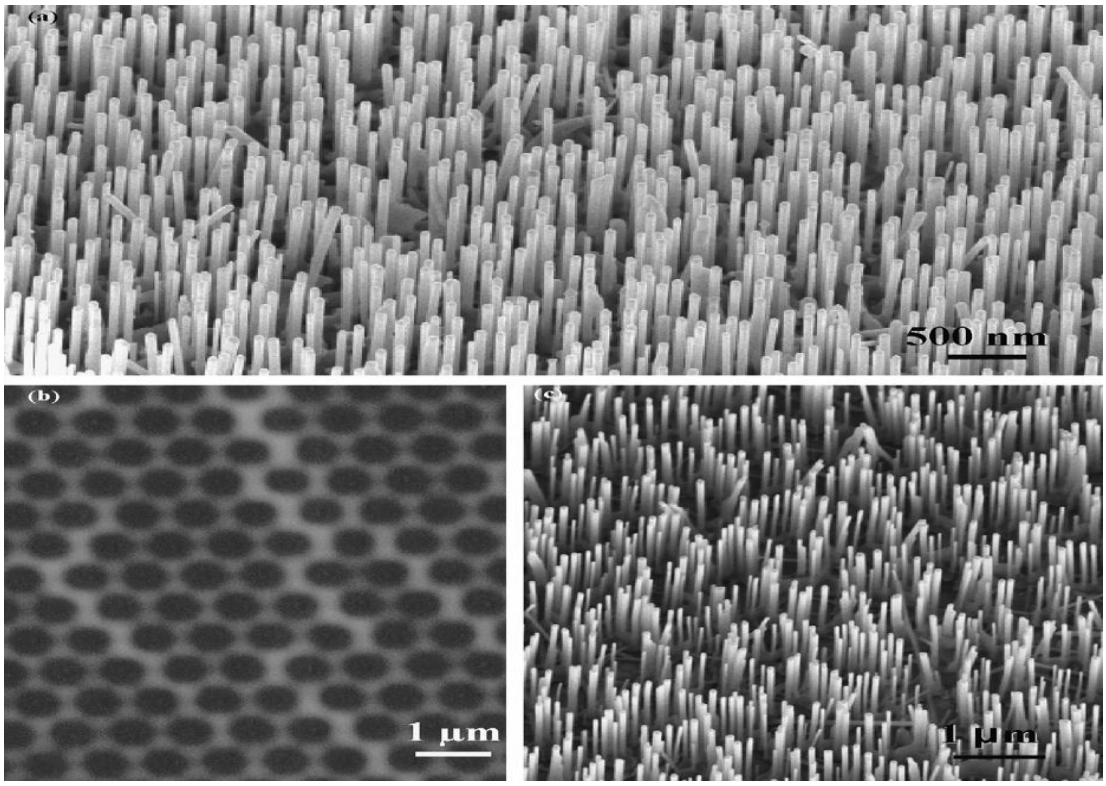

Figure 2.2 (a) SEM image of aligned ZnO nanowires grown on sapphire substrate using a thin layer of gold as catalyst. (b) SEM images of gold catalyst patterns using PS sphere monolayer as mask. (c) SEM image of aligned ZnO nanowires grown with a honeycomb pattern [50].

Another method that is very efficient in producing epitaxial growth of well-aligned ZnO nanowires is the metal-organic chemical vapor deposition (MOCVD) method [51-56]. Here, metal-organic precursors are used to aid the growth process. Some of the advantages of MOCVD over the VLS processes is that it has a catalyst-free growth mechanism, and much lower temperatures can be employed (350-500°C). Furthermore, Zhang et al. have applied MOCVD to discover a feasible means of obtaining the growth of ZnO (c-axis) normal to the substrate, which demonstrates the significance of MOCVD in large area industrial ZnO applications [57]. Typically in the MOCVD process, metal alkyls such as dimethyl zinc (DMZn) or diethyl zinc (DEZn) are used as the precursors that prompt ZnO deposition through its vapor phase chemical reactions on the substrate [15]. Typical substrates used in MOCVD include SiC, Al_2O_3 (sapphire), GaN/Si, and GaN/sapphire. The function of the carrier gas (e.g.,O_2, N_2, or Ar) is to transport the precursor reaction into the growth region. Moreover, it is important for the precursors that are employed to be as less reactive as possible with the carrier gases to lessen the effects of parasitic reactions in the vapor phase [15]. Figure 2.3 provides SEM images of aligned nanowires grown on sapphire (0001) substrates via MOCVD using O_2 gas and DEZn as reaction precursors, N_2 as the carrier gas, and employing substrate temperatures ranging from 400-500°C.

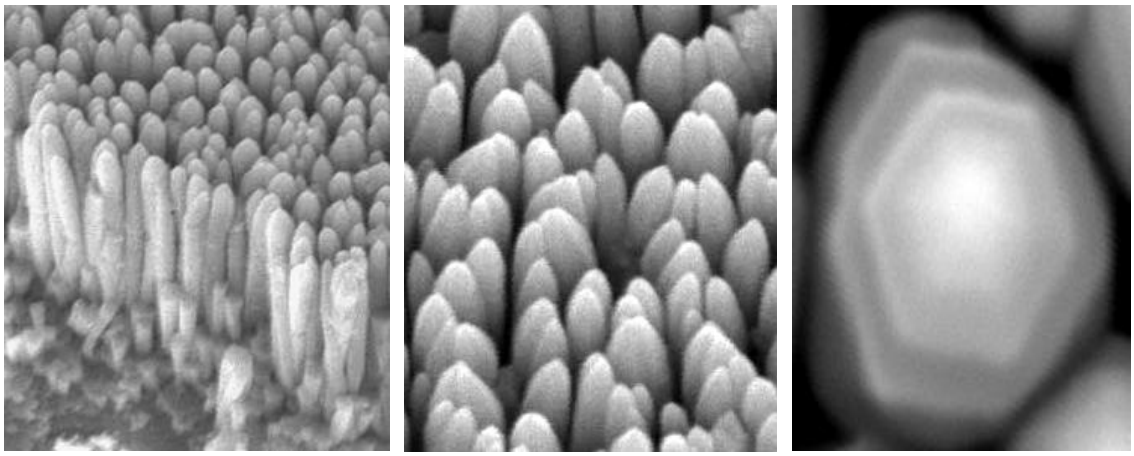

Figure 2.3 SEM images of ZnO nanorods formed on sapphire (0001) substrates. (a) Images observed from a cleaved surface. (b) Images taken with a tilt angle. (c) Image of the top of a single ZnO nanorods [56].

Although these previously mentioned processes are highly efficient and dominant in the synthesis of ZnO nanowires, solution-based processes result in sufficient nanowire structures and have proved to be more beneficial due to their simplicity and economic feasibility under less rigorous synthesis conditions. Furthermore, the employment of even lower temperatures (65-95°C) in the solution-based method allows feasible synthesis of ZnO on polymers, while other methods cannot be used for that purpose. Thus, with the solution-based method, soft and flexible substrates can be fabricated. In the solution-growth method, the substrate must be first coated with a ZnO seed layer. Seed application can be done several ways including spin-coating, dip-coating, drop-coating, and sputter-coating [45, 58, 59]. Typical substrates used to grow the ZnO nanowires include silicon substrates and doped conductive glass substrates, such as fluorine-tin oxide (FTO) and indium tin oxide (ITO) glass, for photovoltaic devices such as dye-sensitized solar cells. For the hydrothermal process, an equimolar aqueous solution of zinc nitrate hexahydrate and hexamethylenetetramine (HMTA or HMT) is typically used to grow the ZnO nanowires onto a specific substrate. There are other zinc compounds used as starting reactant

components to synthesize the ZnO nanowires, such as zinc chloride and zinc acetate; the various starting reactants used tend to vary the morphology of the ZnO nanostructure. However, the sole use of zinc nitrate hexahydrate and HMTA as the starting components has been widely reported and accepted; and thus, it is suggested that ZnO nanowires can be produced from these reactants via the following series of chemical reactions, A-E [14]:

$$(CH_2)_6N_4 + 6H_2O \leftrightarrow 4NH_3 + 6CH_2O \quad \textbf{(A)}$$

$$NH_3 + H_2O \leftrightarrow NH_3 \cdot H_2O \quad \textbf{(B)}$$

$$NH_3 \cdot H_2O \leftrightarrow NH_4^+ + OH^- \quad \textbf{(C)}$$

$$Zn^{2+} + 2OH^- \leftrightarrow Zn(OH)_2 \quad \textbf{(D)}$$

$$Zn(OH)_2 \xrightarrow{\Delta} ZnO + H_2O \quad \textbf{(E).}$$

These given chemical reactions manage the growth of ZnO nanowires and the final result of these equilibrated reactions can be influenced by altering the reaction conditions including the initial precursor concentration, reaction temperature, and growth time [14]. Specifically, the initial concentration of the starting reactants influence the NW density, while the reaction temperature and growth time generally affect the ZnO NW morphology [14]. An SEM image of

vertically aligned nanowires grown on FTO substrates via a hydrothermal method employing an 85°C growth temperature is provided in Figure 2.4.

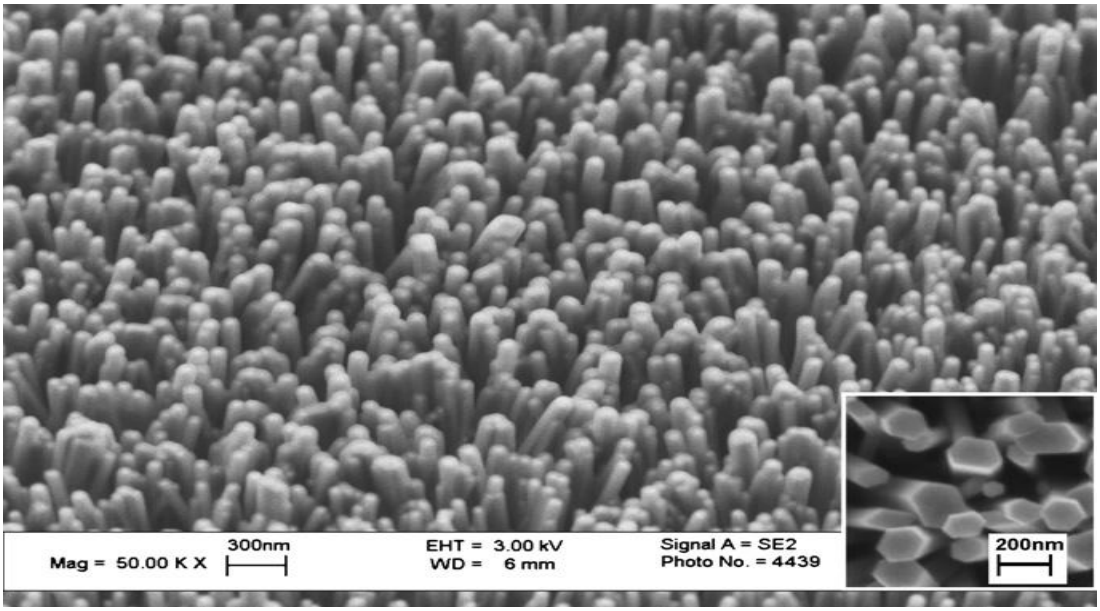

Figure 2.4 SEM image of the hydrothermally grown ZnO nanowires was taken at a 45° tilt. The inset is the top-view SEM image [60].

2.2.2 Morphology Control of Zinc Oxide Nanostructures from Aqueous Solution

The ability to control the shape, size, and orientation of ZnO nanostructures on the substrates is instrumental in engineering high performance photovoltaic devices. Govender et al. conduct a study investigating how the specific morphology of ZnO nanostructures is affected by several process factors including the reaction temperature, reaction growth time, nature of the substrate, solution pH, ionic strength and ligands [61]. However, before one can fully understand the effects of these experimental conditions, it is important to realize that a

supersaturated solution is needed to initiate crystallization and the specific degree of supersaturation determines the resulting crystal morphology [61]. As seen in Figure 2.5, there are three major degrees of supersaturation corresponding to varying growth regions.

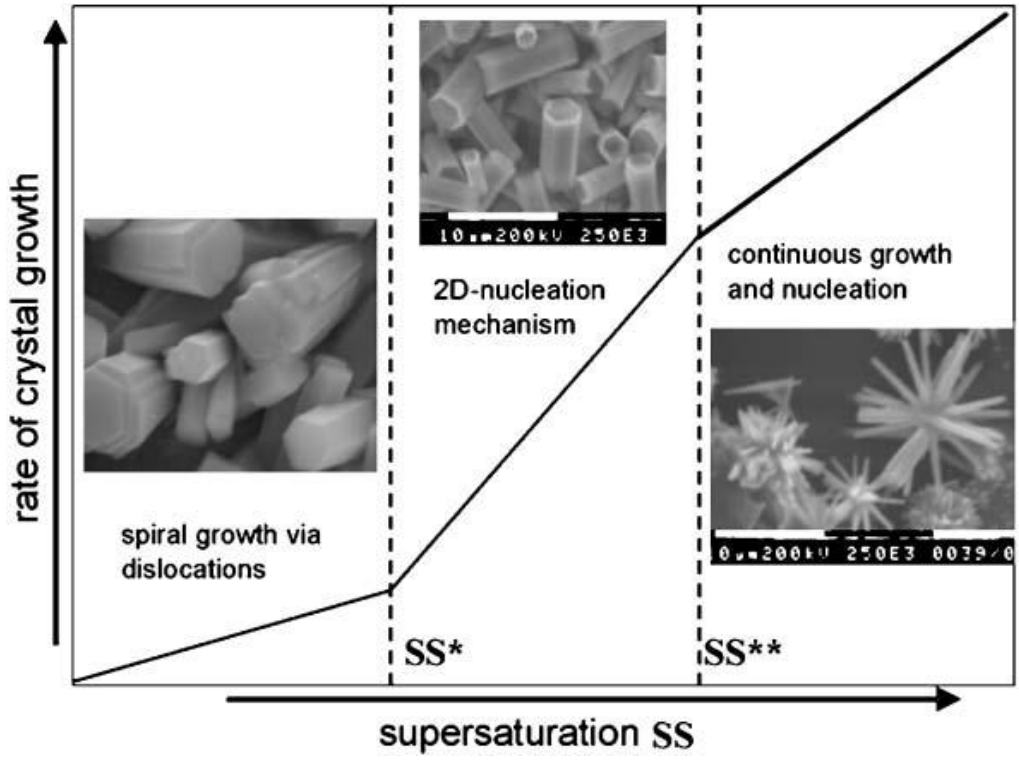

Figure 2.5 Relationship between supersaturation in deposition baths, rate of crystal growth and morphology [61].

Govender et al. found that when the pH is lowered from 6.8 to 5 for an experimental condition of ZnO grown on ZnO template layers on FTO glass using an Zinc Acetate/HMTA aqueous solution bath, the average diameter is smaller and the nanowires have well-developed crystal faces [61]. It was also found that while there is much complexity involved with the effects of ionic strength on ZnO crystal growth, it can be concluded that increasing ionic strength

causes a decrease in the width of ZnO nanowires [61]. This study also captured the influence of ligands on crystal morphology. While several reports have investigated the effect of ligands on ZnO crystal growth and morphology [62, 63], an important concept suggested here is that the hydrolysis of the Zn^{2+} cation can be controlled by the slow release of hydroxide, which is generated by the chemical breakdown of a Lewis base such as HMTA, ethylenediamine (en), or triethanolamine (TEA) at high temperatures, into the zinc salt solution [61]. Lastly, Govender et al. also examined the differences, if any, of the growth of ZnO crystal structures on four different types of substrates: 1) Au-coated FTO glass; 2) ZnO template layers on FTO glass; 3) FTO glass; and 4) single crystalline (0001) sapphire [61]. Their results reveal that more dense nanostructures can be synthesized on fluorine doped tin oxide glass as opposed to using crystalline sapphire. The qualitative results of the ZnO crystal structures grown on these four substrates can be seen in Figure 2.6.

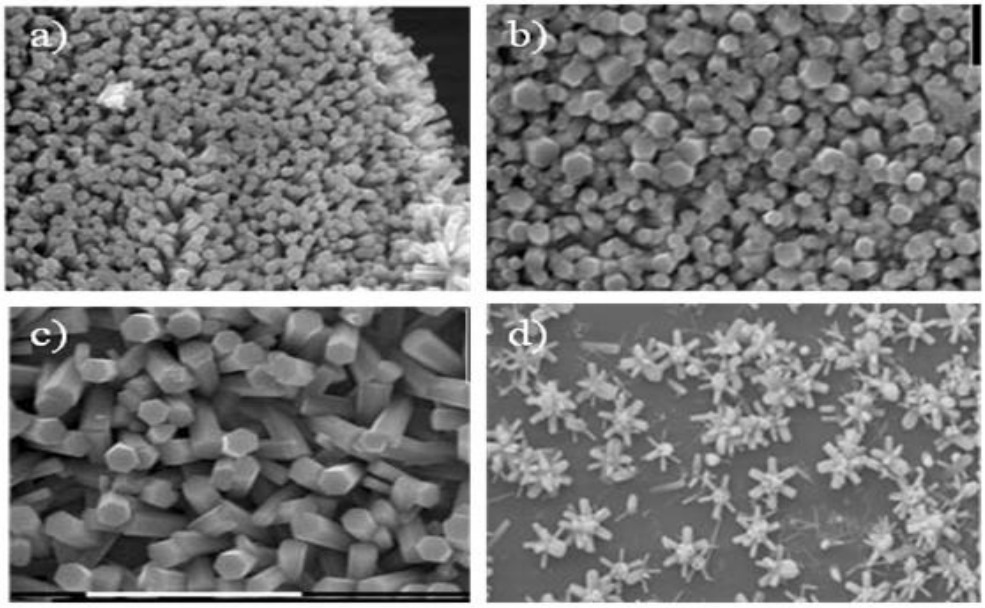

Figure 2.6 SEM images of ZnO films from aqueous solution (25mM Zinc Acetate and 25mM HMTA, pH 5, 90 °C, 1 hour) on a) Au-coated TO(F) glass; b) ZnO template layers on TO(F) glass; c) TO(F) glass; and d) crystalline (0001) sapphire [61].

Schmidt-Mende and MacManus-Driscoll reported a summary of the studies on solution growth and the resulting structures. This summary can be found in Table 2.1.

Table 2.1 Summary of Different Results and Methods for Aqueous Solution Growth. Adapted from [64]

Growth Solution	Resulting Morphology	Focus of Investigation
Zinc nitrate, HMT	Nanorods, microtubes	On Si and conducting glass substrates [65, 66]
Zinc nitrate, HMT	Nanorods, nanotubes	Influence of substrate and seed layer [67]
Zinc nitrate, HMT	Aligned nanowire arrays	Influence of seed layer [68]
Zinc-nitrate, HMT, citrate	Oriented nanocolumns, nanoplates	Control of aspect ratio: addition of citrate anions decreases aspect ratio [69]
Zinc nitrate, zinc acetate, HMT	Highly aligned nanorods	Influence of substrate and seed layer [70]
Zinc nitrate, triethanolamine, HCl (pH 5)	Ordered nanorods	Influence of substrate and counter ions in growth solution [71]
Zinc nitrate, thiourea, ammonium chloride, ammonia	Nanowires, tower- like, flower-like, tube-like	Influence of reactants, substrate pretreatment, and growth time and temperature [72]
Zinc acetate, sodium hydroxide, citric acid	Disk-like, flower- like, nanorods	Influence of pH on growth solution [73]
Comparison of different growth solutions	Star-like, nanorods	Influence of reaction conditions: ligand, counter-ions, pH, ionic strength, and deposition time Influence of substrate/ seed layer [61]
Zn foil, zinc sulfate, ammonium ions, sodium hydroxide	Nanobelt arrays, ordered nanowires	Influence of temperature and concentration of solutions [74, 75]

Andrés-Vergés et al. have also done studies on ZnO crystal morphology. They looked at experimental conditions for both Zinc Chloride/HMTA and Zinc Nitrate/HMTA starting reactants [76]. They were able to determine under which precursor concentrations and reaction temperature produced the needle-like structures and those that produced the prism-like (nanorod) structures. Tables 2.2 and 2.3 provide the data from their study for the Zinc Nitrate/HMTA solutions and Zinc Chloride/HMTA solutions, respectively.

Table 2.2 Effect of the Reactant Concentrations on the Morphology of Zinc Oxide Particles (from Zinc Nitrate Solution) [76]

	ZnO particle morphology			
HMT concentration/mol dm^{-3}	0.01 mol dm^{-3} $Zn(NO_3)_2$	0.02 mol dm^{-3} $Zn(NO_3)_2$	0.05 mol dm^{-3} $Zn(NO_3)_2$	0.1 mol dm^{-3} $Zn(NO_3)_2$
0.01	P/N	P/N	P/P	SP/SP
0.02	P/N	P/N	P/P	SP/SP
0.05	N/N	N/N	P/P	SP/SP
0.1	N/N	N/N	SP/SN	SP/SP
0.2	SN/SN	SN/SN	SN/SP	SP/SN

[a] Obtained by ageing zinc nitrate solutions at 78°C/100 °C for 30 min in the presence of HMT. P, prismatic shape; N, needle shape; SP, spherulitic prismatic aggregates; SN, spherulitic needle-shaped aggregates.

Table 2.3 Effect of the Reactant Concentrations on the Morphology of Zinc Oxide Particles (from Zinc Chloride Solution) [76]

	(ZnO particle morphology)	
HMT concentration /mol dm^{-3}	0.01 mol dm^{-3} $ZnCl_2$	0.02 mol dm^{-3} $ZnCl_2$
0.01	P/N	P/N
0.05	P/N	P/N
0.1	N/N	N/N
0.2	N/SN	SP/SN

[a] Obtained by ageing zinc chloride solutions at 78°C/100 °C for 30 min in the presence of HMT. P, prismatic shape; N, needle shape; SP, spherulitic prismatic aggregates; SN, spherulitic needle-shaped aggregates.

Both sets of data are based on the temperature increase from 78°C to 100°C. From these tables one can see that for majority of the starting concentrations of Zinc Chloride and HMTA, as you increase the temperature, the morphology changes from prism or rod-like shapes (P) to needle-like shapes (N) [76]. The SEM images of their synthesized prism and needle ZnO crystal structures can be seen in Figure 2.7.

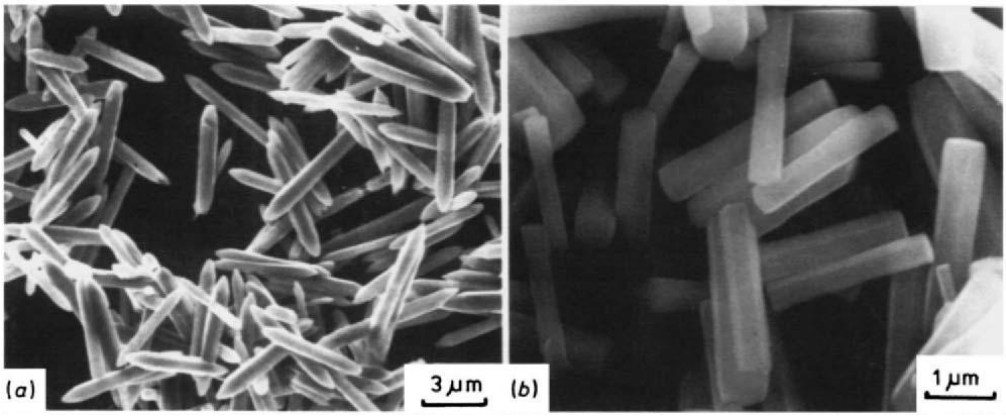

Figure 2.7 SEM of ZnO crystal structures obtained at 100°C after 30min of ageing from: (a) 20 mM $ZnC1_2$- 50 mM HMT to produce the needle shape; (b) 50 mM $Zn(NO_3)_2$ -50 mM HMT to produce the prism shape [76].

Liu et al. studied the effect of seed layer thickness on the density and diameter of nanowires [77]. Though a report prior to their studies concluded the opposite trend [78], Liu et al. were able to determine that i) the density of nanowires is greater in areas of greater seed layer thickness, and ii) the diameter and height of the nanowires decreases with increasing seed layer thickness [77]. Obviously with smaller diameter nanowires, there is more space to have a denser array of nanowires. Liu et al. suggest a possible explanation based on the fact that i) "the crystal size is smaller on a thicker seed layer, and ii) the consumption of Zn^{2+} may be higher at the areas with dense nanowires" causing the growth rate to be slower in less dense areas [77]. This would lead to shorter nanowires and if the growth rate is slower for the sidewalls of the nanowires, then the diameters would be smaller as well. Moreover, they identified a critical seed layer thickness (~ 3.5 nm) in which the ZnO seeds are thick enough to withstand the etching that occurs in order to successfully grow dense ZnO nanowires [77].

Finally, Xu et al. have reported a liquid-phase chemical process for growing ultralong ZnO nanowires with lengths up to 33 μm [79]. During solution growth reactions, ZnO also forms in the bulk solution, which limits the amount of reactant consumption by the ZnO nanowires on the substrate. This ultimately causes the nanowire length to be shorter due to the impedance of the nanowire growth rate. Many have suggested that longer nanowires can be synthesized by refreshing the growth solution every 2-3 h for long periods of time; yet the length of the nanowires are still under 20μm [10, 80, 81]. However, Xu et al. have shown a way to avoid growth of ZnO in the bulk solution by adding end-capped polyethylenimine (PEI) and ammonium hydroxide to the zinc nitrate/HMTA growth solution as a means of preventing homogeneous nucleation [79]. They believe that PEI selectively adsorbs onto certain crystal faces in the bulk solution, acting as steric hindrance to the growth of ZnO on these specific faces. The PEI does not prevent growth on the seeded substrate because the seeds are large enough to be unaffected by the blocking of PEI, allowing the crystal faces on the substrate to maintain exposure to the reactants [79]. With their preferential growth process, long nanowires of ~ 17 μm can be grown solely on the seeded substrates in 7 h without refreshing the growth solution and 33μm long nanowires can be obtained by refreshing the growth solution every 3.5 h [79]. In Figure 2.8, a comparison is shown between their preferential method and the typical liquid-phase deposition method. In both processes, nanowires grow longer with increasing reaction time; however, the preferential growth process allows for a much higher growth rate resulting in longer nanowires [79]. The SEM images of these ultra long nanowires are provided in Figure 2.9.

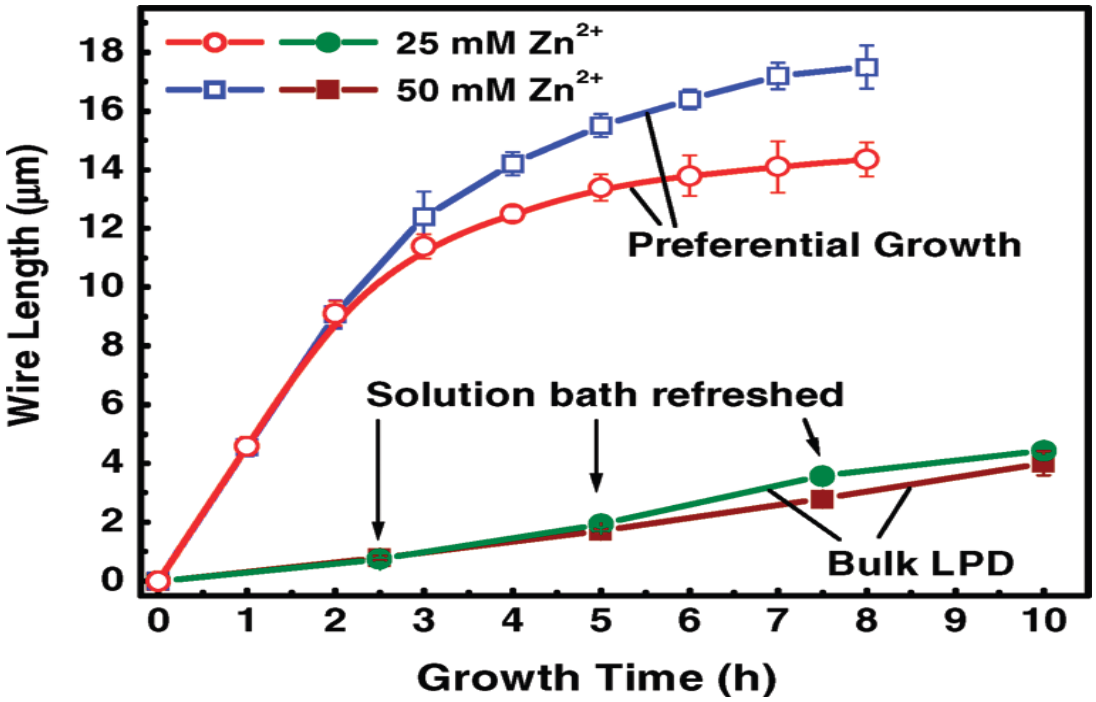

Figure 2.8 Comparison of wire growth by using the preferential growth process developed in this study and the bulk liquid-phase deposition method reported in the literature. The wire length is plotted as a function of growth time at different growth conditions [79].

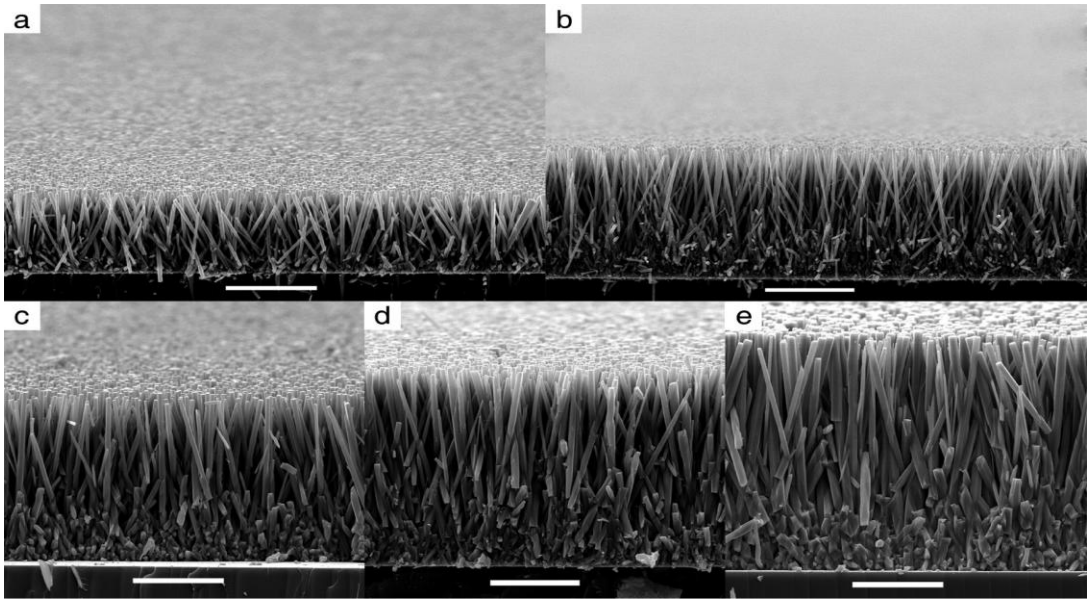

Figure 2.9 SEM images of arrays of ZnO nanowires in varied lengths via a preferential growth method. Scale bar, 10 μm. Wire length (a) 11 μm, (b) 17 μm, (c) 22 μm, (d) 27 μm, (e) 33 μm [79].

2.3 Photovoltaic Principles and Concepts

2.3.1 History of Photovoltaics

Photovoltaic cells function to directly generate electricity through solar conversion. Throughout history, scientists across the world have continually made progress regarding the advancement of photovoltaic technology. In 1839 French physicist, Alexandre-Edmond Becquerel, conducted experimental tests using a platinum electrode-electrolyte set up and witnessed the generation of electrical current upon light exposure [82]. Despite its low efficiency, Charles Fritts, an American scientist, fabricated a solar cell based on selenium wafers in 1883 [83]. Yet, there was still much research and experiments to be done to fabricate higher performing photovoltaics.

In 1921, Albert Einstein won the Nobel Prize for his report of what is now considered to be the fundamental principle of present photovoltaics (i.e., the process in which photo-induced electrons jump from the valence band to the conduction band followed by transfer through the external circuit) [84]. Later, the first practical solar cells were built by researchers at Bell Laboratories, in which these p-n junction silicon based cells provided conversion efficiencies between 5-10%, but these cells also required expensive production costs [85, 86]. The mechanism of p-n junction solar cells is considered to be the traditional fundamental mechanism of solar cells. This type of cell is comprised of an 1) n-type layer (i.e., layer doped with group V materials that have excess electrons) working as the donating anode; 2) p-type layer (i.e., layer doped with group III materials that lack electrons, creating holes) working as the accepting cathode; and 3) the p-n junction, which is the connection of the two layers [3]. Light absorption occurs in the p-n junction, and consequently the photogenerated electron-hole pairs are produced through electron excitation from the valence band to the conduction band [3].

Throughout the 1950's and 1960's, there was more research being conducted to improve the performance and lower the cost of these silicon based solar cells, also known as the first generation of solar cells. In 1969, the team at the Exxon lab in New Jersey were able to significantly reduce the cost of silicon based cells , which proved to be an enormous breakthrough since this was right before the oil shock of late 1973 when most oil companies became very interested in economical alternate sources of energy [87].

Extensive research continued over the next decade and there had been relatively high efficiencies for first generation Si-based solar cell, but at a high manufacturing cost. But researchers did not just want to make incremental improvements with these solar cells. Instead they were determined to figure out how to really evolve the state of photovoltaics that would ultimately help lower the manufacturing cost of these cells. This is when the second generation of solar cells was introduced. The second wave of photovoltaic technology was based on thin film technology. These cells also utilized the traditional p-n junction basis to separate photo-induced charge carriers.

Amorphous and crystalline Si on glass (CSG) were among this new group of second generation solar cells. Additionally, polycrystalline CdTe was among the first photovoltaic thin film materials introduced, and its highest reported efficiency is about 16.5% [3]. There were concerns with the toxicity of CdTe, and so $CuInSe_2$ (CIS) thin film cells were studied, as well as the $CuInGaSe_2$ (CIGS) thin film technologies. CIGS has shown to have great potential as it has confirmed efficiencies of nearly 20% and has proven to lower manufacturing production energy [3]. While the production costs have been lowered, the second generation cells have not bypassed the maximum efficiencies of the first generation. Moreover, multi-junction cells have really been an impressive type of second generation cell because its performance is seen as

highly competitive, and in some cases superior, over the first wave of cells with reports of efficiencies greater than 30% [3]. However, due to its high manufacturing costs, multi-junction cells can only be instrumental in areas where large expenditures are not a major limitation.

While some researchers have moved on to developing the next phase of solar cells based on new mechanisms, others still continue to experiment with ways to enhance cells based on the p-n junction phenomena. Recently, there has been research on p-n junction solar cells that incorporate nanowires. Garnett and Yang have reported their research on a low energy and scalable process for silicon nanowire p-n junction solar cells, in which they fabricate wafer scale arrays of n-type Si NWs via a solution-phase etching method, and deposit a p-type amorphous Si via low pressure chemical vapor deposition [88]. Figure 2.10 shows the illustration and cross-sectional SEM image of a Si NW n-p core-shell solar cell. They report an efficiency of only 0.5% for this particular type of Si p-n junction solar cell [88], but with more studies it is likely to increase.

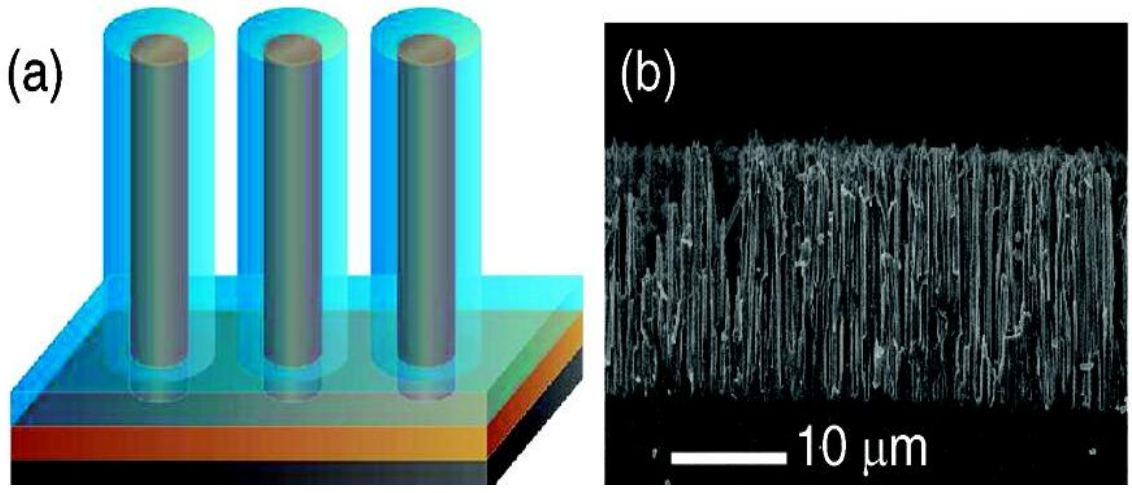

Figure 2.10 (a) Schematic cell design with crystalline n-Si NW core in brown, the polycrystalline p-Si shell in blue, and the back contact in black. (b) Cross-sectional SEM of vertically aligned NWs used in the device [88].

As mentioned before, researchers have now begun to create the third generation of solar cells. The goal of third generation solar cells is to find practical ways to improve performance (increase the conversion efficiency) and maintain a much lower production cost than the solar cells in the first two generations. The most interesting fact about these new types of solar cells is that they do not function under the traditional p-n junction working principle. Examples of these third generation cells are organic polymer solar cells, and dye-sensitized solar cells. Despite low efficiencies currently being obtained (~5% or less), photovoltaic devices based on high mobility polymers have shown potential for application as a renewable energy solution, and in particular the bulk heterojunction concept has been applied to organic polymer cells resulting in improved efficiencies [89]. The dye-sensitized solar cell is another rapidly advancing type of third generation solar cell that is governed by a different working principle. The mechanism and the impressive evolution of dye-sensitized solar cells will be discussed extensively throughout the next section and the remainder of this report. The best laboratory efficiencies of the major photovoltaic technologies over the past 35 years are charted in Figure 2.11. The third generation solar cells are considered “Emerging PV” in the chart.

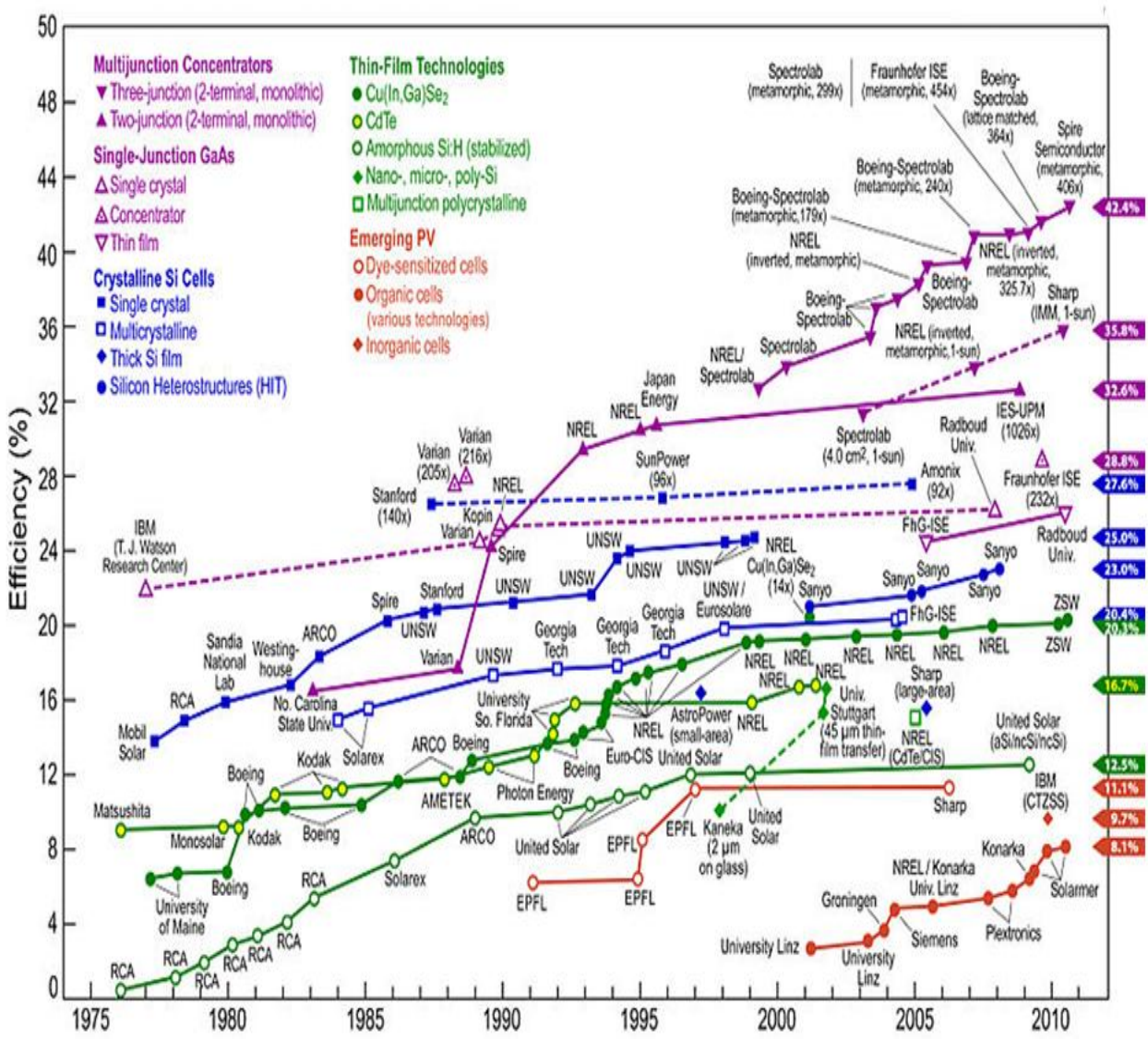

Figure 2.11 Best researched solar cell energy conversion efficiencies from 1976-2011(from National Renewable Energy Laboratory (USA)) [90].

2.3.2 Principles of Dye-Sensitized Solar Cells

Solar energy conversion has been extensively studied for many years [91-97], but in recent years, dye-sensitized solar cells (DSSC) have become an attractive renewable energy alternative. In 1991, Michael Gratzel and Brian O'Regan introduced this innovative photovoltaic device to the scientific community that required a very modest means of production that allowed for low-costing and moderately efficient solar cells [98]. Gratzel and O'Regan's dye-sensitized solar cell design was based on sintered titanium dioxide (TiO_2) nanoparticles. One of the reasons that TiO_2 nanoparticles were chosen was because they possess high surface areas (with roughness factors ~1000 [10]); enhanced surface area is needed for the adsorbed dye molecules to generate efficient light absorption. Moreover, without being sensitized in the dye, TiO_2 can only absorb light in the UV region; however, upon dye sensitization visible light could then be absorbed. The typical DSSC components include two electrodes (i.e., the working electrode (anode) is fabricated by the growth of a metal oxide nanostructure on transparent conductive oxide (TCO) glass and the counter electrode (cathode) is generally platinum coated TCO glass), the dye sensitizer in which a monolayer of dye is adsorbed onto the metal oxide nanomaterial, and the redox electrolyte that fills in the region between the electrodes [98].

Moreover, these DSSCs do not obey the traditional mechanistic principle of silicon based p-n junction cells; instead, the light absorption and charge transfer functions are assumed by separate components of the cell. Specifically, the role of the dye is to absorb photons, while the semiconductor's main function is to facilitate charge transport. DSSCs have several other advantages over the traditional p-n junction solar cell. Some examples of advantages of DSSCs over traditional p-n junction solar cells include inexpensive production, flexibility in the material

choice including the use of various substrates, and ability to function under a wide temperature range [99].

The specific mechanism of the dye sensitized solar cell is unique from traditional solar cells. Upon incident sunlight, the electrons in the dye jump from their ground state to their excited state. The electrons are then injected into the conduction band of the semiconducting material and travel through the semiconducting material to the electron collecting glass substrate. Electrons then travel from the anode through the circuit, performing useful work (i.e., generating current) around to the counterelectrode. The dye is now in an oxidized state but is regenerated by the reducing agent of the electrolyte. In turn, the oxidized species of the electrolyte is reduced to its original state once the electron has passed through the load and is collected at the counterelectrode. At this point, the circuit is complete, and the cyclic flow of electrons continues to pass from the anode to the cathode [100, 101]. "The cell voltage observed under illumination corresponds to the difference between the quasi-Fermi level of TiO_2 under illumination and the electrochemical potential of the electrolyte [98]." Ultimately, based on this unique mechanism and fabrication requirements, the DSSC can produce electrical power at low cost and moderate efficiencies. The operation principle of DSSCs is illustrated in Figure 2.12.

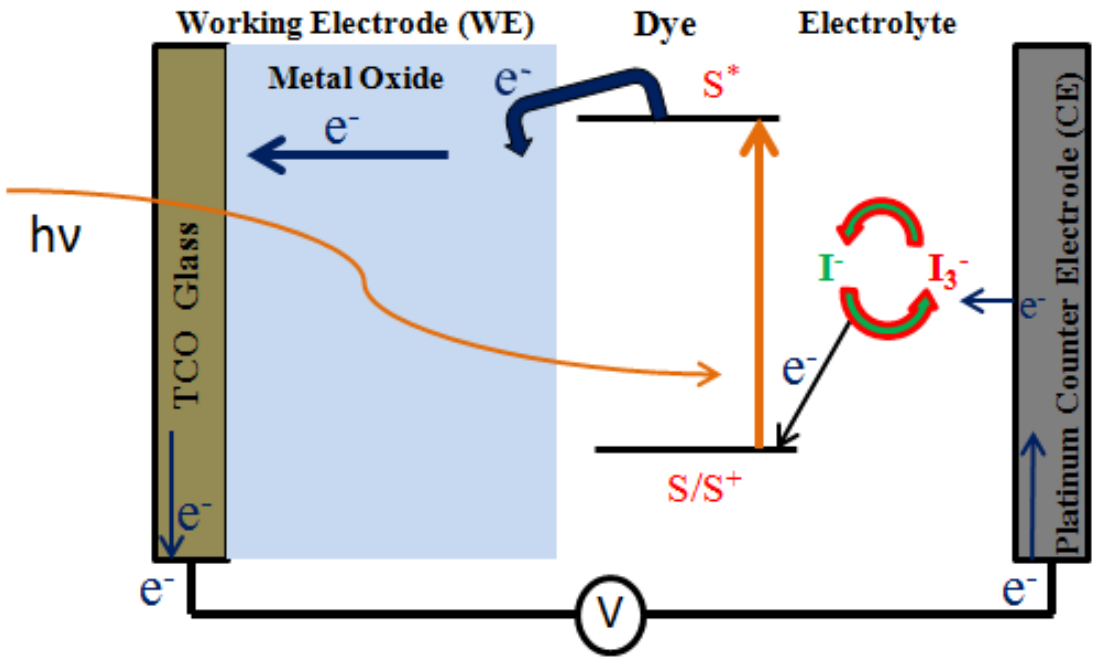

Figure 2.12 Schematic illustrating the operation principle of DSSCs.

Furthermore, Jose et al. have described the eight fundamental processes that occur within DSSCs, and a functional diagram of these processes can be seen in Figure 2.13. Jose et al. explain the 8 processes as follows [99]:

i) Light absorption by dye molecules

ii) Relaxation of the excited dye back to its ground state- rate constant (k_1)

iii) Exciton diffusion through dye material (D_{ext})

iv) Electron injection from excited dye to semiconductor conduction band- rate constant (k_2)

v) Electron back transfer to oxidized species of the electrolyte- rate constant (k_3)

vi) Electron recombination to oxidized dye molecules-rate constant (k_4)

vii) a) Electron transport through conduction band via diffusion (D_e);

b) Phonon relaxation in which energy is lost due to phonon-electron contact

viii) Dye regeneration via electron transfer from electrolyte-rate constant of (k_5) [99].

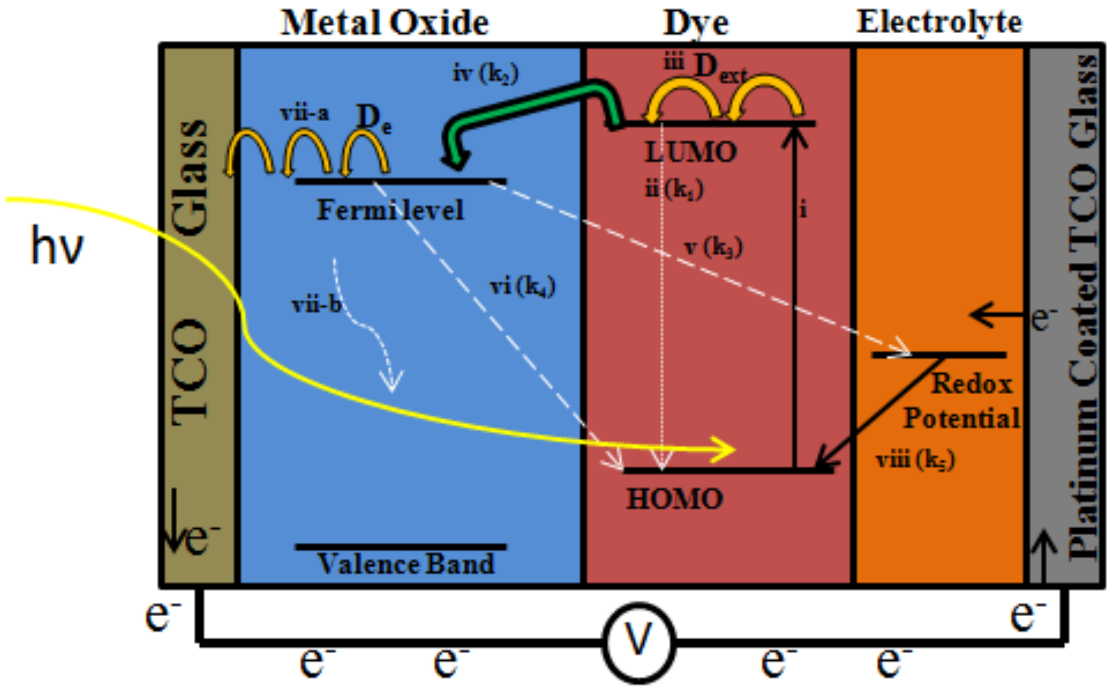

Figure 2.13 Functional diagram of DSSC illustrating 8 fundamental processes. Adapted from [99].

As mentioned earlier, the emergence of dye-sensitized solar cells was based on TiO_2 nanoparticles. However, there has been significant interest in studying other metal oxide nanomaterials to replace the TiO_2 nanoparticles. The requirements of the metal oxide are i) it should possess a wide bandgap to ensure that most photons are absorbed as possible; ii) the energy level of the conduction band needs to be appropriately lower than the HOMO level of the dye to ensure proper injection of the electrons from excited dye molecules; iii) it should have a

high charge carrier mobility for effective charge transport; and iv) it should possess a large enough surface area for efficient light harvesting [102].

Specifically, in the past decade, there has been an extensive amount of research done on DSSCs where the semiconducting metal oxide material is ZnO nanowires. Still, as of today, the amount of literature based on ZnO nanowire DSSCs is small in comparison to TiO_2 nanoparticle-based DSSCs. However, there are some advantages to utilizing ZnO nanowires. Figure 2.14 provides an illustration of the nanowire-based dye-sensitized solar cell.

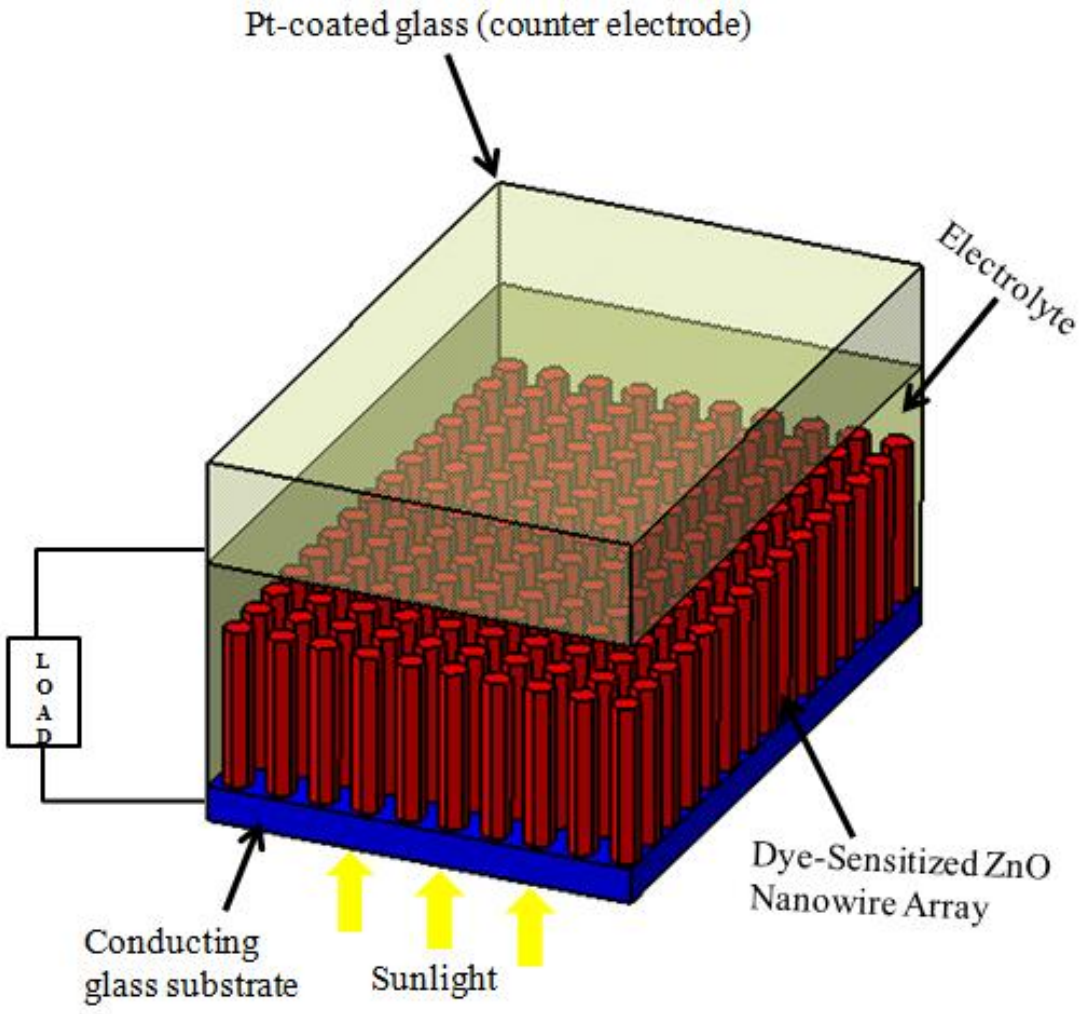

Figure 2.14 Illustration of a ZnO nanowire-based DSSC.

Utilizing wide-band gap semiconductor nanowires (e.g., ZnO nanowires) instead of TiO_2 nanoparticles has been thought to be very advantageous because i) the nanowire morphology allows for electrons to travel a more direct conduction path from the point of injection to the point of collection, and ii) the nanowires possess a large enough surface area for adequate dye adsorption [9]. The nanowire photoanode has a very fast electron injection rate and the electron diffusivity in crystalline wires (specifically ZnO nanowires) has been reported as several orders of magnitude larger than electron diffusivity within TiO_2 nanoparticles [10-13]. The superior electron transport within the nanowire photoanode can be attributed to its higher crystallinity and the presence of an internal electric field that facilitates electron transport to the collecting glass substrate by effectively separating the injected electrons from the oxidized species of the electrolyte; this, in turn, improves the charge collection efficiency [10]. Furthermore, nanowires can be synthesized at low temperatures, which allow the use of various substrates including polymers, and the employment of low temperatures greatly reduces energy costs. However, researchers have yet to fabricate ZnO nanowire-based DSSCs with efficiencies similar or higher than TiO_2 nanoparticle-based DSSCs. The current highest efficiency resulting from a DSSC incorporating ZnO nanowires is 7 %, but this DSSC was based on 1D multilayer ZnO nanowire arrays [103]. Another report showed an efficiency of 4.8%, but it was also unique in that it was comprised of a hierarchal structure of ZnO nanosheets and nanowires [104]. Reports of DSSCs that solely incorporate 1 layer of ZnO nanowire arrays typically have efficiencies ranging from 0.1-3% [9, 79, 81, 105-107].

2.3.3 Characterization of Dye-Sensitized Solar Cells

Current-voltage measurements are taken to characterize the performance of DSSCs. In order to compare experimental power conversion efficiencies (η) reported globally, DSSC measurements are generally taken under a set of standard conditions: i) constant cell temperature of 25°C; ii) input power density of 100 mW/cm^2; and iii) simulated sunlight characterized as AM 1.5, which is the air mass coefficient corresponding to incident sunlight at an angle of 48° [99]. The power conversion efficiency, η, is defined as [99]

$$\eta = \frac{P_{max}}{P_{in}} = \frac{J_{SC} \times V_{OC} \times FF}{P_{in}}, \quad \textbf{(2.2)}$$

where V_{OC} is the open circuit voltage (i.e., the voltage in unit volts at which the current is zero), J_{SC} is the short-circuit current density (i.e., the current density, generally in units mA/cm^2 at which the applied voltage is zero), Pin is the input power density generally in units mW/cm^2, and FF is the fill factor. The FF is defined as the ratio of maximum power output to the product of V_{OC} and J_{SC} [99],

$$FF = \frac{J_{MP} \times V_{MP}}{J_{SC} \times V_{OC}}, \quad \textbf{(2.3)}$$

where J_{MP} and V_{MP} are the corresponding current density and voltage, respectively of the maximum power point. A current-voltage (I–V) curve is shown in Figure 2.15 to illustrate the key parameters required to evaluate the DSSC power conversion efficiency.

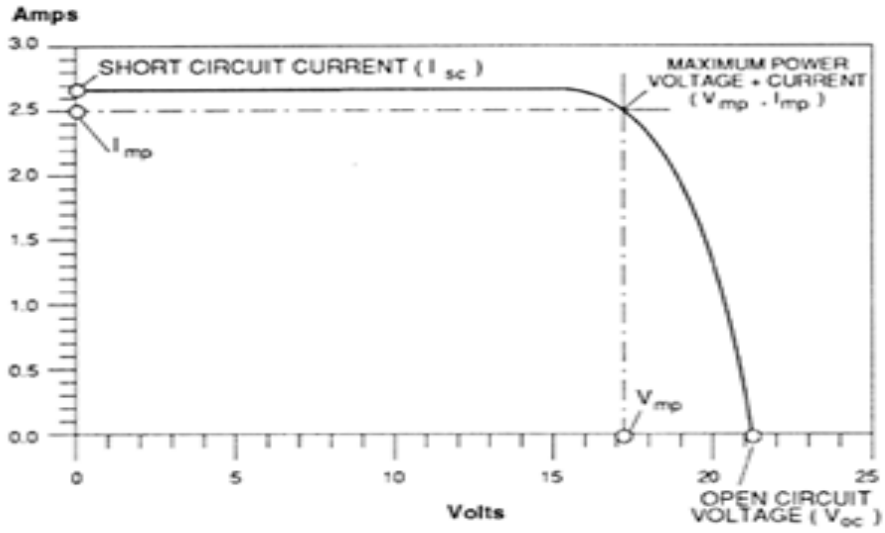

Figure 2.15 (Left) Standard I-V curve used to determine η after inverting the raw data [108].

The Incident Photon-to-Current Conversion Efficiency (IPCE) is another common measure of DSSC performance. IPCE is defined as the ratio of the number of electrons ($n_{electrons}$) flowing through the external circuit generating current to the number of incident photons ($n_{photons}$) at a specific wavelength as seen in Equation 2.4 [99].

$$IPCE\ (\lambda) = \frac{n_{electrons}(\lambda)}{n_{photons}(\lambda)} = \frac{J(\lambda)\times h\times c}{P_{in}(\lambda)\times e\times \lambda}\ , \qquad \textbf{(2.4)}$$

where J(λ) is the measured current density and $P_{in}(\lambda)$ is the input power density at a specific wavelength of irradiation in nanometer, λ, h is Plank's constant, c is the speed of light, and *e* is the elementary charge [99]. Lastly, Electrochemical Impedance Spectroscopy (EIS) is used widely in photovoltaic studies to understand the charge transport dynamics and kinetics of the DSSC [99]. EIS can reveal pertinent information regarding the dynamics of the competing processes of charge recombination (typically with the oxidized electrolyte species) and charge collection [109].

2.3.4 Factors that Govern the Performance of Dye-Sensitized Solar Cells

As previously mentioned, the current state of performance of DSSCs has not been comparable to other solar cell types due to its much lower efficiencies and stability. There are several factors that contribute to the substandard performance of DSSCs. The three most significant factors that govern DSSC performance are 1) inefficient light absorption; 2) sub-par photovoltage output; and 3) low fill factors [110]. The inefficient light absorption can mostly be attributed to the restrictive spectral response of current dye sensitizers used in DSSCs [110]. The sub-par photovoltage is mostly due to the occurrence of charge recombination, while the losses in series resistance are most responsible for the low fill factor values [110].

While common dyes that are used today, such as N719, have shown great potential (i.e., efficiency ~11-12% for TiO_2 DSSC using N719), they still lack the optimum range of light absorption needed for higher efficiencies because their optical absorption range generally does not surpass 800 nm; therefore these dyes are only able to produce current densities in the range of 15-20 mA/cm^2 [110] . The UV-Vis absorption spectrum of N719 in an equimolar ratio of acetonitrile and tert-butanol is shown in Figure 2.16.

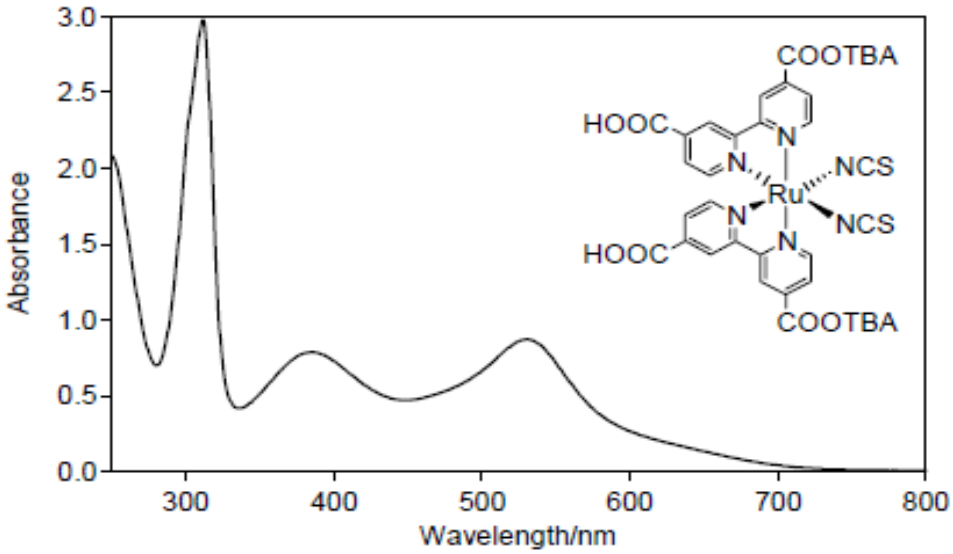

Figure 2.16 UV-Vis absorption spectrum of N719 in 1:1 acetonitrile and tert-butanol. The inset shows the molecular structure of N719 [111].

There must be a collective effort to synthesize new dyes that have broader spectral responses in order to obtain current densities beyond 25 mA/cm^2 so that the DSSC efficiency can be significantly improved. There has been some work performed already to engineer new dyes, such as ruthenium based K-19, that have better molar extinction coefficients and have a broader spectral response allowing for an improvement in light harvesting as well as stability [110, 112, 113]. These new dyes are thought to be quite promising in the efforts of trying to reach DSSC efficiencies beyond 12%.

There is still a challenge in today's DSSC research as to how we can produce high photovoltages. Research studies have shown that reducing charge recombination at the metal oxide-electrolyte interface could substantially increase device efficiencies by up to 50% [110]. Some of the techniques investigated to increase open circuit voltages of DSSCs include the

incorporation of barrier layers that help reduce interfacial recombination losses, as well as the engineering of electrolytes with coadsorbents [110]. High fill factor values are an indication of high performing DSSCs as the fill factor essentially measures how close the I-V response is to ideal conditions. As mentioned earlier, limitations of the fill factor are mostly due to series resistance losses. It is believed that the amount of series resistance can be influenced through manipulation of the contact between the two electrodes as well as proper contact of the electrodes with the wires that connect the electrodes.

In addition to these 3 governing factors, the conversion efficiency of DSSCs can also be greatly affected by the semiconductor film morphology and its fabrication conditions. It is essential for the surface area of the semiconducting nanomaterial to be as large as possible. Additionally, it is known that larger particles can absorb red light absorption via light scattering much more efficiently than N719 dye, yet the presence of these large particles can cause back-scattering that reduces surface area [111]. Thus, Wang et al. have reported the design of a multilayer TiO_2 morphology used to fabricate a DSSC that balance the opposing effects of light scattering and surface area; and their proposed morphology allowed for an increase in the cell's efficiency [111]. Another aspect of film morphology is the thickness of the film. The thickness of the semiconductor films greatly affects the DSSC performance. Giannouli et al. conducted a study that shows the dependence of the DSSC efficiency on ZnO film thickness, for two different sensitizers: Rose Bengal, and Rhodamine B [114]. Figure 2.17 provides the results of this study.

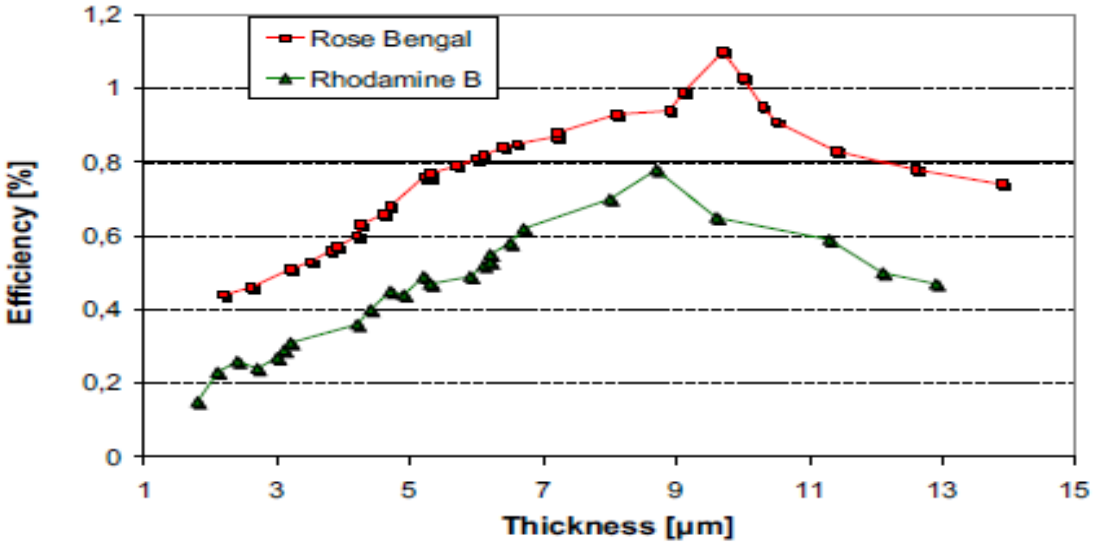

Figure 2.17 The effect of ZnO film thickness on the DSSC efficiency for ZnO films sensitized with Rose Bengal and with Rhodamine B [114].

The results from the study of Giannouli et al. showed that the efficiency of DSSCs increases with increasing thickness of the ZnO film up to an optimum thickness, and then decreases for cells with thicker films [114]. This trend held true for both of the sensitizers studied. However, for Rhodamine B, which has a higher molar extinction coefficient than Rose Bengal, the maximum efficiency could be achieved using a smaller film thickness [114]. The molar extinction coefficient indicates how well a sensitizer absorbs light; therefore, with a higher molar extinction coefficient, dye molecules can be adsorbed on thinner ZnO films in order to yield relative maximum efficiencies [114].

Lastly, specific fabrication conditions of the semiconductor film can affect the performance of the DSSC. Specifically, Lu et al. conducted a study that investigated the effect of the annealing temperature on the performance of a ZnO nanoparticle-based DSSC [115].

Annealing temperatures ranging from 300°C to 450°C were studied, and the results of this study can be seen in Figure 2.18 and Table 2.4.

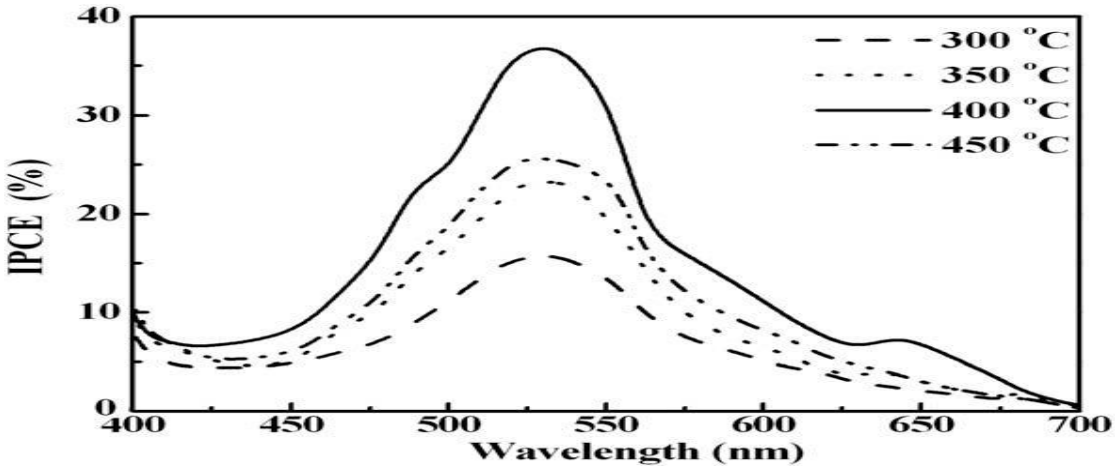

Figure 2.18 IPCE spectra of ZnO-based DSSCs annealed at different temperatures [115].

Table 2.4 Operation parameters of ZnO-based DSSCs made with different photelectrodes [115].

Electrodes (°C)	V_{oc} (mV)	I_{sc} (mA cm^{-2})	FF	η (%)	Dye adsorbed amount ($\times 10^{-8}$ mol cm^{-2})
300	599	8.36	0.51	2.51	4.46
350	599	10.76	0.46	2.94	4.35
400	549	16.84	0.43	3.92	4.29
450	619	11.64	0.38	3.05	4.18

It was found that 400°C was the optimal annealing temperature due to its highest IPCE value and highest conversion efficiency of 3.92% [115]. Moreover, Lu et al. concluded that at an annealing temperature of 400°C, a higher charge collection efficiency can be obtained because this temperature allowed for the largest reduction in the effects of bulk traps [115].

2.4 Thesis Hypotheses

I. A critical problem that generally occurs with DSSCS is when the oxidized species of the redox system electrolyte acts to regenerate itself by taking the electrons that are at the anode. This problem is referred to as back transfer of electrons from the conductive glass layer to the oxidized species in the electrolyte, which will undoubtedly reduce power conversion efficiency. It is expected that a blocking layer of optimal thickness on the surface of the conducting glass substrate will successfully control this electron back transfer, and subsequently the efficiency of a ZnO nanowire-based DSSC will be improved.

II. While reports have shown that increases in the length of the nanowires yield increases in the overall conversion efficiencies dye-sensitized solar cells, it is still very difficult to synthesize nanowire arrays with very long lengths. Therefore, we have proposed several methods to build multiple layers of three-dimensional structures containing average length ZnO nanowire arrays via various deposition techniques. It is expected that a dye-sensitized solar cell assembled by depositing several ZnO nanowire layers on the surface of the substrate will significantly improved the efficiency. In particular, if the diameter of the ZnO nanowires can be decreased and the density of the ZnO nanowire array can be significantly enhanced, it is believed that the performance of the ZnO nanowire-based DSSC will be greatly enhanced.

III. Additionally, it is expected that a model can be developed that will investigate how the geometry of ZnO nanowires affects the incident photon-to-current conversion efficiency of 1D ZnO nanowire-based N719-sensitized solar cells at the maximum absorption wavelength of 543 nm.

2.5 Thesis Objectives

- Initiate an exploration of a mathematical model that will investigate how the geometry of ZnO nanowires affects the incident photon-to-current conversion efficiency of 1D ZnO nanowire-based N719-sensitized solar cells at the maximum absorption wavelength of 543 nm.

- Design a study that investigates and compares several methods to incorporate a functional block layer at the surface of the conducting glass substrate of the ZnO NW based DSSC as a means to control electron back transfer and ultimately improve the overall power conversion efficiency

- Investigate effects of the density of ZnO NW arrays on the overall DSSC power conversion efficiency by designing a three-dimensional ZnO NW that increases the NW density and enhances surface area, and thus enhances light absorption

- Design a novel fabrication technique that is inexpensive and simple that yields a multilayered three dimensional ZnO NW array that significantly increases the density of the nanowire array, improving the overall power conversion efficiency of ZnO NW based DSSC

CHAPTER 3

FABRICATION OF ZINC OXIDE NANOWIRES

3.1 Introduction

There are several ways to synthesize ZnO NWs including chemical vapor deposition, laser ablation, template-based synthesis, and hydrothermal growth. Hydrothermal growth has become very popular due to the fact that the production cost is much lower, the process is simpler, the temperatures are lower, and less rigorous synthesis conditions are employed. During the hydrothermal growth of ZnO nanomaterials, capping agents are sometimes added to the growth solution to influence the morphology of the nanomaterial by either promoting or hindering the growth of certain crystal faces [8]. Specifically when ZnO NWs are the desired shape, HMTA is used as the capping agent to inhibit lateral growth; consequently, the promotion of vertical growth leads to the long and thin morphology of a nanowire. Weintraub reports that the formation of long and thin ZnO NWs may be attributed to the selective adsorption of non-polar HMTA on the non-polar faces of the ZnO NWs, resulting in steric hindrance of the a-planes [116]. While the full understanding of the role of HMTA is still fairly unknown, Figure 3.1 provides an excellent illustration to help understand one possible function of the multi-functional HMTA precursor. The non-polar HMTA preferentially adsorbs to the non-polar $\{10\bar{1}0\}$ and $\{11\bar{2}0\}$ crystal faces, resulting in steric hindrance of the a-planes and continued exposure to the Zn^{2+}-containing growth solution for the c-plane [116].

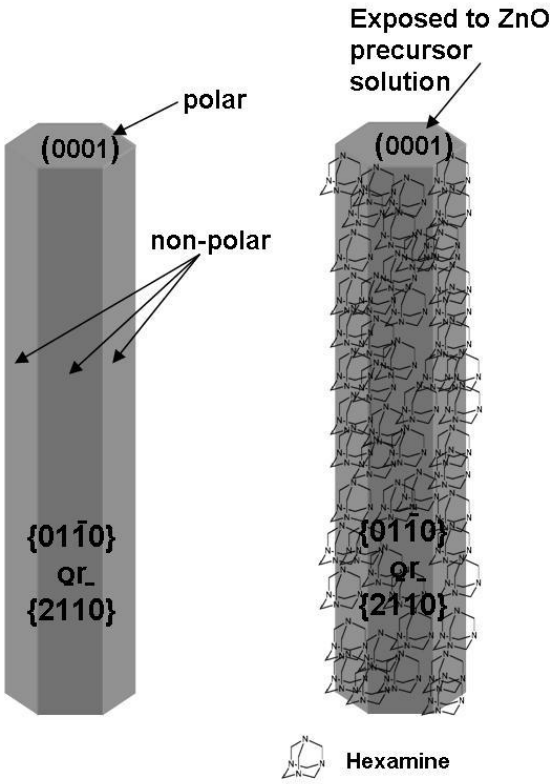

Figure 3.1 Schematic showing role of hexamethylenetetramine as a capping agent to promote 1-D growth [116].

As mentioned in Chapter 2, growth time and temperature control the ZnO morphology, whereas the initial equimolar concentration of the reactants (e.g., zinc nitrate and HMTA) influences the ZnO NW density. As the Zn^{2+} concentration increases, the zinc chemical potential inside the solution also increases; therefore, more nucleation sites are produced on the substrate in order to compensate for the increase in zinc chemical potential yielding a more dense array of ZnO nanowires [14]. As the zinc concentration is further increased, the density of ZnO NWs remains somewhat fixed. Wang et al. suggest two possible explanations as to why there can be a steady density (i.e., no new nuclei initiation on the substrate): i) if the sizes of the nuclei are smaller than the nuclei critical size, then no new nanowires can grow; and ii) the added Zn^{2+} ions on the substrate are more likely to arrive at the existing NWs rather than the newly formed

nuclei [14]. In this situation there cannot be continual increase in density with increasing precursor concentration if the density is greater than the critical steady density described earlier; moreover, this theory also suggests the occurrence of somewhat uniform height of the nanowires [14]. Furthermore, Wang et al. conducted experiments that investigated the relationship between precursor concentration and the density of NW arrays, see Figure 3.2 [14].

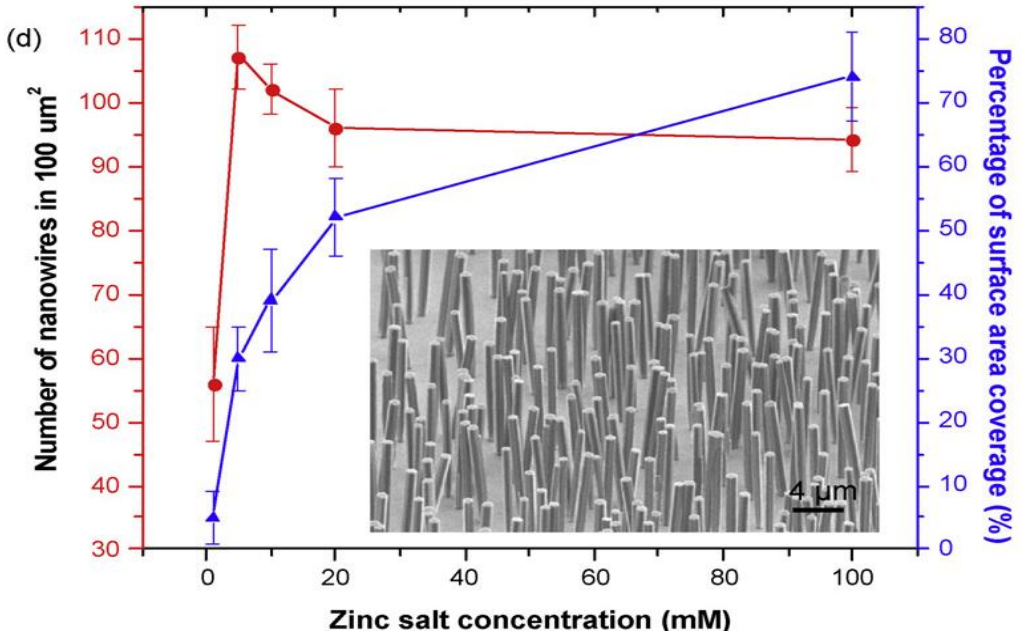

Figure 3.2 Density varied with concentration. (Circle) Plot of ZnO nanowire density in a 100 mm^2 area; (Triangle) Plot of area percentage covered by ZnO nanowires. Each data point was obtained from 4 different areas. Inset is a typical image of ZnO nanowires grown at 5 mM [14].

The results of their study show that the precursor concentration does influence the density of the ZnO nanowires. From 0.1 mM to 5 mM, their results reveal a significant increase in the ZnO NW density, and then the density remains fairly steady for higher concentrations of Zn^{2+}. Additionally, their results show that the surface coverage continually increases with increasing Zn^{2+} concentration. This is due to the increasing diameter of the ZnO nanowires.

For this research, one of the main objectives is to improve the efficiency of the dye sensitized solar cells by synthesizing highly dense arrays of ZnO nanowires that improve the surface area of the nanowires. Thus, it was important to study the results of the ZnO NWs fabricated based on various synthesis conditions, including reaction time, growth temperature, and precursor concentration using the hydrothermal growth method.

3.2 Fabrication Procedure

ZnO NWs were synthesized using a hydrothermal chemical solution based method. High-density ZnO NWs were grown on 1x1 cm^2 seeded fluorine-doped tin oxide (FTO) substrates (TEC 8 Ω/cm^2-3.0mm thick, Hartford Glass) via the following steps. Formation of the seed layer onto the FTO substrate was conducted via spin-coating of a 5 mM ethanolic solution of zinc acetate dihydrate ($ZnAc \cdot 2H_2O$) (molecular formula: $Zn(CH_3COO)_2 \bullet 2H_2O$, Acrōs Organics, 98%). The spin coating machine (P-6000 Spin Coater, Integrated Technologies, Inc.) was set to 3000 rpm and the spin cycle time was 60 sec, see Figure 3.3. SEM analysis determined that multiple spin coatings (usually 6-7 times total) were needed for a dense seed layer on the FTO substrate. The dense seed layer was annealed at 350°C for 20-30 min to form the ZnO nanocrystalline layer. ZnO NWs were grown from the seed layer using a chemical bath deposition method in an equimolar aqueous precursor solution (ranging from 10-25 mM) of zinc nitrate 6-hydrate ($ZnNO_3 \bullet 6H_2O$, J.T. Baker 99.4%) and hexamethylenetetramine (HMTA) (molecular formula: $C_6H_{12}N_4$, Fluka 99.5%) at 70-90°C for 5 h. The reaction time was varied from 5-24 h to attain optimal nanowires. Substrates were subsequently rinsed with water and ethanol and oven dried at 95°C for 30 min in air. As-grown ZnO NWs could be annealed further in air at 400°C for 30 min to improve the crystallinity of the NWs and the interfacial structures. Figure 3.4 provides a schematic illustration of the setup, while Figure 3.5 gives a representative image of the synthesis setup. The figures show that the substrates were fully immersed in the precursor solution contained in a 50 mL capped Pyrex vessel, and were fastened to the top directly from the cap.

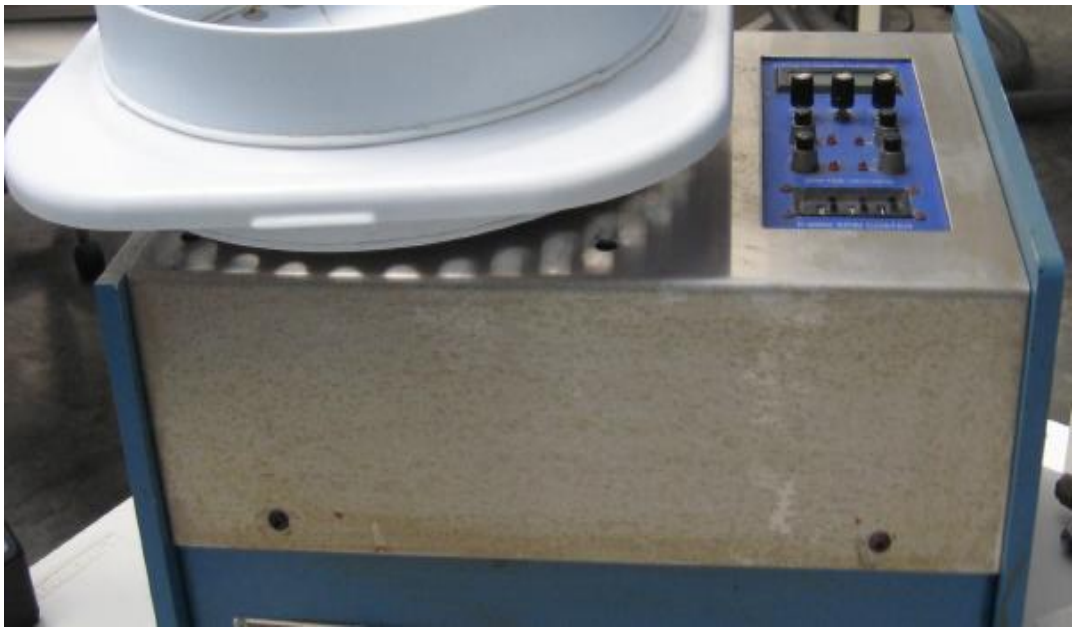

Figure 3.3 Image of P-6000 Spin Coater (Technologies Integrated, Inc.) [117].

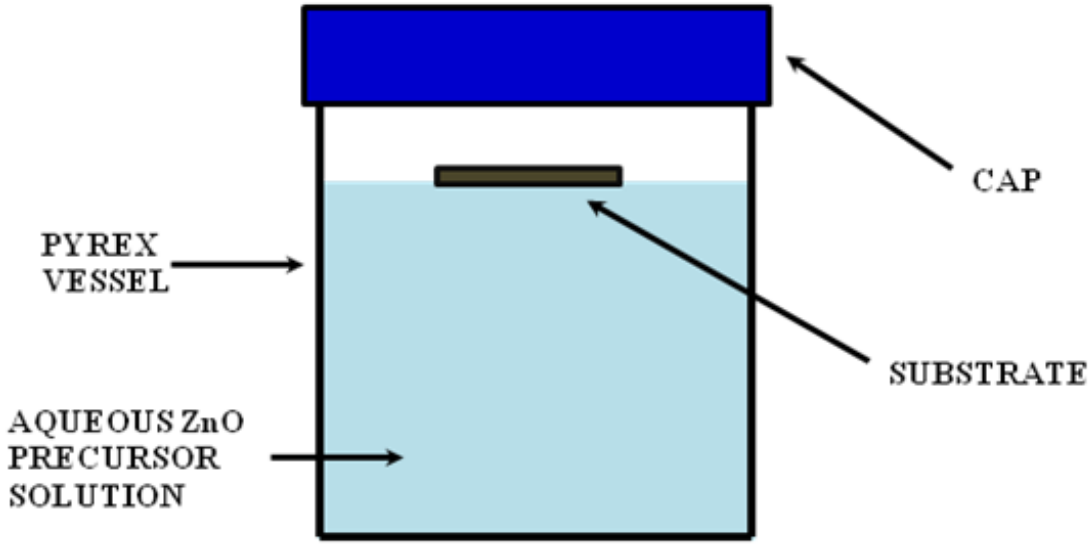

Figure 3.4 Schematic of synthesis setup.

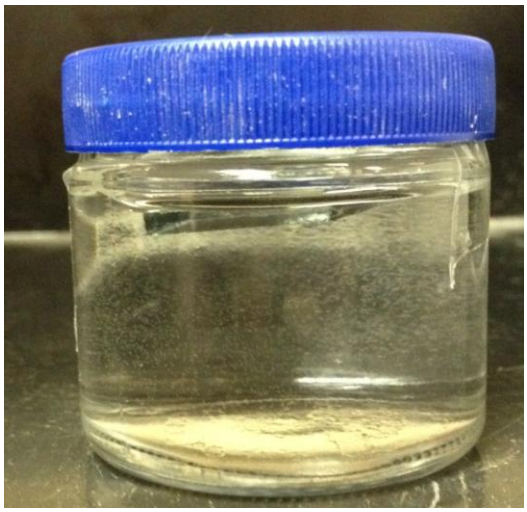

Figure 3.5 Solution-based synthesis vessel consisting of 50 mL Pyrex bottle filled with precursor solution.

The Pyrex vessels were placed inside a VWR Vacuum Oven to react at approximately 90°C, and later transferred to a Fischer Scientific Muffle Furnace to anneal at a heating rate of 2°C/min until it reached 400°C (see Figure 3.6).

Figure 3.6 (Left) Vacuum Oven (1400E, VWR Scientific); (Right) Muffle Furnace (Fischer Scientific) [118, 119].

The morphologies of the deposited materials were examined using Scanning Electron Microscopy (SEM: *LEO 1530 thermally-assisted field emission). The crystal structures of the composites were investigated using X-Ray Diffraction (XRD: X'Pert Pro).

3.3 Zinc Oxide Nanowire Synthesis and Characterization Results

The first objective of this research project was to successfully grow ZnO nanowire arrays. Due to its simplicity, low costing materials, and easily accessible equipment required, it was decided to employ a solution-based growth method. Furthermore, small pieces of Si wafers were used to practice synthesizing arrays of ZnO NWs. Initially, a sputter-coating approach was chosen to apply a very dense ZnO seed layer (~20-50 nm thick). During the first several months of a tedious series of growing the ZnO NWs under various synthesis conditions, the precursor solutions only produced a dense ZnO nanoparticle morphology. These ZnO nanoparticles typically appeared in a random clustered formation. The average diameter of these nanoparticles was around 200 nm. Figure 3.7 provides SEM images of a few of these initial results at various magnifications. Although these nanoparticles were not the desired morphology, they did posses the hexagonal-shaped face at the ends that is very characteristic of ZnO nanowires. The reason for the nanoparticles having the hexagonal faces of typical nanowire structures, but not the lengths, could be attributed to several different reasons including the precursor solution not being reacted under the proper combination of optimal conditions such as the concentration, temperature range, and growth time. Moreover, while it is clear that the degree of supersaturation was high enough for crystal initiation, the degree of supersaturation may not have been high enough (i.e., not in the appropriate regime discussed in Chapter 2) to stimulate further crystal growth.

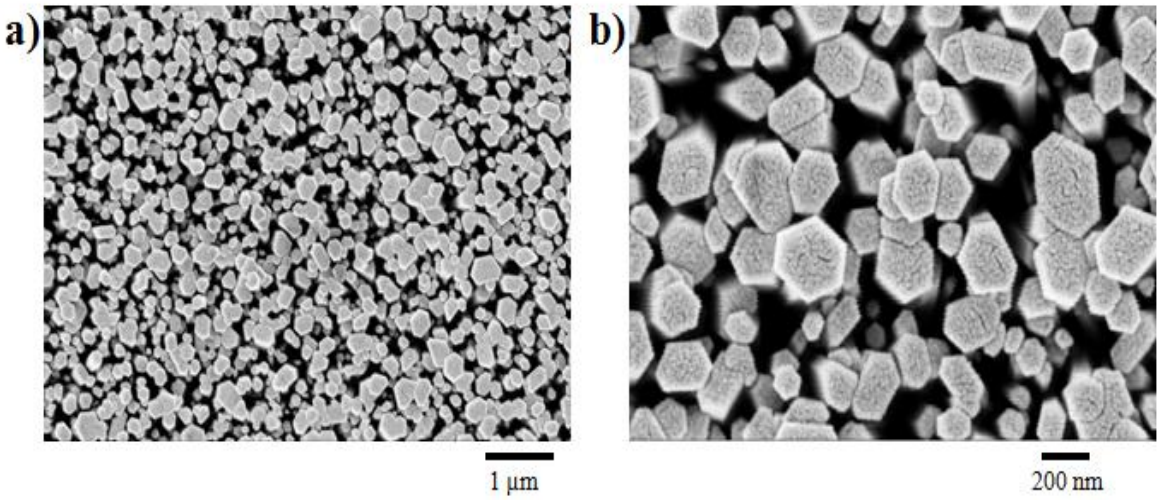

Figure 3.7 a) SEM images of ZnO nanostructures; b) close up SEM image of same ZnO nanostructures.

Finally, after many months, we were able to develop valuable insight about the entire fabrication procedure and optimize critical synthetic aspects regarding precursor concentration, growth temperature, and reaction time. Using optimal synthesis conditions of 10 mM precursor concentration, 70°C growth temperature, and 12 h reaction time, desirable ZnO nanowires were fabricated. Specifically, we wanted to look at the effect of the seed layer on the density of the nanowires. It was determined from the SEM images that the samples with the thicker seed layer gave denser arrays of nanowires, and these results can be seen in Figure 3.8. In both cases, the lengths of the nanowires in the array varied between 1-3 μm.

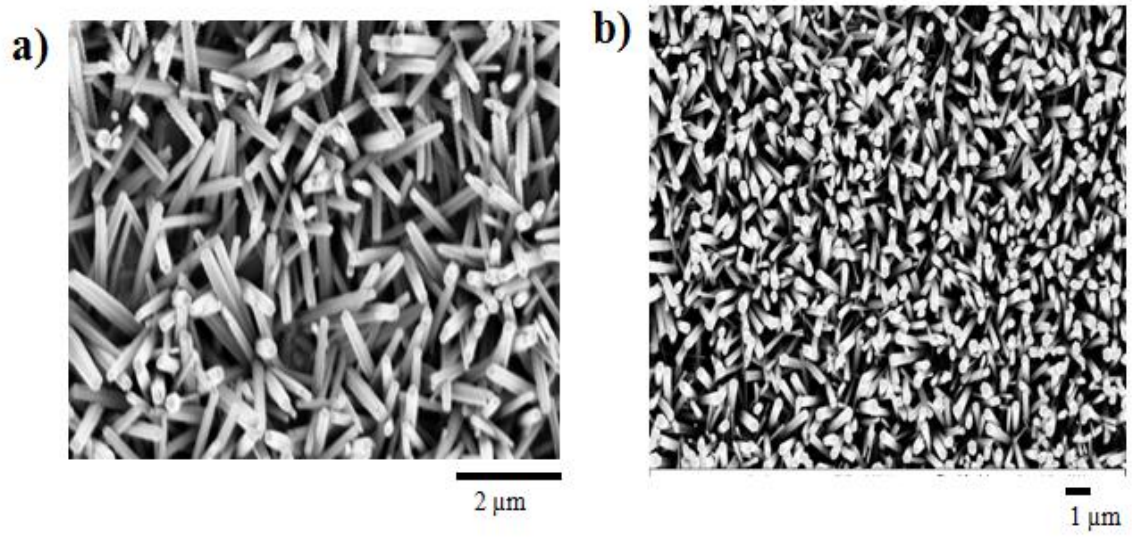

Figure 3.8 SEM images of 1D ZnO NW array. a) 10 mM @ 70°C for 24h on Si substrate using 4 coats of seed layer solution; b) 10 mM @ 70°C for 24h on Si substrate using 6 coats of seed layer solution.

Now that the fabrication process became more intuitive, the next step of the research plan was to grow the ZnO nanowires onto a new type of substrate, transparent conducting glass, which would be useful in the solar cell application. Studies were done to observe the characteristics of the ZnO nanowires fabricated on FTO substrates under various synthesis conditions (precursor concentrations ranging from 10-25 mM, growth temperatures ranging from 70-90°C, and reaction times from 5-24 h). For example, SEM images were analyzed for a study on reaction time, in which the precursor concentration and the growth temperature were kept constant at 10 mM and 80°C, respectively. Interestingly, the most desirable ZnO nanowires were produced at a reaction time of 12 h. It was clear that precursor concentration, growth temperature, and reaction time all have a notable effect on the ZnO morphology. Figure 3.9 shows SEM images of ZnO nanowires grown on the FTO conducting glass substrate using 10 mM precursor concentration,

80°C growth temperature, and 12 h reaction time; and again the affect of seed layer thickness is highlighted.

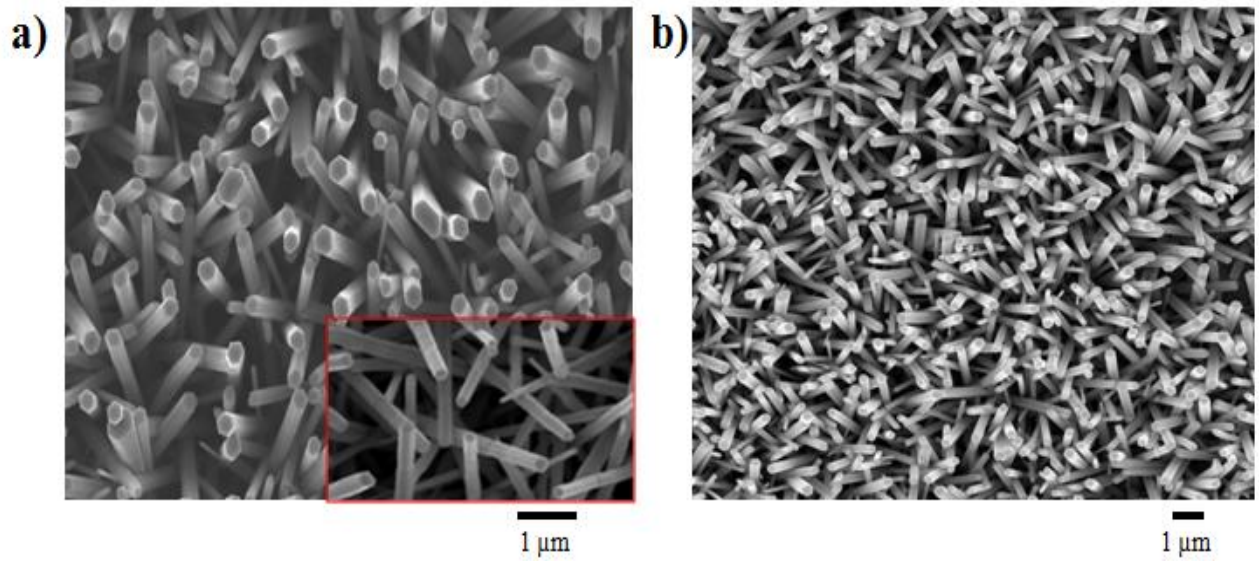

Figure 3.9 SEM images of 1D ZnO NW array. a) 10 mM @ 80°C for 12h on FTO substrate using 4 seed layers; b) 10 mM @ 80°C for 12h on FTO substrate using 6 seed layers.

The physical appearance of the nanowire arrays were as expected, with the hexagonal faces and reasonable aspect ratio. The nanowires were nearly 105 nm in diameter and about 2.5 µm in length. Furthermore, as expected, the samples with the thicker seed layer gave denser arrays of nanowires for the synthesis done using FTO substrates as well. The main results of the overall study are displayed in Table 3.1 and Table 3.2. It was found that the optimal synthesis conditions were 25 mM precursor concentration, 90°C growth temperature, and 5 h reaction time.

Table 3.1 Analysis of 1D ZnO NW Array at 10 mM Precursor Concentration

Growth Temperature (°C)	Reaction Time (h)	Length (± 0.01 μm)	Diameter (± 2 nm)	Density (x 10^8 per cm^2)
70	5	1.60	97	6.70
70	12	1.68	120	6.38
70	24	1.74	139	6.20
80	5	2.22	95	6.69
80	12	2.51	104	6.32
80	24	2.35	130	6.22
90	5	1.20	92	6.75
90	12	1.29	102	6.30
90	24	1.34	124	6.38

Table 3.2 Analysis of 1D ZnO NW Array at 25 mM Precursor Concentration

Growth Temperature (°C)	Reaction Time (h)	Length (± 0.01 μm)	Diameter (± 2 nm)	Density (x 10^9 per cm^2)
70	5	1.51	88	1.89
70	12	1.59	112	1.49
70	24	1.60	125	1.15
80	5	2.52	87	1.92
80	12	2.10	105	1.64
80	24	2.34	121	1.28
90	5	2.99	87	1.95
90	12	2.90	97	1.70
90	24	2.71	118	1.35

From the tables above, some specific conclusions can be drawn. First, the nanowires synthesized from the higher precursor concentration resulted in an array of more dense nanowires. This tells us that a higher degree of Zn^{2+} consumption leads to denser arrays. Furthermore, the increase of the ZnO NW density can be explained by the increase in the number of nuclei that form on the substrate as a means to compensate for the increase in the zinc chemical potential. Next, for both

precursor concentrations, the diameter of the nanowires tends to become larger at longer reaction times. This outcome is possibly due to the sidewalls of the nanowires being exposed to the precursor ions for a longer period of time causing continual lateral growth. On the other hand, while the lengths were slightly longer in the case of the 25 mM precursor solution, the length of the nanowires did not show a clear trend. The length has been known to not be affected by one single reaction parameter as much as the diameter. However, in the case of 25 mM precursor solution, the lengths increased slightly with increasing temperature. Yet, in the case of the 10 mM precursor solution, the lengths increased slightly as the temperature increased from 70-80°C; however, the lengths then decreased as the temperature increased from 80-90°C. This occurrence is possibly due to the fact that if the temperature is too high, then the reaction is sped up causing a faster depletion of Zn^{2+} ions required to continue growth in the vertical direction. Still, there must be an optimal combination of synthesis conditions to yield the longest possible nanowires.

Furthermore, it was assumed that if the substrates were continuously introduced to fresh growth solutions under the optimal synthesis conditions of 25 mM precursor concentration and 90°C growth temperature, the lengths of the nanowires could be enhanced. This idea stems from the fact that after a certain period of time during crystal growth, there is depletion of Zn^{2+} ions and growth ends. Thus, if the substrates are introduced into a fresh precursor solution, then there will be additional consumption of the Zn^{2+} to promote further growth of the nanowires. The SEM images in Figure 3.10 demonstrate the differences in nanowire length for one sample that was continuously exposed to fresh solutions every 2.5h for an entire 12.5 h period and another sample that was exposed to the same precursor solution for the entire 12.5 h period.

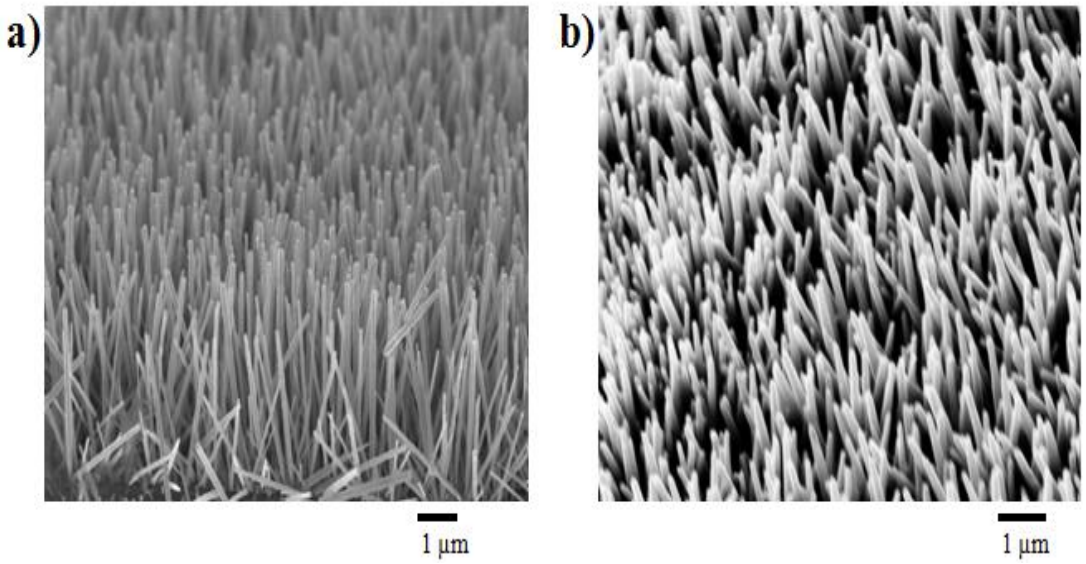

Figure 3.10 SEM images of 1D ZnO NW array. a) 25 mM @ 90°C on FTO substrate using 5 seed layers for 12.5h (refreshing the growth solution every 2.5h); b) 25 mM @ 90°C on FTO substrate using 5 seed layers for 12.5h in the same growth solution.

The crystal structure of the ZnO nanowire array grown on the FTO substrate was examined using XRD. Figure 3.11 shows an XRD pattern of the ZnO nanowire array. The remarkably enhanced (002) diffraction peak at 34.6° is much more intense than the other peaks, implying that these nanowires were perfectly oriented perpendicular to the substrate surface and that they were grown along the c-axis. The (002) diffraction peak also confirms the [001] as the fastest growth direction and verifies the high degree of crystallinity of the ZnO NWs. The XRD spectrum also shows signals at other degrees giving insight about slight growth in other directions, and these specific peaks are almost always evident in any of the XRD spectra found for ZnO in the literature.

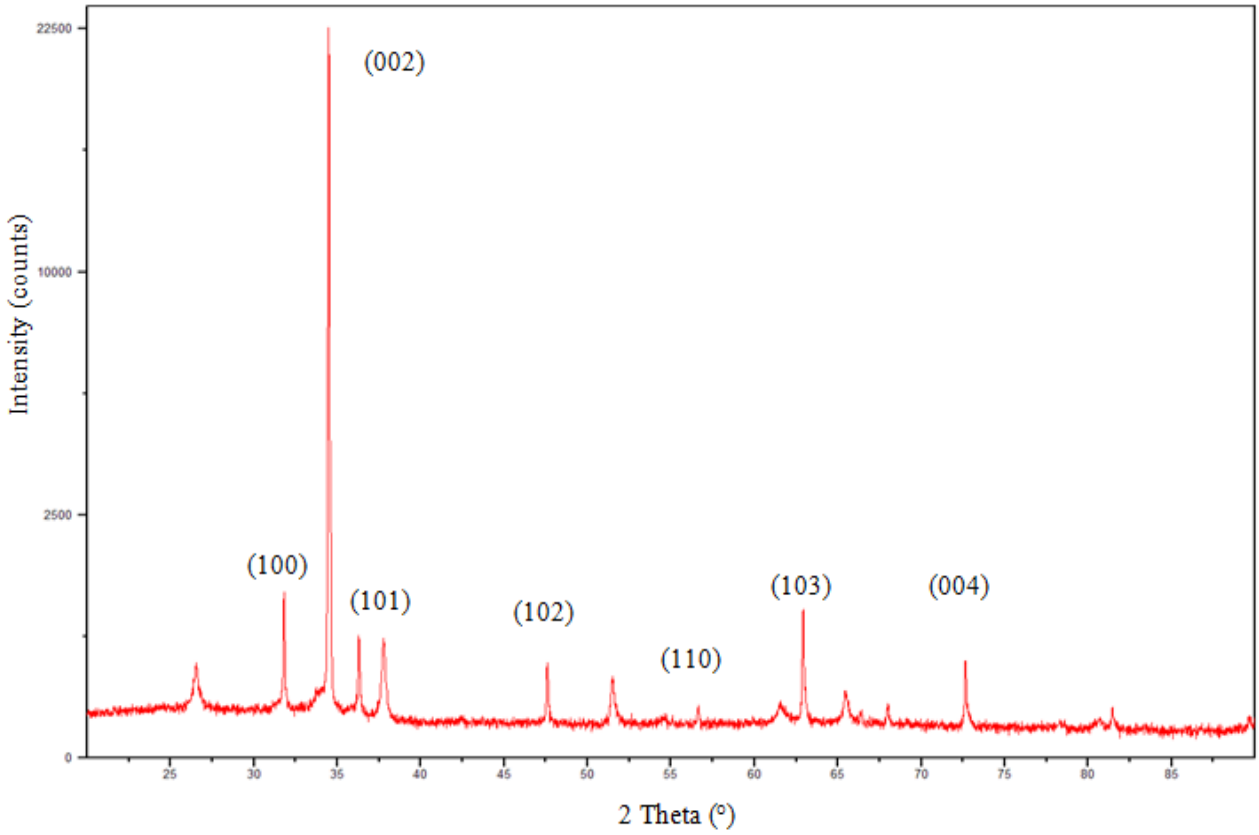

Figure 3.11 XRD spectrum of 1D ZnO nanowire sample.

3.4 Brief Summary

In this chapter, the research goal was to effectively fabricate 1D ZnO nanowires based on the hydrothermal growth method. The hydrothermal growth method is based on reacting equimolar concentrations of zinc nitrate hexahydrate and HMTA in an aqueous solution at relatively low temperatures compared to other ZnO nanowire synthesis techniques. The advantages of using the hydrothermal process is not limited to the employment of lower reaction temperatures, but also includes inexpensive production costs, process simplicity and less rigorous synthesis conditions. It was important to determine the optimal reaction conditions for synthesizing well crystallized ZnO nanowires that form hexagonal faces and grow perpendicular the substrate, as well as dense nanowire arrays with high aspect ratios. As determined from experimental synthesis, the optimal conditions for the growth of ZnO nanowires were based on a 25 mM equimolar precursor concentration, 90°C growth temperature, and 5 h reaction time. The lengths and diameters of these nanowires ranged between 1.5-3 μm and 85-125 nm, respectively. The XRD spectrum verified the crystallinity and vertical alignment of the ZnO nanowires grown on FTO substrates under these optimal conditions.

CHAPTER 4

MATHEMATICAL MODEL FOR ZINC OXIDE NANOWIRE DYE-SENSITIZED SOLAR CELLS

4.1 Introduction

Dye-sensitized solar cells have yet to produce comparable performance to those of other solar cell technologies (e.g., silicon based multi-junction cells, single junction GaAs-based cells, and Cu(In, Ga)Se_2 cells based on thin film technologies) [3]. These other technologies, however, have shown to be very expensive for large-scale production. Therefore, many researchers are interested in dye-sensitized solar cells because of their potential to provide both cost efficient and process efficient renewable energy. The maximum efficiency, however, has leveled off to ~12% [7]. Thus, considering that Grätzel et al. produced 10% efficiency DSSCs in 1993[120], there has not been much improvement in experimental efficiencies in nearly 20 years. Therefore, it is important to get a thorough understanding of how the DSSC performance is being affected by specific components of the cell as well as specific processes of its fundamental mechanism. The use of models allows us to investigate how specific properties of the cell components (e.g., the semiconducting material used as the photoanode, the dye, and the electrolyte redox couple) affect DSSC efficiency. Thus, with the insight gained from various models, we can then engineer new materials that possess the necessary qualities that yield higher conversion efficiencies.

Many models in the literature discuss the use of responses from IMPS and IMVS (intensity modulated photocurrent spectroscopy and intensity modulated photovoltage spectroscopy, respectively) to reveal how DSSC performance is being affected by charge dynamics. Specifically, IMVS is used to measure the respective time constants for charge

recombination at open circuit, while IMPS is used to measure the respective time constants for the combined processes of charge collection and charge recombination at short circuit. Schlichthörl et al. have developed a model in which IMVS and IMPS are used to determine the charge collection efficiency of TiO_2 DSSCs [121]. This model will be discussed further in this chapter. Another example of models of DSSCs comes from the work of Penny et al. [122]. In their work, they highlighted a mathematical model that is specifically based on the one-dimensional transport of TiO_2 NP DSSCs in which the sensitizer is N3 dye and the redox electrolyte couple is I^-/I_3^- (with Li^+ as the solution cation); however the framework of their model can be used to study other DSSC systems [122]. Furthermore, their model investigated the effects of the separate charge transfer processes occurring at the TiO_2/dye/electrolyte interface on DSSC performance [122]. A commissioned experimental study confirmed the results of their model simulation [122]. Another example of how models are used to investigate the factors that influence the performance of DSSCs is shown by the work of Barnes et. al (under the leadership of B. O'Regan, co-author of first report of DSSCs) [123]. Specifically, they presented a numerical model based on TiO_2 DSSCs that illustrates how the various charge transfer reactions affect DSSC efficiency under various conditions [123]. Moreover, their model gives an account for both the time dependent and independent effects on DSSC performance. Their time dependent simulations, specifically, were validated with experimental data obtained from transient photocurrent and photovoltage measurements at open circuit [123]. Lastly, Hill et al. provided an interfacial and bulk charge transport model for DSSCs based on nanowire arrays with a conductive core and TiO_2 shell [124]. In their report, the explicit function of the interfacial electric field and its effect on the performance of nanowire-based DSSC was investigated. Their study revealed that the presence of the internal electric field allowed the reaction rate for

electrons recombining with oxidized species in the electrolyte to decrease, which in turn improved the fraction of electrons collected at the anode for electrical use [124]. Thus, better DSSC performance was observed. Their model computations were also validated with experimental data [124].

Here, the goal of our model is to build on the previous models (especially the model of Schlichthörl et al.) and determine how the ZnO nanowire geometry is affecting the DSSC performance. Specifically, we look at how the nanowire length, radius, and density affect the incident photon-to-current conversion efficiency (IPCE) at a single wavelength (543 nm) in which the N719 dye has maximum light absorption. The geometry that the ZnO nanowires take on is a hexagonal wire. Therefore, in this model the surface area, which will prove to be very key in the determination of the IPCE, is determined from the geometric calculations of a hexagonal prism. The maximum IPCE based on experimental measurements usually does not reach beyond 80%, which is mainly due to the negative effects of reflection losses and light absorption by the electrolyte [125]. However, not taking these effects into account, this model gives an approximation of what the theoretical IPCE should be for various physical dimensions of the ZnO nanowires, and then approximates the optimal dimensions that will yield maximum IPCE under specific model conditions.

4.2 Device Geometry and Modeling Physics

The model is designed to explore how the physical dimensions of the ZnO nanowire array (e.g., the length, radius, and density on the glass substrate surface) affect the results of the incident photon-current conversion efficiency (IPCE). In the model the ZnO nanowire array is represented by a film on the substrate, where the thickness of this film is the same as the length of a single nanowire (where all the nanowires are at the same length). Thus, we can then imagine the cell as simply an area of film on the surface with film thickness, d, as shown in Figure 4.1.

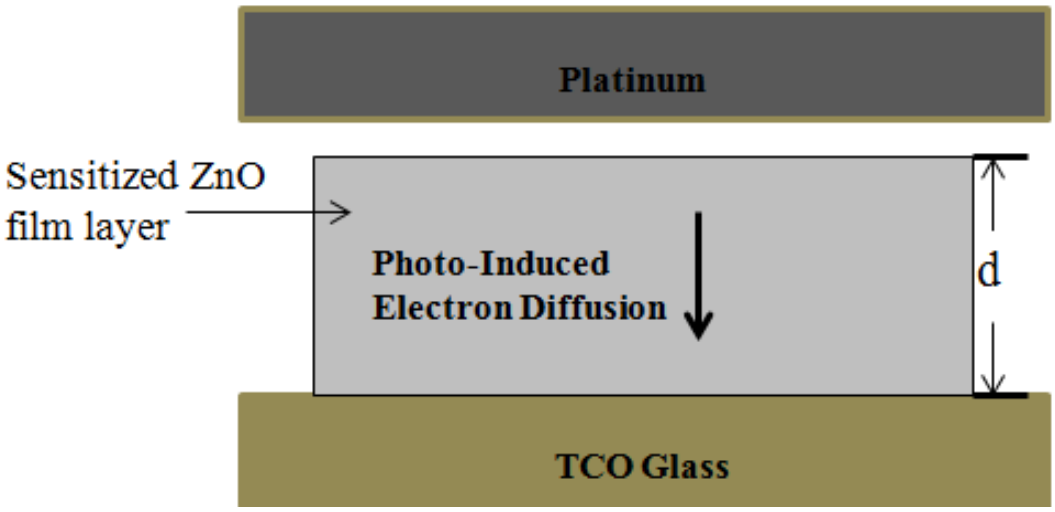

Figure 4.1 Illustration of a certain film thickness, d, of ZnO nanowires on the glass substrate and electron diffusion processes of the DSSC.

Specifically, the ZnO nanowires take on the geometric shape of a hexagonal prism. This geometric shape is used to determine the surface array of the ZnO nanowire array. Figure 4.2 provides a schematic of the actual DSSC based on ZnO nanowires. From this figure, you can see that the nanowires take on the actual geometry of a hexagonal prism.

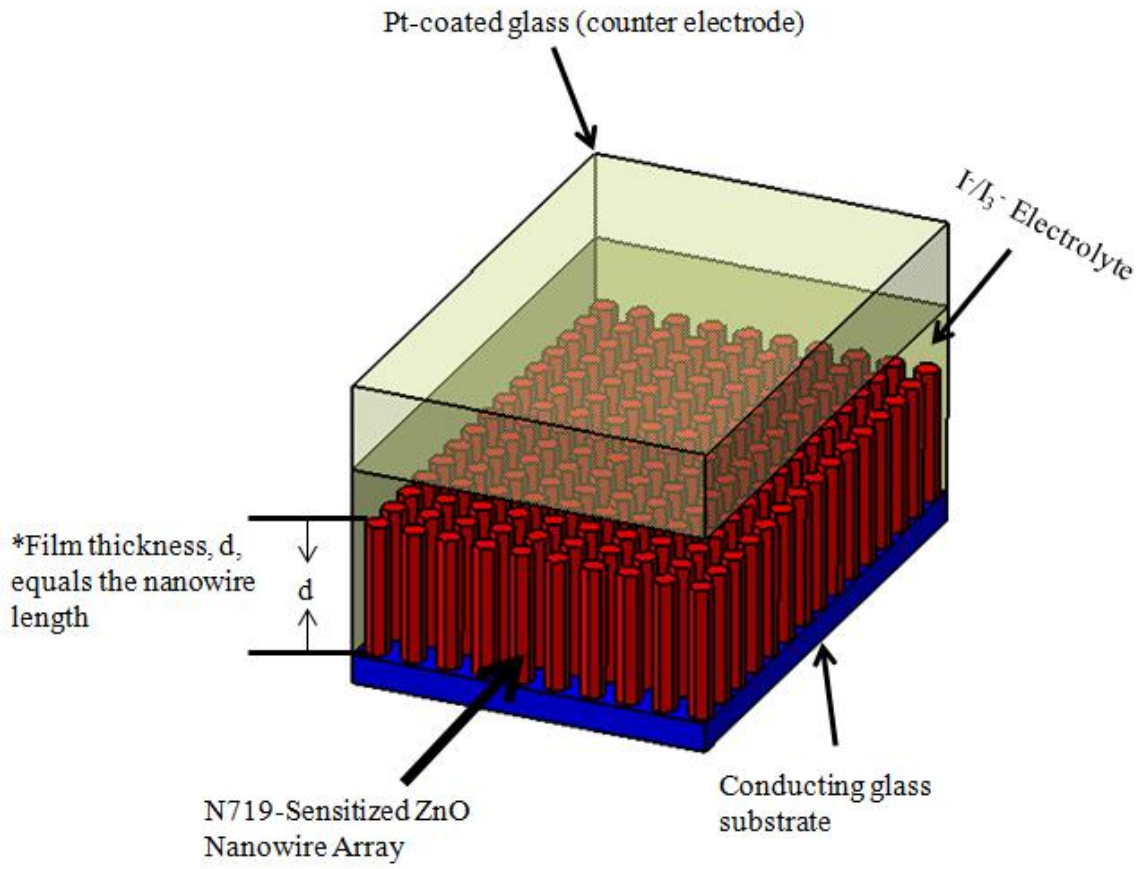

Figure 4.2 Illustration of the ZnO nanowire array-based DSSCs.

Model Basis and Assumptions:

- Light absorption by the electrolyte, ZnO and conducting glass is neglected as well as light reflection losses
- IPCE is calculated based on a single wavelength (543 nm)
- Light intensity is assumed to be constant
- Electron transport is based on diffusion, and the effects of an internal electric field are neglected
- The loss of injected electrons via recombination is proportional to the electron concentration in ZnO and the electron diffusion current is proportional to the gradient of the electron concentration (*also assumed in existing model by Schlichthörl et al. [121])
- Electron concentration profile is under steady-state conditions (*also assumed in existing model by Schlichthörl et al. [121])
- Free and trapped electrons are in thermal equilibrium(*also assumed in existing model by Schlichthörl et al. [121])
- Electron recombination rate is assumed constant. The literature states that the rate of recombination is proportional to the light intensity [121], and for this model the light intensity is constant → constant rate of electron recombination.
- The electron injection efficiency, ϕ_{inj}, is assumed to be constant at 100%, so the parameters used to calculate the ϕ_{inj} have been set strategically within a feasible range as obtained from the literature to yield 100% injection efficiency [120] (given in Table 4.1)
- All the nanowires in the array are treated as having a uniform height and radius and the nanowires do not overlap in the array (The geometric dimensions are carefully monitored in the model to ensure that total cross section of the array (cm^2) does not exceed the active substrate area (which is the projected surface area).

The surface area of the film, A_{array} (cm^2) is calculated by the surface area of a single nanowire, A_{NW} (cm^2), times the number of nanowires on the substrate.

$$A_{array} = A_{NW} N A_{a,} \quad \textbf{(4.1)}$$

where the number of nanowires on the substrate is determined from the product of the nanowire density, N (number per cm^2 of projected surface area), and the projected surface area, A_a (cm^2). A_{NW} is given by Equation 4.2 [126, 127],

$$A_{NW} = \frac{3\sqrt{3}r^2}{2} + 6rd, \quad \textbf{(4.2)}$$

where d is the thickness of the ZnO film (cm: *length of nanowire) and r is the nanowire radius (cm) which is shown in Figure 4.3 as the distance from a vertex to the center (i.e., radius is equal to the length of the sides for a regular hexagonal prism). The surface area includes the top and sides of the nanowire only because the dye adsorbs to this specific portion of the nanowire surface.

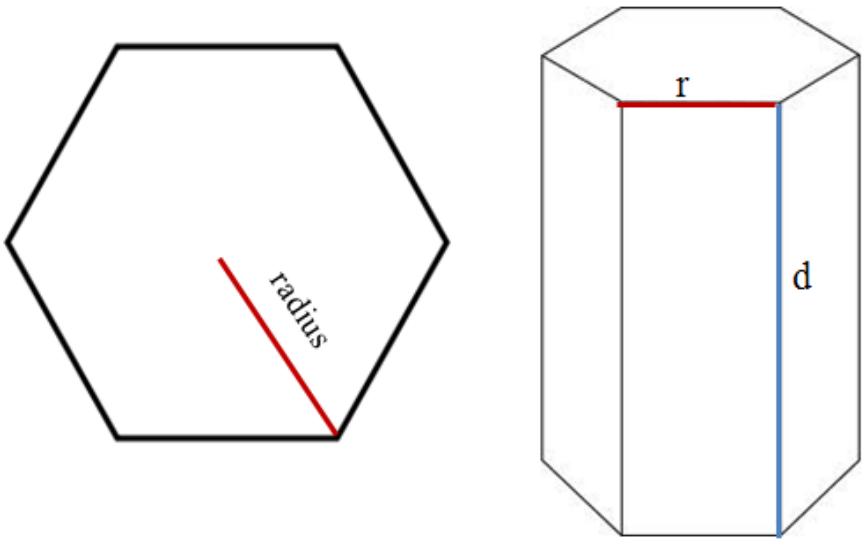

Figure 4.3 Schematic of nanowire dimensions to calculate surface area. Adapted from [128]

Also, important to note, is the cross sectional area of the base of the ZnO nanowire, $A_{cross\text{-}sec.}$ This is needed to ensure that the nanowires do not overlap. The total cross section of the array should not exceed the total surface area of the substrate. This total cross section of the array (cm^2) is determined by multiplying the cross sectional area of the base of one single nanowire, $A_{cross\text{-}sec}$ (cm^2), by the total number of nanowires on the projected surface area. $A_{cross\text{-}sec}$ can be calculated by Equation 4.3 [126, 127],

$$A_{cross-sec} = \frac{3\sqrt{3}}{2} r^2 \ . \qquad \textbf{(4.3)}$$

Governing Model Equations:

The overall objective of the model is to determine the IPCE, the incident photon-to-current conversion efficiency. IPCE is determined using Equation 4.4 [125],

$$IPCE(\lambda) = LHE \times APCE, \qquad \textbf{(4.4)}$$

where LHE is the light harvesting efficiency and is defined as the fraction of incident photons that are absorbed by the dyed electrode. LHE can be determined from Equation 4.5 [120],

$$LHE = 1 - 10^{-\Gamma\sigma(\lambda)}, \qquad \textbf{(4.5)}$$

where Γ is the number of moles of sensitizer per square of projected surface area of the film (mol/cm^2), and σ is the absorption cross section (cm^2/mol) [120]. The Γ value is obtained by first calculating the number of moles of adsorbed dye by taking the dye loading amount (mol/cm^2 of the ZnO array) and multiplying it by A_{array} (cm^2). Then the number of moles of dye is divided by the projected surface area of the film, A_a. The σ value is based on the dye properties and this value can be obtained from the decadic extinction coefficient (units of M^{-1} cm^{-1}) by multiplication with 1000 cm^3/L [120].

The APCE is the absorbed photon to current efficiency and is defined as the portion of absorbed photons that generate electrons in the external circuit. APCE is the product of the electron injection efficiency, ϕ_{inj}, and the charge collection efficiency, η_c as seen in Equation 4.6 [125],

$$APCE = \phi_{inj}\,\eta_c\,. \qquad \textbf{(4.6)}$$

The electron injection efficiency, ϕ_{inj} is determined using Equation 4.7 [120],

$$\phi_{inj} = \frac{k_{inj}}{\tau^{-1}+k_{inj}}, \qquad \textbf{(4.7)}$$

where k_{inj} is the rate constant for electron injection (s^{-1}) and τ is the excited –state lifetime in the absence of injection(s) [120]. In the model k_{inj} and τ have been set to 5 x 10^{11} s^{-1} and 6 x 10^{-8} s, respectively [120] to yield a ϕ_{inj} of 100% as stated in the model assumptions.

The charge collection efficiency, η_c, is calculated based on the expression in Equation 4.8 that was derived from the transport model for DSSCs developed by Schlichthörl et al. [121],

$$\eta_c = \frac{\alpha\left[2\alpha\exp(-\alpha d)-\left(\alpha-L^{-1}\right)\exp\left(L^{-1}d\right)-\left(\alpha+L^{-1}\right)\exp\left(-L^{-1}d\right)\right]}{[1-\exp(-\alpha d)][L^{-2}-\alpha^2][\exp(L^{-1}d)+\exp(-L^{-1}d)]}, \quad \textbf{(4.8)}$$

where α is the light absorption coefficient of the cell (cm^{-1}), d is the film thickness of ZnO (cm), and L is the electron diffusion length (cm) [121]. The electron diffusion length can be evaluated from Equation 4.9 [121]:

$$L = \sqrt{{mD_{cb}}/{k_r}}, \quad \textbf{(4.9)}$$

where D_{cb} is the electron diffusion coefficient in the conduction band (cm^2/s), m is the ratio of the photo-induced electrons in the conduction band (n_{cb}) to the total number of photo-induced electrons in both the conduction band (n_{cb}) and the trap states (n_t), and k_r is the recombination rate constant (s^{-1}) [121]. The absorption coefficient is determined from the dye coverage across the ZnO film as shown in Equation 4.10 [129-131],

$$\alpha = \frac{\sigma\Gamma}{d}. \quad \textbf{(4.10)}$$

Hence, with ϕ_{inj} and η_c calculated, the APCE can then be determined.

The charge collection efficiency is a function of the absorption coefficient because the amount of electron recombination is affected by how many photo-induced electrons are generated due to the amount of light absorption of the dye at various positions along the thickness of the film. In this model and in the model derived by Schlichthörl et al., a constant rate of recombination on the electron concentration in the ZnO film (linear dependence) is assumed [121]. This concept is discussed later under the model limitations section. The expression for charge collection efficiency comes from an existing model developed by Schlichthörl et al. for the evaluation of the charge collection efficiency of DSSCs based on TiO_2 nanocrystalline particles [121]. Their model of the charge collection efficiency was based on a steady- state electron concentration profile for electron transport via diffusion across the TiO_2 film[121]. As mentioned earlier, the ZnO nanowire array of a certain uniform nanowire length can be represented by a film of ZnO with a certain thickness. Moreover, in this model, the major transport process that is applied is diffusion. Therefore, the model by Schlichthörl et al. can be used to represent the charge collection efficiency for any type of DSSC that has the same charge transport dynamics. The actual geometry of the semiconductor film is taken into account when the specific surface area of the film is needed to evaluate the Γ value that is required in both the LHE and the APCE. Moreover, Wong et al., have also used the model by Schlichthörl et al. to compare the differences in the charge collection efficiency of four different types of DSSC: 1) ZnO nanowire-nanoparticle composite; 2) vertical ZnO nanowires; 3) TiO_2 nanoparticles; and 4) horizontal TiO_2 nanowires [132].

4.3 Model Results and Discussion

The model shows results based on the N719 dye sensitizer. In this model, the film thickness (length of nanowires) was varied, while the radius and the density remained constant. Three specific constant radii were investigated (25nm, 50 nm, and 100 nm). To ensure that there is no overlapping of the nanowires, we calculated the maximum density that could exist at those specific radii so that the total cross section of the ZnO film will not exceed the projected surface area of the substrate. Thus, for constant r set to 100 nm, N should be $\leq 3.6 \times 10^9/cm^2$ of projected surface area. For constant r set to 50 nm, N should be $\leq 1.45 \times 10^{10}/cm^2$ of projected surface area, and lastly for constant r set to 25 nm, N should be $\leq 5.85 \times 10^{10}/cm^2$ of projected surface area. In all these cases, the total surface coverage (i.e., percentage of the projection area are covered by nanowires) does not exceed 95%. As you can see, for larger radii, the density must be a lot less to prevent nanowire overlap.

For Case I, we will first look at the condition: r = 50 nm, and $N= 1 \times 10^9/cm^2$ of projected surface area. The fixed constant parameters are given in Table 4.1.

Table 4.1 Constant Model Parameters.

Constant Model Parameters	Modified Values from Literature Reported Data
$\varepsilon(\lambda)$ [N719 dye]	1.4×10^4 $M^{-1}cm^{-1}$ [111]
λ	543 nm [111]
Dye loading amt.	2.25×10^{-10} mol/cm^2 [modified from experimental]
A_a	1.0 cm^2
k_{inj}	5×10^{11} s^{-1} [120]
τ	6×10^{-8} s [120]
m	0.7 [10, 132-134]
D_{cb}	0.1 cm^2/s [10]
k_r	1000 s^{-1} [109, 134]

Inputting the parameters from Table 4.1 and the physical dimensions provided earlier for Case I, an IPCE plot as a function of film thickness was generated as shown in Figure 4.4. Table 4.2 provides a detailed account of how the IPCE was determined based on the LHE and the APCE.

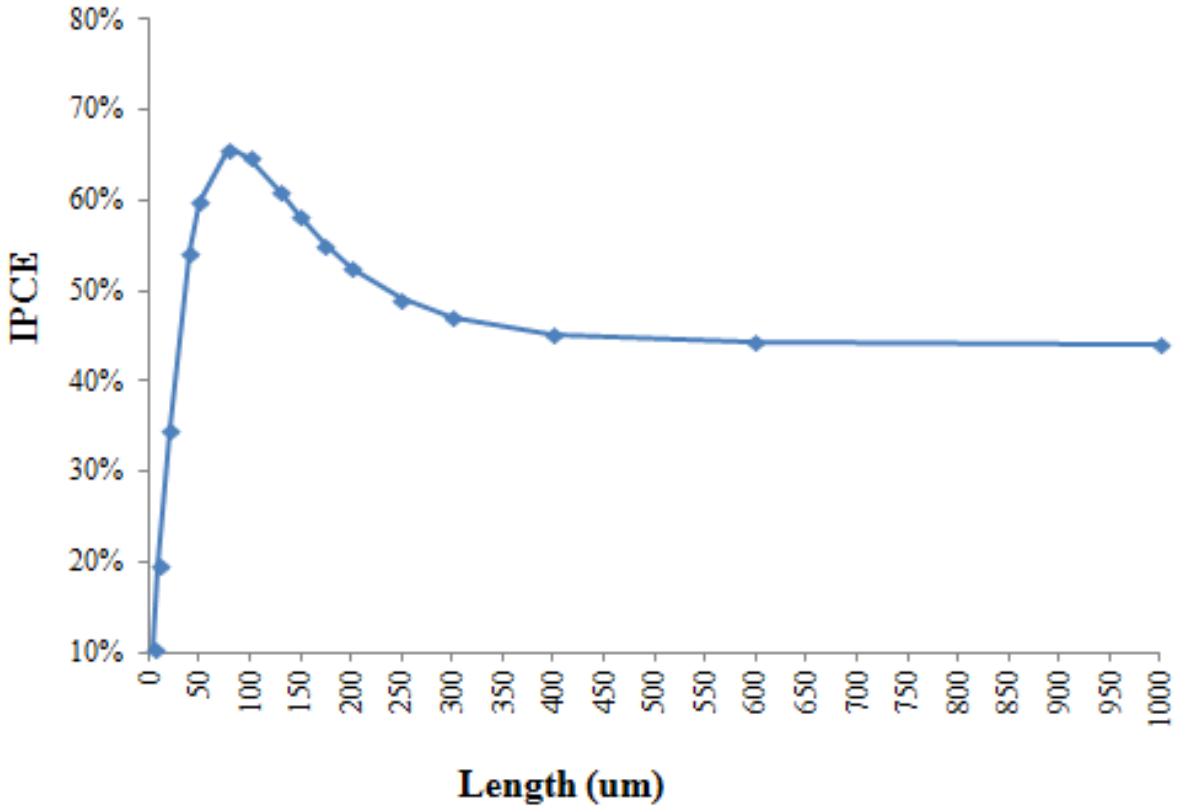

Figure 4.4 Effect of length of the ZnO nanowires on the IPCE of the DSSC at constant radius of 50 nm and constant density of $1x10^9$ /cm^2 of projected surface area (or ~10% surface coverage).

Table 4.2 Case I Model Results of DSSC performance characteristics at varying lengths of the ZnO nanowires with the radius and density set constant to 50 nm and 1 x 10^9 /cm^2 of projected surface area, respectively.

Length (μm)	Array Surface Area (cm^2)	LHE (%)	APCE (%)	IPCE (%)
5	15	10.39%	99.88%	10.38%
10	30	19.63%	99.53%	19.54%
20	60	35.35%	98.18%	34.70%
40	120	58.16%	93.35%	54.29%
50	150	66.34%	90.19%	59.84%
80	240	82.48%	79.74%	65.77%
100	300	88.66%	73.12%	64.83%
130	390	94.10%	64.84%	61.02%
150	450	96.18%	60.54%	58.23%
175	525	97.78%	56.36%	55.11%
200	600	98.71%	53.27%	52.58%
250	750	99.57%	49.31%	49.10%
300	900	99.85%	47.14%	47.07%
400	1200	99.98%	45.22%	45.21%
600	1800	100.00%	44.31%	44.31%
1000	3000	100.00%	44.16%	44.16%

From the results shown in Figure 4.4 and Table 4.2, it is clear that geometry of the ZnO plays a critical role in the IPCE results. Firstly, since the radius and density were set constant, the surface array of the ZnO film was varied due to the increase in length. As the surface area was increased, the LHE continually increased. This makes sense because as you increase the surface area, the amount of dye molecules on the ZnO surface increases, thus increasing the amount of light absorption. On the other hand, as the surface area increased due to longer nanowires, the

APCE continually decreased. This occurs due to the steady decrease in the charge collection efficiency since the electron injection efficiency was constant at 100%. The charge collection efficiency decreasing with increasing length can be explained by the competing processes of electron recombination and electron diffusion. Diffusion length, L, is defined as the average distance an injected electron can travel through the cell before the occurrence of charge recombination [129]. Thus, when L > d, only a low percentage of injected electrons will not be collected at the photoanode; and likewise, when the L< d, a higher percentage of the injected electrons will not make it to the charge collecting substrate, and thus the charge collection efficiency decreases. Therefore, it is seen desirable to utilize materials with fast electron transport (high diffusion coefficients) to obtain long diffusion lengths. It has been reported consistently in the literature that the D_{cb} is in the range of 0.05-0.5 cm^2/s for ZnO nanowires, which is several orders of magnitude higher than that of TiO_2 nanoparticles [10]. In this model, the D_{cb} is fixed at 0.1 cm^2/s, which is in the middle of the experimental range given in the literature for ZnO nanowires. Ultimately, because of the steady increase in LHE until it reaches 100% coupled with the steady decrease in APCE, we observe an IPCE trend that increases up to a certain maximum (in this case 65.77% IPCE at the corresponding nanowire length of 80 μm), and then decreases for longer nanowires. Next, Figures 4.5 and 4.6 illustrate the ability to reach higher IPCE values once the surface area is improved by varying the radii and densities under the same fixed parameters in Table 4.1. For example, in Figure 4.6, when the density is increased from $1x10^9/cm^2$ to $1x10^{10}/cm^2$ (i.e., surface coverage is increased from 6% to 65%) with the radius held constant at 59 nm, the maximum IPCE reaches 97% corresponding to 20 μm length nanowires. A higher IPCE is reached at 20 μm in this case (compared to only 35% at 20 μm in the case of the $1x10^9/cm^2$ density) because the surface area was increased significantly from 60

cm^2 to 600 cm^2, leading to 100% LHE at this length, and the absorption coefficient is also increased by an order of magnitude (from 95 cm^{-1} to 950 cm^{-1}) allowing for a slower rate of decrease in the charge collection efficiency. Therefore the IPCE is reaches much higher values at shorter nanowire lengths and then tails off at still fairly high IPCE values at longer nanowire lengths.

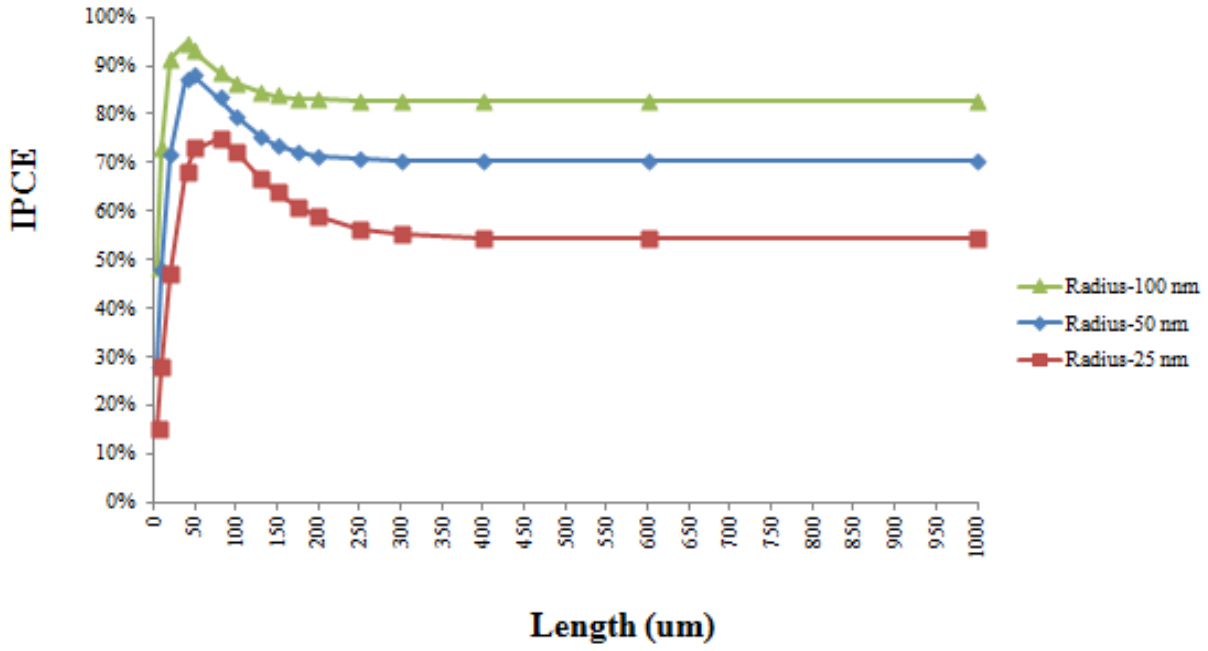

Figure 4.5 Effect of length of the ZnO nanowires on the IPCE of the DSSC at a constant density of $3x10^9$ /cm^2 of projected surface area and varying constant radii.

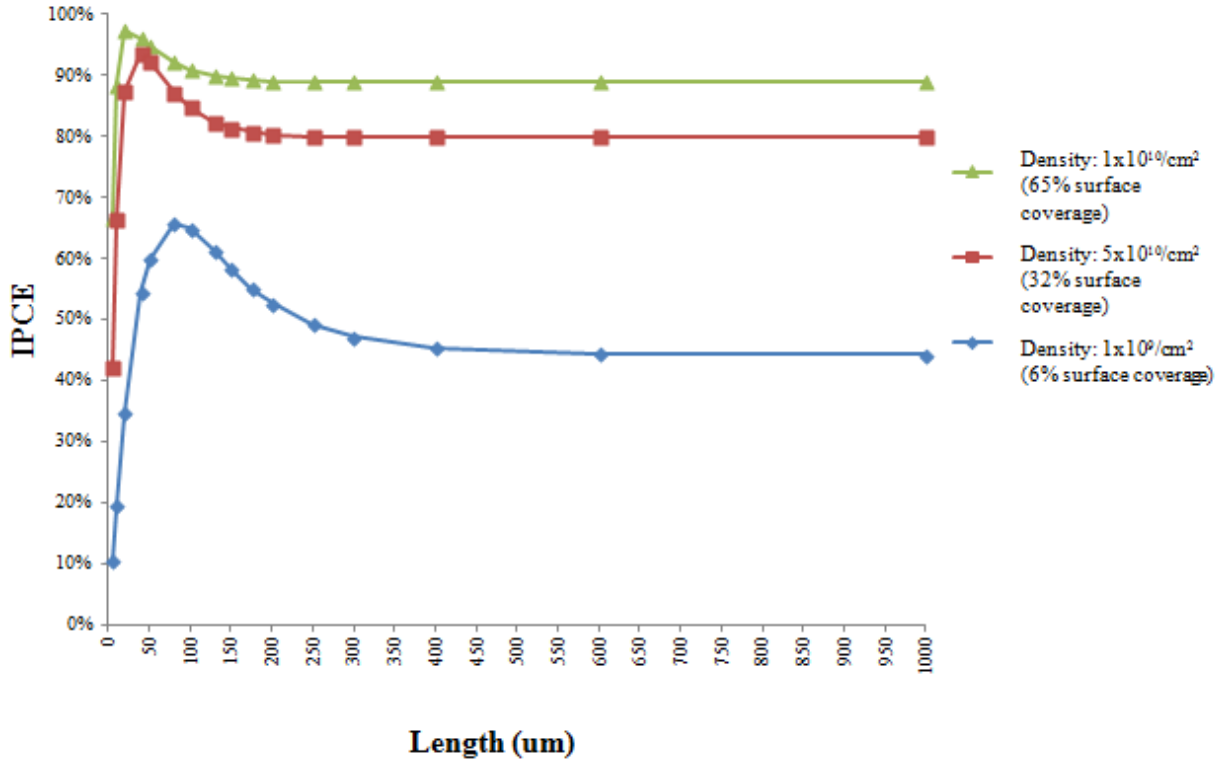

Figure 4.6 Effect of length of the ZnO nanowires on the IPCE of the DSSC at a constant radius of 50 nm and varying densities.

The amount of dye adsorption on ZnO is very crucial in obtaining high LHE values and high absorption coefficients. Model investigations have revealed that for N719 sensitized cells at 543 nm wavelength of light (corresponding to maximum absorption), the light harvesting efficiency should be 100% for Γ values on the on the order of 10^{-7} (mol/cm^2) or higher. In Case I, the dye loading was 2.25 x 10^{-10}/cm. For Case II, another dye loading is investigated. Calculations for the determination of our experimental dye loading amount can be found in Appendix A. Figure 4.7 compares the IPCE results of nanowires with a constant radius of 50 nm and constant density of 1x10^9/cm^2 with different dye loadings (2.25 x 10^{-10}/cm^2 and 2.0 x10^{-9}/cm^2), and all other parameters are fixed at values in Table 4.1.

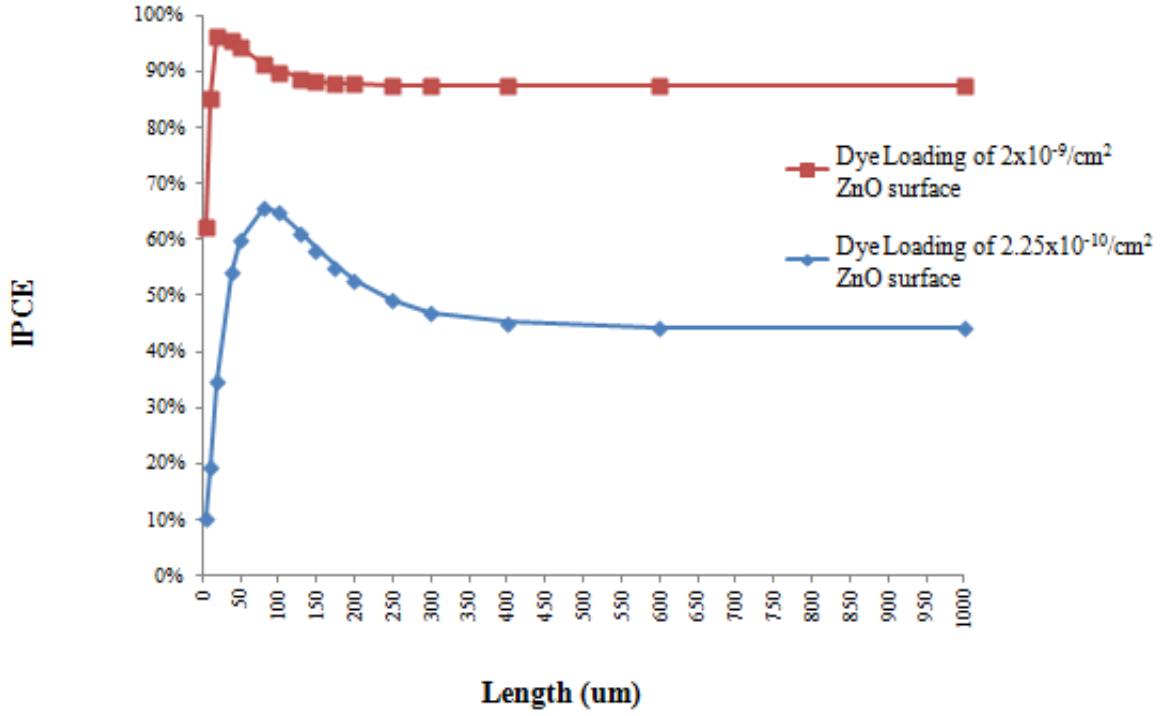

Figure 4.7 Effect of length of the ZnO nanowires on the IPCE of the DSSC at a constant radius of 50 nm and constant density of 1 x10^9 /cm^2 of projected surface area for different dye loadings.

Seen from the figure above, when the dimensions are the same, a higher dye loading plays an even greater role in producing high IPCE values. It should be noted, however, that further increases in the dye loading amount may not lead to higher (or steady) IPCE values because with very thick layers of the dye, some of the dye molecules may not be able to absorb the light. Furthermore, when the dye loading amount increases to some critical level, the IPCE decreases due to a decrease in the LHE. This model allows you to approximate the specific nanowire array dimensions and specific dye loading that is necessary to yield maximum light absorption. Additionally, the properties of the dye (e.g., the extinction coefficient) play a crucial role in the surface area needed to absorb high levels of light. Utilizing dyes with high extinction coefficient

allows greater light absorption, which is very advantageous for shorter nanowire lengths and low dye loading amounts.

For Case III, we will look at the effects of having a slower recombination rate. Ideally, in addition to having a material with high electron diffusivity, in order to obtain a long diffusion length, the presence of trap sites needs to be low in order to yield high m values and the recombination rate needs to be slow in order to yield low k_r values. The literature has reported that for ZnO nanowires, there are fewer sites for trapping electrons [10, 132-134]; therefore, we have set m to 0.7 a reasonably high fraction of electrons in the conduction bands to the sum of electrons in the conduction band and in trap sites. Looking specifically at the effect of the recombination rate constant on IPCE in Figure 4.8, the k_r is varied between 10 -1000 s^{-1}, with the radius set constant at 50 nm, the density set constant at 1.0 x10^9/cm^2 projected surface area. All other parameters are fixed at values given in Table 4.1.

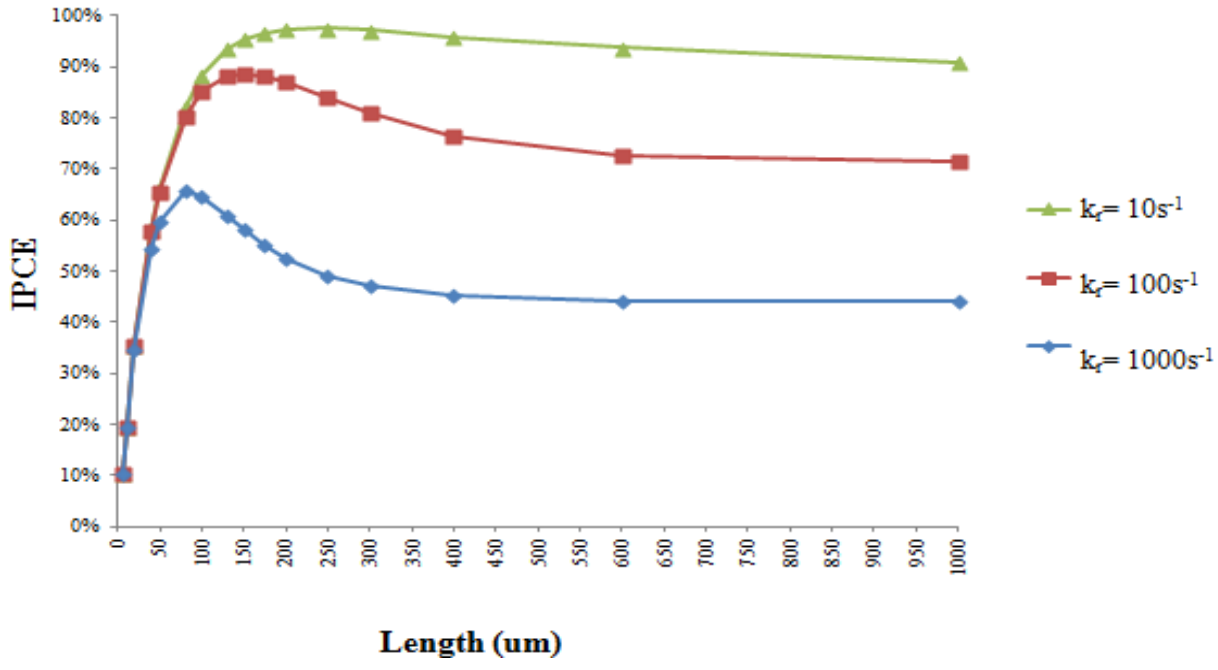

Figure 4.8 Effect of length of the ZnO nanowires on the IPCE of the DSSC at a constant radius of 50 nm and constant density of 1 x10^9 /cm^2 of projected surface area.

The results of Figure 4.8 clearly show that the lowest recombination rate constant gives higher IPCE values (nearly 100%) for long nanowires (lengths > 100 μm). Slower recombination rates allow for greater diffusion lengths; therefore high charge collection efficiencies can be obtained. But ultimately there has to be an optimal combination of the physical dimensions (i.e., surface area), dye loading, as well as recombination rate to yield both 100% LHE and 100% APCE to give the maximum obtainable IPCE. There are various combinations of the physical dimensions, dye loading, and recombination rate constants that can yield a maximum IPCE value.

The model can be used to identify which specific conditions are needed to yield maximum IPCE values. For an example, using the fixed parameters from Table 4.1, nanowire arrays with a nanowire radius of 50 nm, nanowire length of 20 μm, and density of 1.45 $x10^{10}$ /cm^2 of projected surface area (where surface coverage is ~95%, surface area is ~870 cm^2, and the absorption coefficient is ~1375 cm^{-1}), the IPCE(543nm) is ~100% for a N719 sensitized ZnO nanowire DSSC. Other ideal conditions can yield maximum IPCE values. Moreover, lower dye loadings and faster recombination rates would require greater surfaces areas to yield maximum IPCE results, and vice versa.

Findings from the model reveal another example of an optimal set of model conditions that yields perfect IPCE at 543 nm for lengths ≤ 1000 μm. In this case, the radius is set to 50 nm, the density is 1.45 $x10^{10}$ /cm^2 (with a surface coverage of ~95% and absorption coefficient of ~12,200 cm^{-1}), the dye loading is $2.0x10^{-9}$ /cm^2 ZnO surface, m is 0.7, k_r is 7 s^{-1}, and D_{cb} is 0.1 cm^2/s. More importantly, in this case, the diffusion length is 1000 μm, so for all lengths investigated (5-1000 μm), the diffusion length, L ≥ film thickness, d, which leads to perfect charge collection efficiency. Experimental measurements of long diffusion lengths of 1000 μm for ZnO nanotubes have been reported in the literature [109]. Also, the surface coverage and dye

loading are optimal so that perfect light harvesting efficiency is attained for all investigated lengths. Therefore, 100% IPCE is obtained for all of the investigated lengths up to 1000 μm under these specific conditions.

Model Validation:

While we have not measured the % IPCE experimentally for our ZnO nanowire DSSCs, the model can be validated with experimental IPCE values from the literature. It is quite difficult to find experimental reports that provide data for all the parameters that are necessary for this model; however, by comparing experimental IPCE values from reports that provide information about the ZnO nanowire geometry, we should be able to get a reasonable validation for this model.

Law et al. reported synthesized ZnO nanowires with lengths ~16 μm, radius of ~65 nm, and nanowire density on the order of $10^9/cm^2$ [10]. They also report a Γ value of $10^{-8}/cm^2$. They measured an IPCE (543 nm) value ~ 35% for their N719-sensitized ZnO nanowire DSSC [10]. Using these values in the model, with the fixed parameters listed in Table 4.1, this model approximates an IPCE (543 nm) value of 41.53%. The reason for the slightly higher IPCE values in the model may be attributed to the fact that the model does not take into account the efficiency losses due to light absorbed by the electrolyte.

Additionally, Baxter et al. reported synthesized ZnO nanowires with lengths ~8 μm, radius of ~78 nm, and nanowire density of $5x10^8/cm^2$ [81]. They did not report any dye loading data or Γ value. They measured an IPCE (543 nm) value ~ 7 % for their N719-sensitized ZnO nanowire DSSC [81]. Using these values in the model, with the fixed parameters listed in Table 4.1 including the dye loading that is necessary to calculate the Γ value, this model approximates an IPCE (543 nm) value of 12.76% . Lastly, Xu et al. reported synthesized ZnO nanowires with lengths ~17 μm, and radius of ~112.5 nm [79]. However, they did not report any nanowire density nor dye loading data or Γ value. They measured an IPCE (543 nm) value ~ 57 % for their N719-sensitized ZnO nanowire DSSC [79]. Using these values in the model, with the fixed parameters listed in Table 4.1 including the dye loading that is necessary to calculate the Γ value as well as a fixed density of $1.2x10^9/cm^2$, this model approximates an IPCE (543 nm) value of

62.56%. The differences in the model and the experimental results can be attributed to the model assumptions and factors neglected in the model that may not necessarily be the case for these experimental conditions (e.g., no losses due to absorption by the electrolyte, no nanowire overlap, uniform length and radius, etc.).

Model Limitations:

As mentioned earlier, the experimental measure of IPCE for DSSCs generally does not exceed 80%, this is due to the reflection losses as well as light absorbed by the electrolyte. This model does not account for these losses. Also, for a realistic steady-state electron concentration profile, a nonlinear dependence of the rate of recombination on the electron concentration in the ZnO film should be considered. This is to say that the contribution of dye molecules on the light harvest is not equal; the dye molecules on the bottom of the nanowires (near the TCO) absorb more light than those on the top of the nanowires since the light come from the TCO side of the solar cell. Refer to Figure 4.9 for an illustration of this concept. As the ZnO film thickness (nanowire length) increases to extremely large values, the light cannot reach the dyes molecules at the tip of nanowires (i.e., all light is absorbed by the dye molecules that are adsorbed closer to the bottom of the film). As a result, charge collection efficiency may be affected. In this case of extremely long nanowires, there will not be any photo-induced electrons at the top of nanowires if there is no light to be absorbed, so recombination rate is zero. On the other hand, near the bottom of the film, the dye molecules should absorb more light so the recombination rate may be higher there.

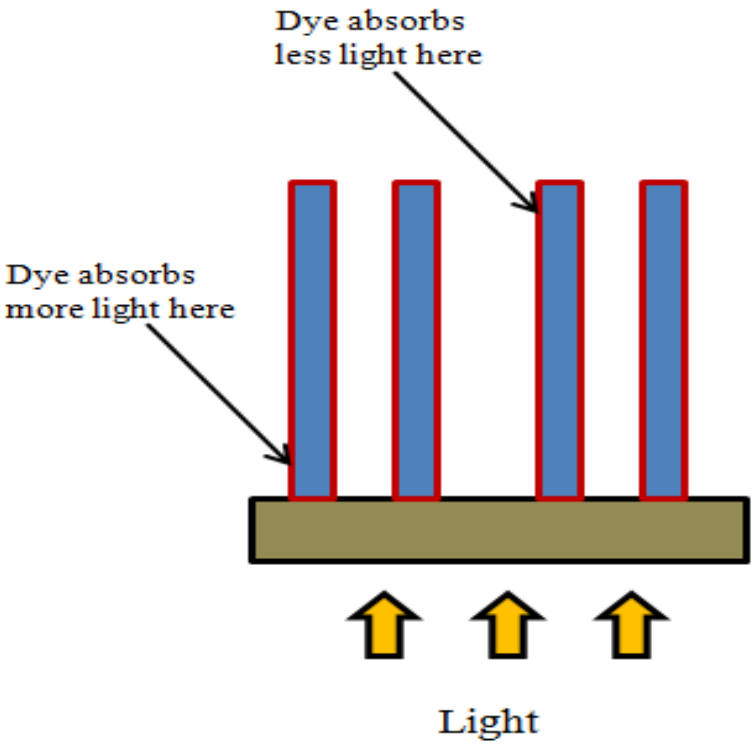

Figure 4.9 Schematic of dye molecules absorbing various degrees of light based on its distance from the light source.

There are other factors that influence the IPCE that are not accounted for in this model. For instance, the occurrence of short-circuiting of the DSSC due to electron back transfer is not included in the model but will affect the conversion efficiency of the DSSC. Specifically, the void space in between the ZnO nanowires allows for the direct contact between the oxidized species of the electrolyte and the electrons at the charge collecting substrate. This contact leads to charge shortage which will limit the DSSC performance. Also, the type of electrolyte used can affect the DSSC performance. Specifically, the higher viscosity of a gel electrolyte compared to a liquid electrolyte can reduce charge leakage and improve DSSC performance.

4.4 Brief Summary

This model allows one to see how the affects of geometry is coupled between both the LHE and APCE. So, it is important to understand how various combinations of the radius, length, and density affect the overall results of IPCE. This model allows you to approximate the optimal combination of the ZnO nanowire physical dimensions under specific constant parameters. The model revealed the important balance of having long enough nanowires that contribute to the needed high surface area for greater light absorption, but at the same time are not too long where the charge collection efficiency is negatively affected due to L<<<d. The model also allows one to investigate the effects of using materials with fewer trap sites, high electron diffusivity, and slower recombination times. Additionally, from the results of the model we are able to see that the properties of the dye (e.g., the extinction coefficient) play a crucial role in the surface area needed to absorb high levels of light. Utilizing dyes with high extinction coefficient allows greater light absorption, which is very advantageous for shorter nanowire lengths. But ultimately there has to be an optimal combination of the physical dimensions (i.e., surface area), dye loading, as well as recombination rate to yield both 100% LHE and 100% APCE to give the maximum obtainable IPCE. There are various combinations of the physical dimensions, dye loading, and recombination rate constants that can yield a maximum IPCE value. The model can be used to identify which specific conditions are needed to yield maximum IPCE values. For an example, using the fixed model parameters (i.e., dye loading of 2.25 $x10^{-10}/cm^2$ ZnO surface, recombination rate constant of 1000 s^{-1}, m value of 0.7, and a D_{cb} of 0.1 cm^2/s), nanowire arrays with a nanowire radius of 50 nm, nanowire length of 20 μm, and density of 1.45 $x10^{10}$ $/cm^2$ of projected surface area (where surface coverage is ~95%, surface area is ~870 cm^2, and the absorption coefficient is ~1375 cm^{-1}), the IPCE(543nm) is ~100% for a N719 sensitized ZnO

nanowire DSSC. Other ideal conditions can yield maximum IPCE values. Moreover, lower dye loadings and faster recombination rates would require greater surfaces areas to yield maximum IPCE results, and vice versa.

CHAPTER 5

ZINC OXIDE NANOWIRE DYE-SENSITIZED SOLAR CELL DESIGNS FOR ENHANCED PERFORMANCE

5.1 Block Layer Zinc Oxide Nanowire Dye-Sensitized Solar Cell Design

5.1.1 Introduction

There are several critical issues for nanowire-based DSSCs containing liquid electrolytes that need to be addressed and solved. One critical issue that many researchers in this field have paid close attention to is the loss of power conversion efficiency due to electron back transfer at the anode of the cell. When the redox system regenerates the oxidized dye molecule, it in return wants to be regenerated. Ideally, the oxidized species of the redox electrolyte system should be regenerated at the counter electrode by electrons passed through the load, as seen in Figure 5.1. Furthermore, there should only be unidirectional flow for electrons to travel from the anode to the cathode.

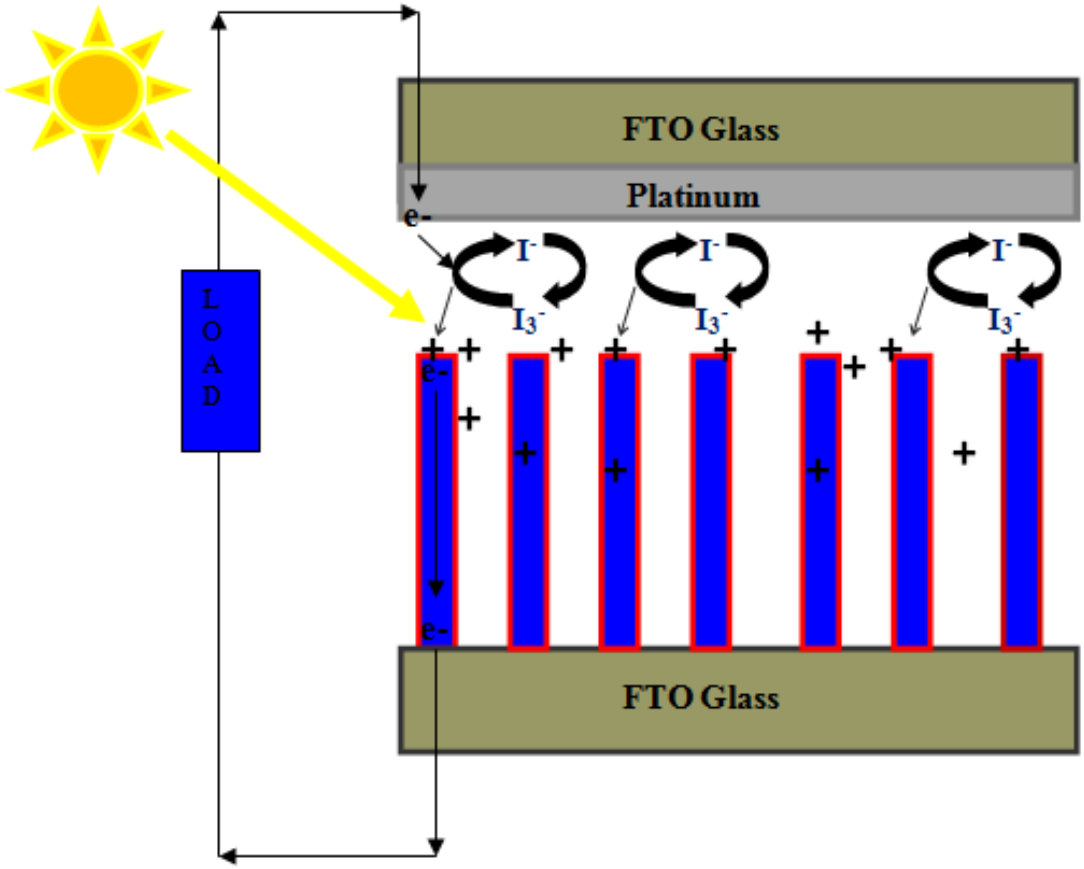

Figure 5.1 Schematic of ideal process in traditional DSSCs based on 1D ZnO nanowires.

However, that ideal situation does not occur due to the fact the oxidized species of the redox system electrolyte want to regenerate itself by taking the electrons that are at the anode; this critical problem is highlighted in Figure 5.2 below. Specifically, the spaces or holes between the NWs allow direct contact between the oxidized species of the electrolyte and the electrons on the conductive glass substrate. This problem is commonly referred to as back transfer of electrons from the conductive glass layer to the oxidized species in the electrolyte. Electron back transfer prevents unidirectional flow and this undesired occurrence leads to short-circuiting of the cell, which undoubtedly reduces the overall power conversion efficiency.

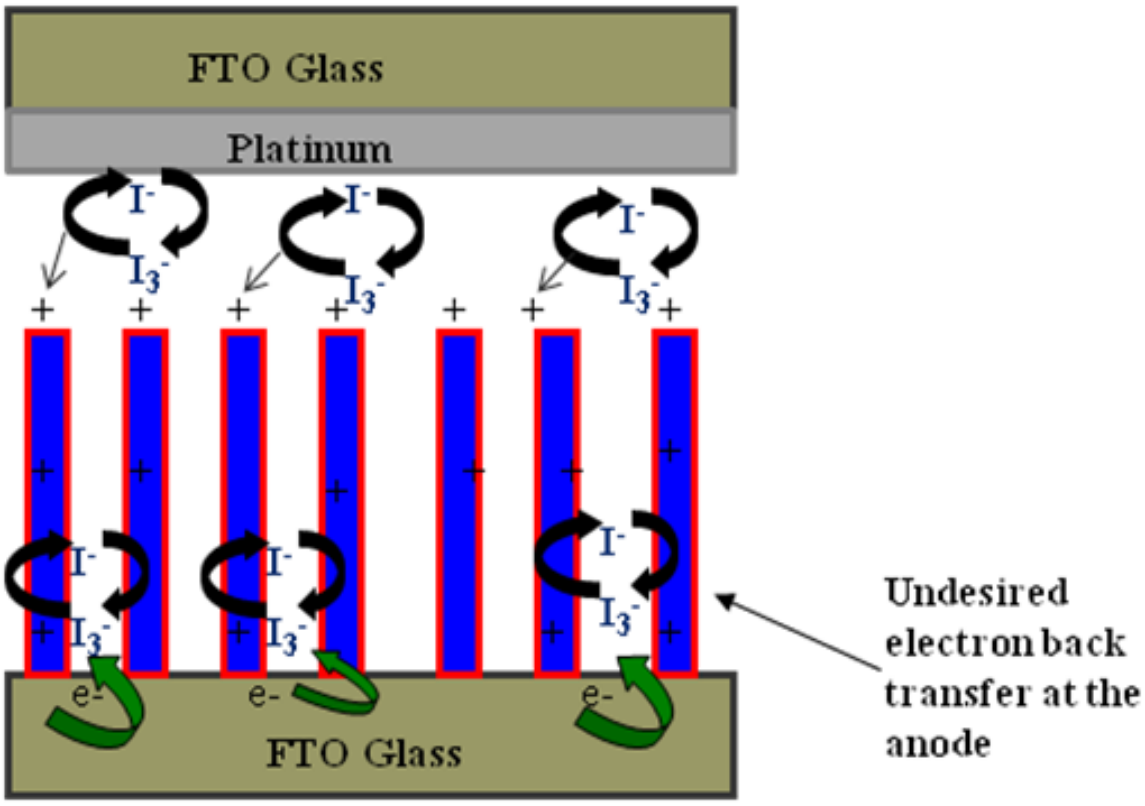

Figure 5.2 Illustration demonstrating the major drawback of a traditional DSSC based on 1D ZnO nanowires.

It is expected that a carefully designed blocking layer will control the issue of electron back transfer, as seen in Figure 5.3. By placing a layer on the FTO surface that acts as a barrier separating the oxidized species of the electrolyte from the electrons at the anode, the unidirectional electron flow from the negative electrode to the positive electrode is maintained and short-circuiting of the DSSC can be avoided.

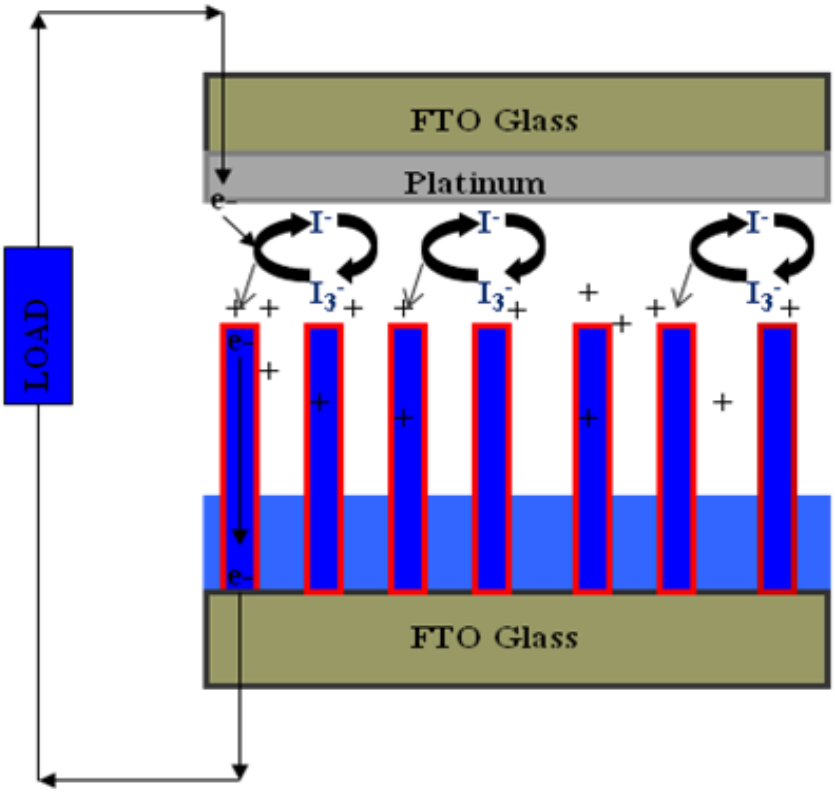

Figure 5.3 Schematic demonstrating the use of a block layer as a solution to minimize electron back transfer in the traditional DSSC based on 1D ZnO nanowires.

In this study, polymer layers and TiO_2 layers are considered to be excellent blocking agents to minimize electron recombination. There are various routes to applying a polymer film as a block layer on specific substrates. Here, we focus on a very unique method that is based on previous work done in our laboratory by Xihong Zu. Specifically, Zu's work demonstrates a novel technique for fabricating ordered nanoring arrays of inorganic materials [135]. Essentially the P4VP shrinks to the extent of being barely on the surface leaving behind ordered nanorings or holes that expose the substrate surface. Therefore, it can be inferred that only the PS polymer remains on the surface as seen in Figure 5.4. Specifically, when the diblock copolymer thin film

underwent methanol vapor treatment, the P4VP blocks contracted and moved to the interfacial region between the two blocks, which resulted in the configuration shown in the AFM images [135]. The AFM and SEM images of the PS-b-P4VP films are provided in Figure 5.5. "From the SEM image, the average center-to-center distance of the ZnO nanorings was found to be 93 ±2 nm, and the inner and outer diameters of the nanorings were around 31 ± 4 nm and 45 ± 3 nm, respectively [135]."

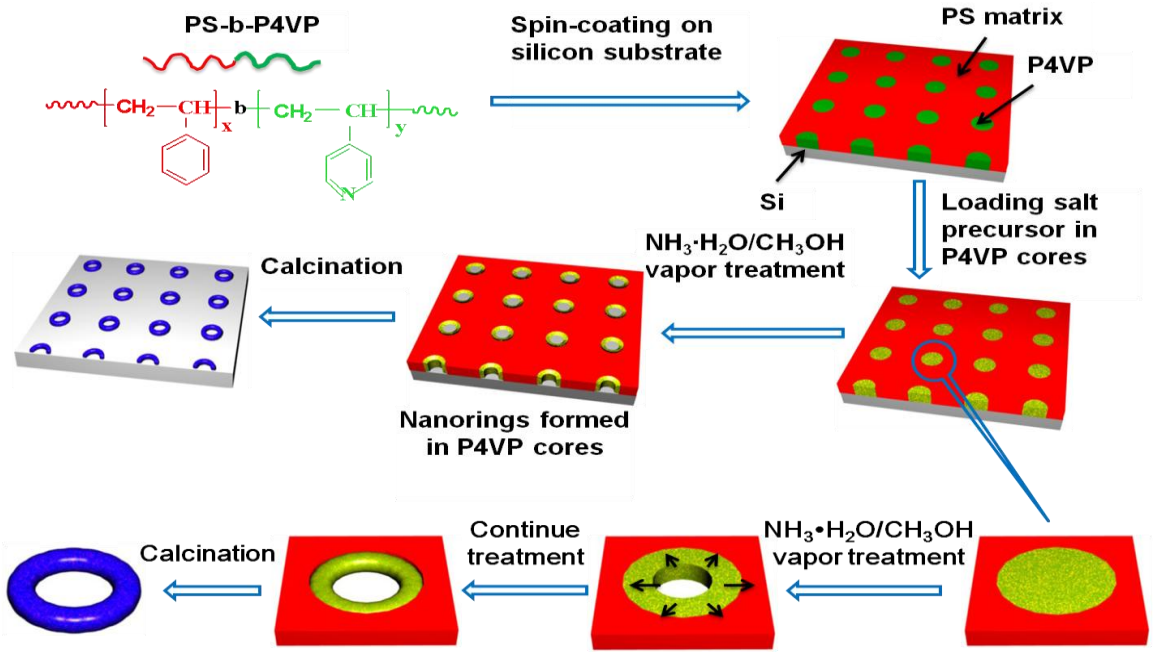

Figure 5.4 Schematic illustration of the nanoring array fabrication using a PS-b-P4VP block copolymer thin film as a template [135].

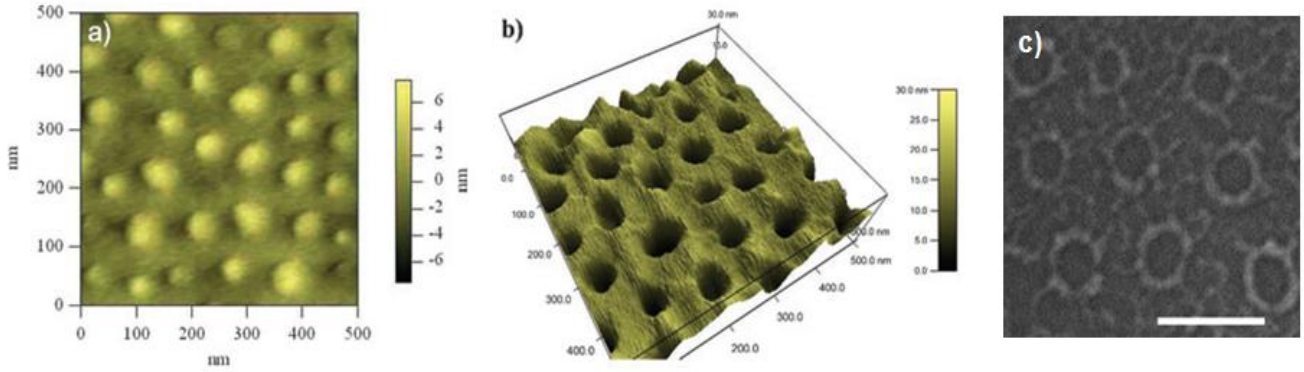

Figure 5.5 (Left) AFM image of the PS-b-P4VP film before methanol vapor treatment; (Middle) 3D AFM image of the PS-b-P4VP film exposed to the vapor of methanol at 40°C for 2h (500 nm x 500 nm); (Right) SEM image of ZnO nanoring arrays by using PS-b-P4VP block copolymer thin film as a template (scale bar = 100 nm) [135].

In this study, we will apply a single polymer block layer on the seeded glass surface by removal of one polymer block of a diblock copolymer through methanol vapor treatment film. The removal of the polymer block will leave holes in the film that provide direct exposure to the seed layer underneath the polymer film. From these seed layer sites, the ZnO nanowire will grow and there will still remain a polymer film between the glass surface and the nanowire array. Additionally, we will apply a TiO_2 block layer via spray pyrolysis of a titanium based solution onto the glass surface, followed by annealing at a high temperature. Lastly, a hybrid block layer of TiO_2 and P4VP polymer will be applied to the glass surface via spray pyrolysis. The polymer mixture is added to the titanium solution to form this hybrid film.

5.1.2 Experimental Procedure

Preparation of Polymer Block Layer

Before the polymer layer is applied, the seed layer must be coated onto the FTO substrate. Therefore, a 5mM ethanolic solution of zinc acetate dihydrate was spin coated onto the clean FTO surface and annealed at 400°C. The diblock copolymer was dissolved in chloroform, as it is a good solvent for both polymer components. Specifically, a 0.5 wt% solution of PS-b-P4VP was prepared and spin coated onto the seeded FTO substrate at 3000 rpm. The polymer molecules then self-assembled into ordered P4VP nanodomains surrounded by a PS matrix. This thin film was then exposed to methanol vapor at 40°C for 2 h and then dried. The P4VP blocks were then shrank and moved to the interfacial region between the PS matrix and the P4VP core. Since the P4VP was essentially etched away due to vapor treatment, only the PS matrix remained on the substrate. Moreover, at the original sites of the P4VP polymer, there were holes that directly exposed the seed layer that was used as seeds to grow the ZnO NWs in the same manner as described in Section 3.2. Figure 5.6 illustrates the experimental scheme to yield the polymer block layer based on the PS-b- P4VP diblock copolymer.

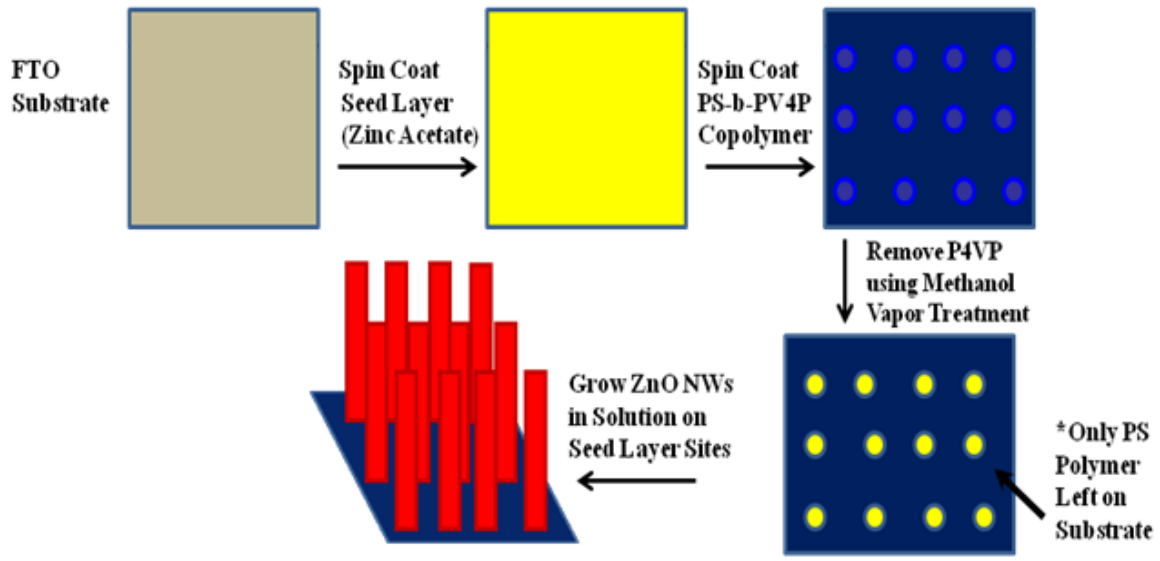

Figure 5.6 Schematic illustration of the experimental process of applying the polymer block layer based on the PS-b-P4VP diblock copolymer.

Preparation of TiO_2 Block Layer

The TiO_2 was prepared from di-iso-propoxy titanium bis(acetylacetonate) (TAA) and its block layer was applied to clean FTO substrates via a spray pyrolysis method [136]. The substrate was placed on a hot plate whose temperature was kept at 400-450°C, and an ethanolic solution of 1M TAA was sprayed layer by layer from a distance of roughly 20 cm onto the hot substrate. Specifically, one spray corresponded to about one-tenth of one layer, and one layer corresponded to approximately 5 mL of the solution. There was a 30-45 second pause between every 5 sprays to ensure complete pyrolysis of the previous layer and to restore the original substrate temperature. Once the appropriate number of layers was applied, the coated substrate was then annealed further at 500°C for 1h in the air. A schematic of the homemade apparatus for the spray pyrolysis technique is shown in Figure 5.7.

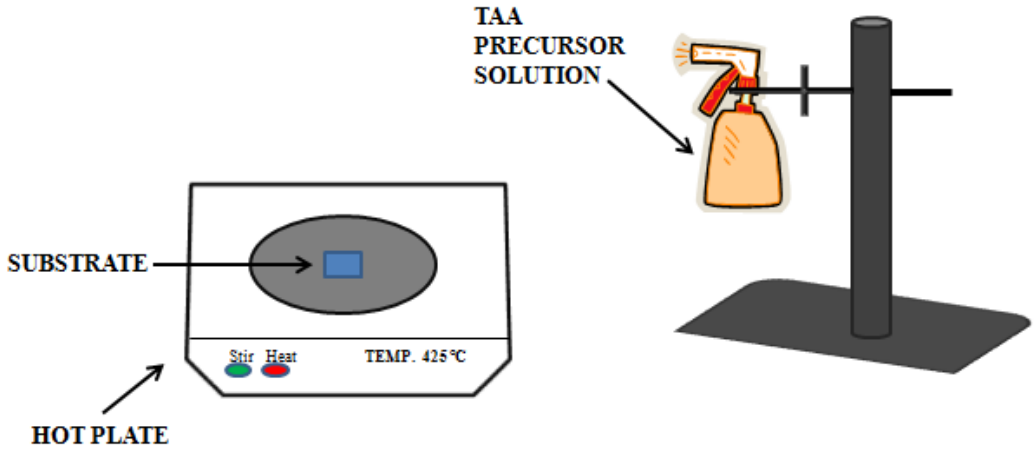

Figure 5.7 Schematic of homemade apparatus for the spray pyrolysis of TAA to form TiO_2 block layer.

Fabrication of ZnO Nanowires on TiO_2 Block Layer

Formation of the seed layer on the block layer coated FTO was conducted by spin-coating a 10 mM ethanolic solution of zinc acetate dihydrate. SEM analysis showed that at least 10 spin coating cycles were needed for a dense seed layer since the FTO substrate was covered with crystalline TiO_2 as the block layer. The dense seed layer was annealed at 400°C to form the ZnO nanocrystalline layer, and this seed application process was repeated to ensure uniform coverage of the seed layer. The seeded substrates were then fastened to the top of the chemical solution in a capped vessel. ZnO NWs were grown from the seed layer using a chemical bath deposition method in a 25 mM equimolar aqueous solution of zinc nitrate 6-hydrate and HMTA at 90°C for 5 h. Substrates were subsequently rinsed with deionized water and ethanol and oven dried at 95° C for 1h in air.

DSSC Assembly

The substrate was immersed in a 0.5 mM ethanolic solution of a Ruthenium-based dye for 1 h. This dye is chemically named (cis-bis (isothiocyanato) bis (2,2'-bipyridyl-4,4'-dicarboxylato)-ruthenium (II) bis-tetrabutylammonium and is commercially known as N719 dye from Solaronix. The counterelectrode was a platinum coated FTO glass plate (1x1 cm^2-same type of FTO used as the substrate for nanowire growth). The Pt was brush-coated onto the FTO using a 5 mM solution of H_2PtCl_6 in 2-propanol and annealed in oven at 350-400° C for 1 h. The Pt electrode could also be prepared by sputter coating the Pt target onto FTO glass. The iodide-triiodide-based electrolyte solution, consisting of 0.5 M LiI, 0.05 M I_2, and 0.5 M 4-tertbutylpyridine in 3-methoxypropionitrile, was placed on the active electrode area drop-wise.

The average active electrode area was around 0.3 cm^2. The electrodes were separated by a 60-μm thermoplast hot-melt sealing foil (Surlyn by Solaronix) and sandwiched together with clips. A small space of bare FTO glass was uncovered for wire connection on the anode. The configuration of the solar cell was achieved by putting the ZnO nanowire face of the FTO substrate on the top of the counterelectrode in face-to-face fashion. A DS345 30 MHz (Stanford Research Systems) and a 4200- SCS (Semiconductor characterization system, Keithley Instruments Inc.) were used to examine the *I-V* curves under AM 1.5-type simulated sunlight. For all data, the corresponding illumination was 100 mW/cm^2. Pictures of an assembled solar cell, the characterization systems, and system apparatus are shown in Figure 5.8.

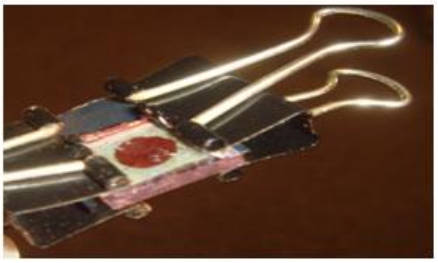

Actual DSSC

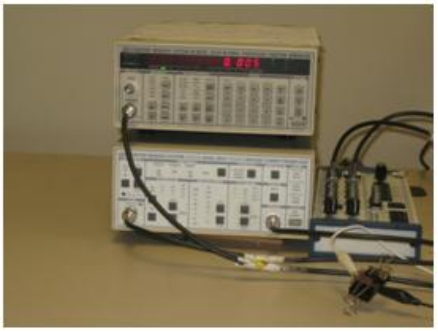

DS345 30 MHz Function Generator

SR570 Current Preamplifier

(Stanford Research Systems)

SoLux ® Solar Simulator
Simulated Sunlight, AM 1.5
P_{in}= 100 mW/cm^2

Figure 5.8 (Top) Solar Cell; (Middle) Characterization System; (Bottom) Experimental Apparatus with SoLux Solar Simulator.

5.1.3 Experimental Results and Characterization

Before showing the results of the power conversion efficiency for an enhanced ZnO NW based DSSC due to incorporation of a block layer, it is important to know that the experimental results show that the average efficiency of a basic unmodified 1D ZnO NW based DSSC is 0.01% (see Figure 5.9). The DSSC data along with the physical dimensions of the synthesized ZnO NWs are shown below in Table 5.1.

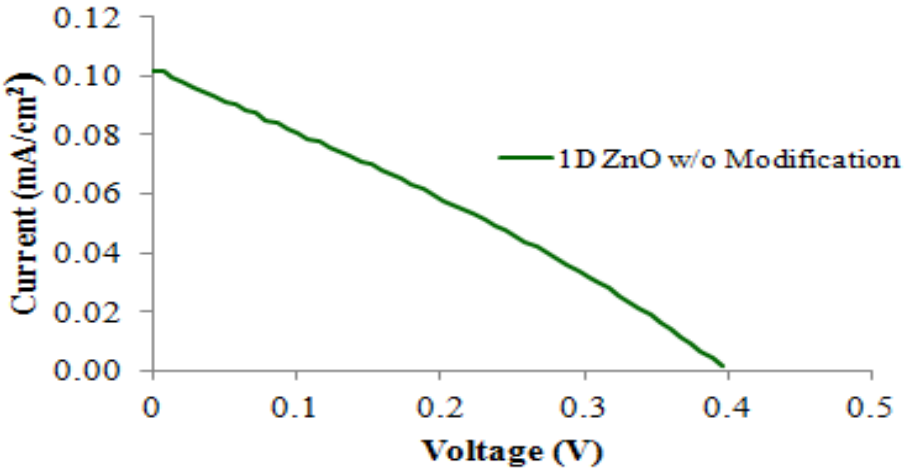

Figure 5.9 J-V curve of DSSC based on an unmodified assembly of 1D ZnO NW array using 25 mM equimolar concentrations of Zinc Nitrate Hexahydrate and HMTA.

Table 5.1 Physical Characteristics of ZnO NW used in DSSC and its Photovoltaic Characteristics.

Density, N (per cm^2)	1.35×10^9
Length, L (μm)	2.1 ± 0.6
Diameter, D (nm)	105 ± 20
Concentration (mM)	25
V_{oc} (V)	0.40
J_{sc} (mA/cm^2)	0.10
FF	0.30
Efficiency (%)	0.01 ± 0.006

For the case of incorporating the polymer block layer based on the technique to form a patterned diblock copolymer film, it was very difficult to determine whether the ZnO nanowires were growing from the holes exposing the seed layer sites. From the SEM image in Figure 5.10 below, it is clear that a very dense layer of the ZnO nanowire array is fabricated. However, the density of the array is so high and the diameter of the holes are very small, therefore it cannot be concluded if the nanowires only grow at the specific hole sites. It was found that the desired surface of the diblock copolymer patterned structure was very difficult to control, and in order to get a suitable SEM image that captures the fundamental idea of this technique (growing the nanowires from the holes of the polymer surface) a very smooth surface was needed. For this purpose, it was decided not to pursue further modifications of this technique. Despite not having clear evidence of the nanowires growing from the seed layer sites (holes of polymer film), the efficiency of the DSSC incorporating the PS polymer layer still gave an improved average efficiency of 0.18 %. It is believed that this improvement is due to the polymer barrier that aids in reducing the contact of opposite charges at the FTO-electrolyte interface.

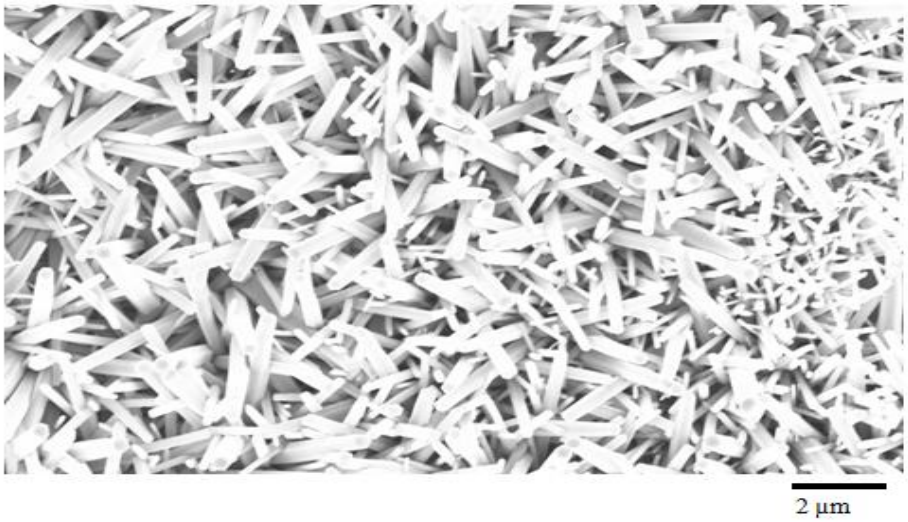

Figure 5.10 SEM image of ZnO nanowires grown from on seed layer sites with the PS polymer block layer.

The next type of block layer studied was TiO_2. The main challenge that was faced during this study was how to control the excessive amount of cracking in the TiO_2 BL. Evidence of the critical cracking issue can be seen in Figure 5.11. Using a small representative portion of the entire TiO_2 BL surface, we were able to estimate a total TiO_2 BL coverage of approximately 70%.

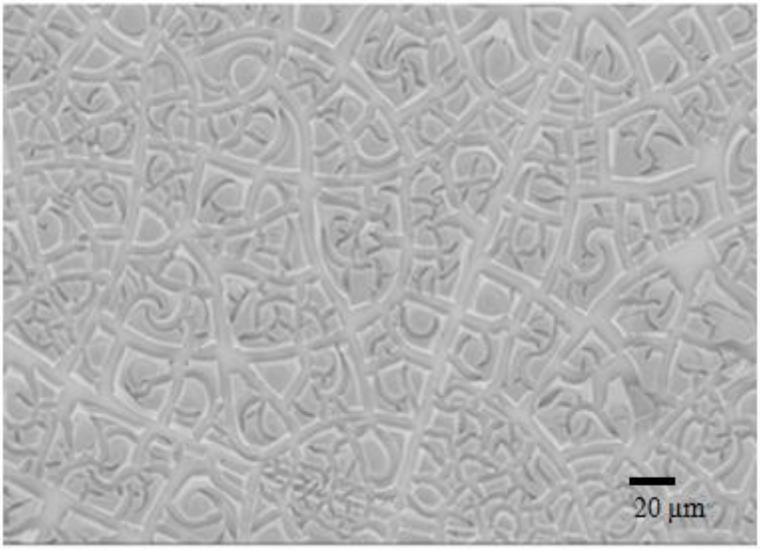

Figure 5.11 SEM image of TiO_2 BL.

Despite a complete coverage of the TiO_2 BL, syntheses of the ZnO NWs onto the surface of the block layer were still pursued. From Figure 5.12, it is clear that the ZnO NWs grow on both the FTO glass surface and the TiO_2 BL surface. From SEM analysis, we were able to calculate the nanowire density on the block layer and the FTO glass (N_{BL} and N_{FTO}, respectively), as well as the length and diameter of the ZnO NWs on the block layer and the FTO glass (L_{BL} and L_{FTO}, respectively; D_{BL} and D_{FTO}, respectively). The results confirmed that the density of the ZnO NW array grown on the block layer was higher than those grown simply on the FTO glass; the N_{BL} = 3.53 x $10^9/cm^2$, while the N_{FTO} = 8.80 x $10^8/cm^2$. The higher density along the block layer is probably due to the seed layer being thicker in those areas. Smaller diameters tend to occur when the seed layer is thicker, and these results show that the D_{BL}= 91 nm, while the D_{FTO} = 133 nm. Furthermore, it is very typical to see higher density arrays when the nanowires are much smaller in diameter. The length, however, did not vary too much as the L_{BL} = 2.2 μm, while the L_{FTO} = 2.4 μm. Generally, the amount of seed layer does not have a significant effect on nanowire length.

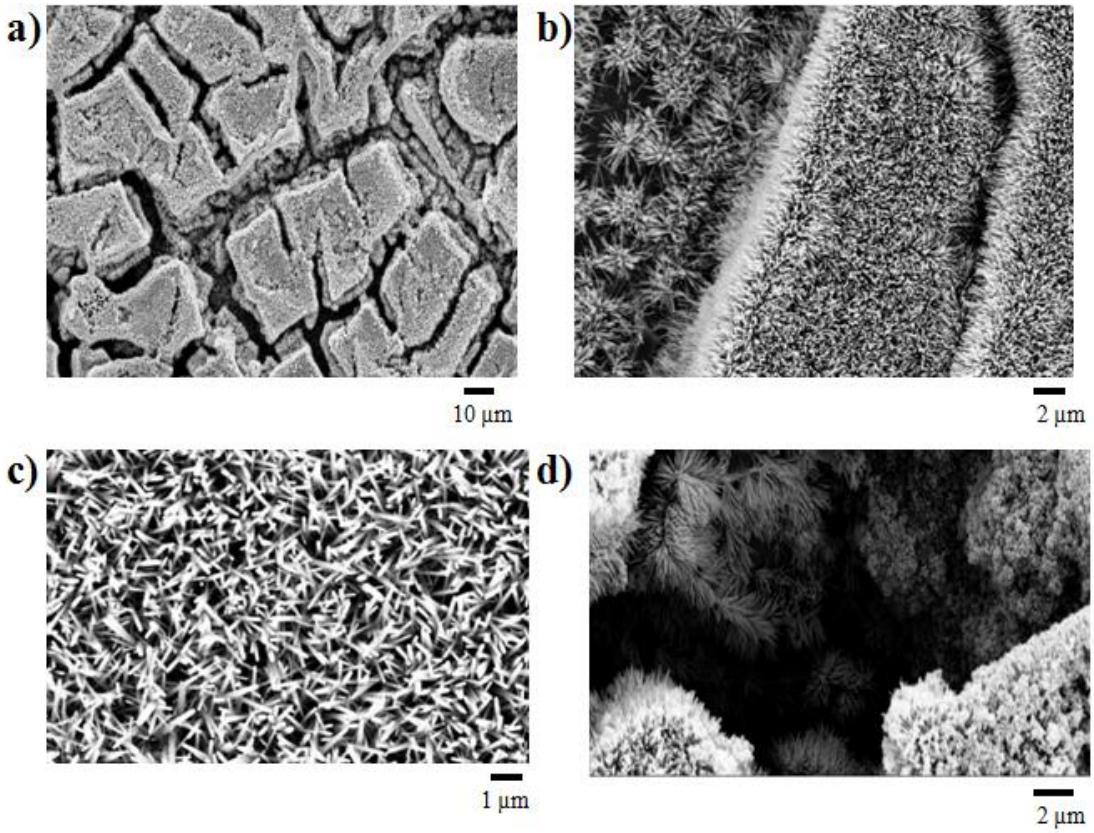

Figure 5.12 SEM images of ZnO NWs grown on TiO_2 BL coated FTO substrates. a) zoomed out image; b) zoomed in image; c) zoomed in image of NWs on BL surface; d) zoomed in image of NWs on FTO surface.

Although there was a concern with the amount of cracking in the block layer, the DSSC with the TiO_2 BL was able to show promising performance with an average efficiency of 0.29%. Interestingly, the polymer layer did not have any issues with cracking, but the conversion efficiencies for DSSCs incorporating the polymer BL were still not as high as those incorporating the TiO_2 BL. Polymers are known to have a much higher elasticity than crystalline materials, which allows a more uniform and flexible surface. Therefore, it was believed that by adding a flexible polymer to its precursor solution, the inorganic TiO_2 layer would be held together during annealing. This would reduce the amount of cracking in the TiO_2 block layer and would significantly reduce electron back transfer and yield better DSSC performance. Therefore,

P4VP polymer (10.0 wt. %) was mixed into the TAA solution and applied to the FTO substrate via spray pyrolysis to create a uniform film on the glass surface. The combination of TiO_2 and P4VP BL allowed an average efficiency of 0.43 %, the highest of all the cases in the block layer study. The addition of the polymer to the TiO_2 eliminated the limitations of using a non-uniform block layer, allowing for an ideal barrier to prevent contact between the electrons at the anode and the oxidize electrolyte species. Figure 5.13 and Table 5.2 provide the photovoltaic characteristics of the DSSCs based on ZnO NWs with various block layers. Specifically in Table 5.2, we see higher V_{oc} values for these DSSCs with block layers compared to the V_{oc} value given in Table 5.1 for DSSCs without block layers. The increase in V_{oc} is a critical reflection of the reduction of electron back transfer. V_{oc} is known to be strongly dependent on the charge recombination reactions taking place at the substrate-electrolyte interface; thus, a larger V_{oc} value indicates the suppression of those reactions with the block layer.

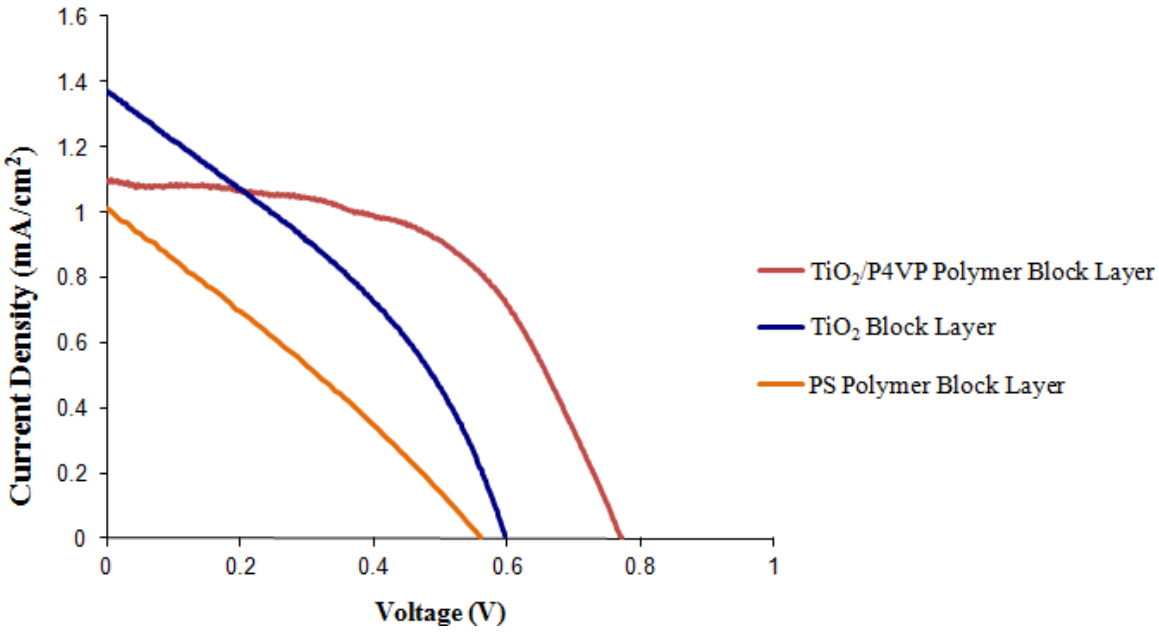

Figure 5.13 J-V curves of DSSCs based on 1D ZnO NW arrays incorporating block layers. (Pink) TiO_2/P4VP BL; (Blue) TiO_2 BL; (Orange) PS Polymer BL.

Table 5.2 Photovoltaic Characteristics of ZnO NW based DSSCs incorporating Block Layers.

Block Layer Type	Concentration (mM)	V_{oc} (V)	Jsc (mA/cm^2)	FF	Efficiency (%)
PS Polymer	25	0.562	1.01	0.317	0.18 ± 0.02
TiO_2	25	0.597	1.37	0.358	0.29 ± 0.03
TiO_2/P4VP Polymer	25	0.759	1.10	0.521	0.43 ± 0.06

5.1.4 Brief Summary

The purpose of the block layer was to reduce, if not eliminate, the occurrence of electron back transfer at the anode. Because there are spaces in between the ZnO nanowires, direct access is provided for the oxidized species of the electrolyte to join with the electrons at the conducting glass substrate. This leads to short-circuiting of the cell, which ultimately reduces the V_{oc}. In this study, we investigated the use of different types of block layers. The results revealed that in all cases, the Voc was increased from that of the base case with no block layer; and ultimately, the average efficiency was increased when the block layers were incorporated into the DSSC. The idea to add the polymer to the TiO_2 mixture was so that the more elastic polymer would allow the rigid TiO_2 BL to become more flexible, which in turn would reduce the risk of the crystalline layer hardening under temperature and cracking. The incorporation of the hybrid TiO_2/P4VP block layer resulted in the highest V_{oc} value of 0.759 and the highest average efficiency value of 0.43%, which was an increase of more than 40 times the efficiency of the ZnO nanowire based DSSC without a block layer.

5.2 Three-Dimensional Zinc Oxide Nanowire Dye-Sensitized Solar Cell Designs

5.2.1 Introduction

There have also been many studies done on how to improve the aspect ratio of ZnO NWs. In particularly, researchers are trying to greatly enhance the length of the nanowires since it has shown in several studies that DSSCs with longer ZnO NWs yield higher conversion efficiencies. Xu et al. report a technique based on a liquid-phase chemical process that allows growth of very long ZnO NWs (up to 33 μm) solely on the seeded substrate, preventing the formation of ZnO in the bulk solution [79]. These ultralong ZnO NWs were used as the photoanode for DSSC applications. The performance results of their DSSC experiments revealed that the power conversion efficiency increased with increasing ZnO nanowire length. The DSSC with the greatest nanowire length of 33 μm had an overall efficiency of 2.1% [79].

It is well known in this field of study that the more surface area that is created by the semiconducting nanomaterial of the DSSC, the more light can be absorbed. Therefore, the main universal goal is to increase the surface area of the semiconducting nanomaterial. Many researchers have equated increasing the surface area with increasing the nanowire length as reported previously. Despite the reporting of these ultralong nanowires, there still has been great difficulty in synthesizing nanowires longer than 10 μm. Therefore, in this research, we propose a way to increase the surface area and density of the ZnO NWs by designing DSSCs that would be based on a three-dimensional structure of ZnO NWs. Figure 5.14 illustrates how we propose to transform a 1D ZnO NW array into a 3D ZnO NW array.

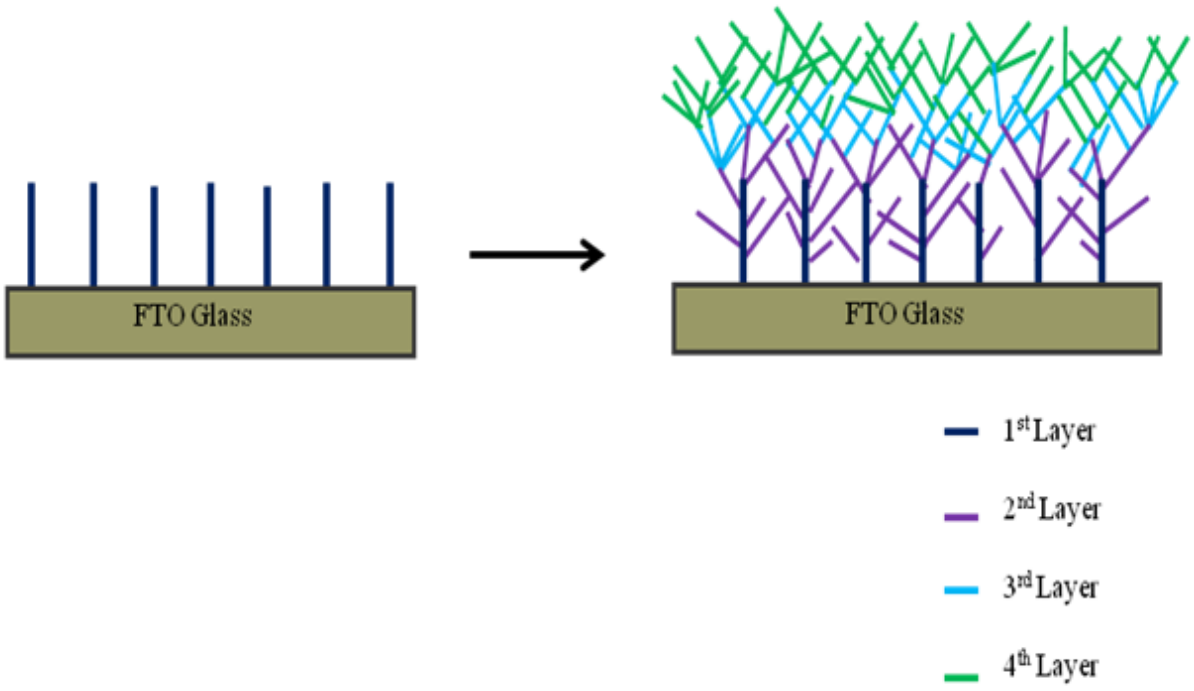

Figure 5.14 Illustration displaying the transforming of a 1D ZnO NW array to a 3D ZnO NW array.

This idea stemmed from a previous report by Sun et al., in which a direct integration of a Si NW core and ZnO NW branches is fabricated via a metal-assisted chemical etching process (Si NWs) and hydrothermal growth method (ZnO NW) [137]. The ultimate 3D nanoheterostructure, as seen in Figure 5.15, was used as a photodetector device. They report an overall conversion efficiency of 0.154 % [137].

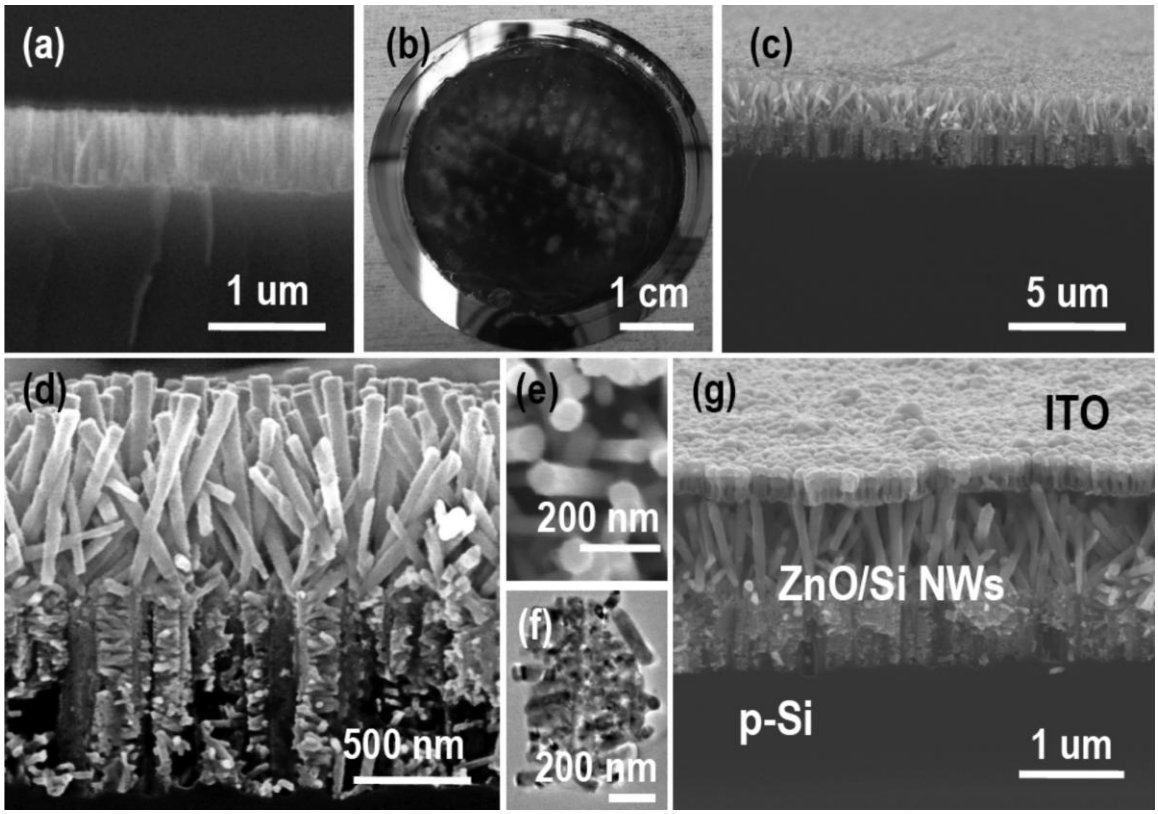

Figure 5.15 (a) Cross-sectional SEM image and (b) optical image of NW arrays on a 2 in. p-type Si wafer (etched for 5 min). (c) 45° view SEM micrographs of the ZnO/Si branched nanowire heterostructures at low magnification. (d) 89° view and (e) top view SEM micrographs of the ZnO/ Si branched nanowire heterostructures at high magnification. (f) LR-TEM image on a single Si/ZnO branched NW. (g) 45° view SEM image of a photodetector device with top ITO contact [137].

In this work, however, we propose to fabricate flower-like ZnO NWs based on a simple layer by layer (LBL) hydrothermal process. As seen in Figure 5.16, there are 1D secondary ZnO NWs that branch out in multiple directions from the tips of the primary 1D NWs by reapplying the seed layer and placing the sample into fresh precursor solution. This design still allows for a direct conduction pathway while achieving a higher dye adsorption due to the greater surface area and increased nanowire density that will improve the overall power conversion efficiency of the DSSC.

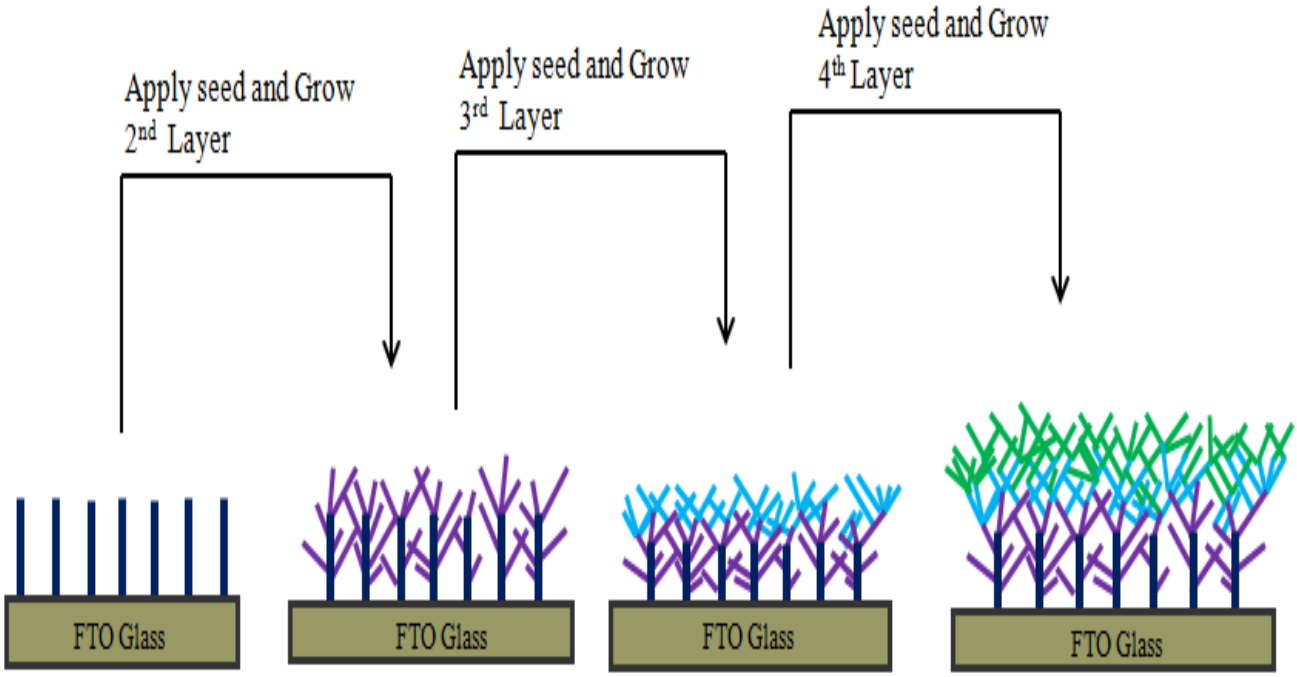

Figure 5.16 Schematic LBL growth procedure of 1D ZnO NWs into 3D ZnO NWs.

5.2.2 Experimental Procedure

Fabrication of ZnO Nanowires

ZnO NWs were synthesized using a hydrothermal chemical solution based method. High-density ZnO NWs were grown on 1x1 cm^2 seeded fluorine-doped tin oxide (FTO) substrates via the following steps. Formation of the seed layer on FTO was conducted by spin-coating a 10 mM ethanolic solution of zinc acetate dihydrate. SEM analysis showed that at least 6 spin coating cycles were needed for a dense seed layer on the FTO substrate. The dense seed layer was annealed at 400°C to form the ZnO nanocrystalline layer, and this seed application process was repeated to ensure uniform coverage of the seed layer. The seeded substrates were then fastened to the top of the chemical solution in a capped vessel. ZnO NWs were grown from the seed layer using a chemical bath deposition method in a 25 mM or 50 mM equimolar aqueous solution of zinc nitrate 6-hydrate and HMTA and 10 mM Polyethylenimine (PEI) (end capped, MW 800 (LS), Aldrich) at 90°C for 2.5 h. The PEI served as an agent to help increase the length of the nanowires.

The samples were then placed in another fresh growth solution (25 mM or 50 mM equimolar aqueous solution of zinc nitrate 6-hydrate and HMTA) for another 2.5 hrs at 90°C. Substrates were subsequently rinsed with deionized water and ethanol and oven dried at 95° C for 30 min in air. This provided one layer of the ZnO nanowire array. To obtain subsequent layers, the same method was carried out for each layer: 1) the seed application onto the FTO substrate via spin coating; and 2) ZnO NW growth from that seed layer. As-grown ZnO NWs could be annealed further in air at 400°C for 30 min to improve the crystallinity of the NWs and the interfacial structures.

DSSC Assembly

The DSSC assembly and solar cell characterization process were performed in the same manner that was explained in Section 5.1.2.

5.2.3 Experimental Results and Characterization

The first experiment was conducted using the ZnO NW prepared from the growth solution containing 25 mM equimolar aqueous solution of zinc nitrate hexahydrate and HMTA. Figure 5.17 provides SEM images of various ZnO NW arrays exhibiting 3D flowerlike shapes. These are based on an equimolar starting precursor solution concentration of 25 mM. From these top view images, it appears that as the number of layers increases, the overall density of the ZnO NWs increases. During this experimentation, it was observed that as more layers were included in the DSSC device, the short circuit current density of the cell increased. Figure 5.18 and Table 5.3 provide data for the photovoltaic performance of these 3D ZnO NW based DSSCs.

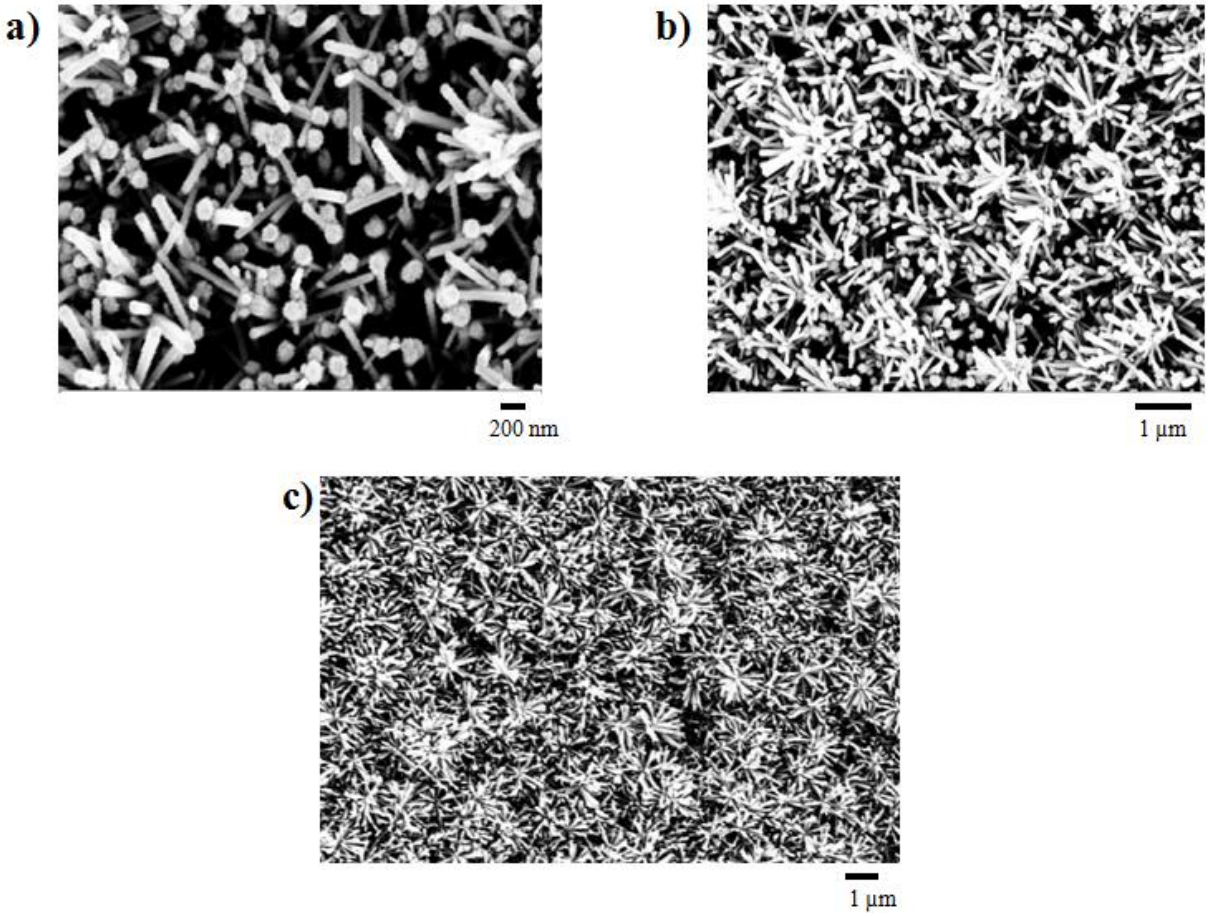

Figure 5.17 SEM images of 3D ZnO NW arrays. a) 2 layers; b) 3 layers; c) 4 layers.

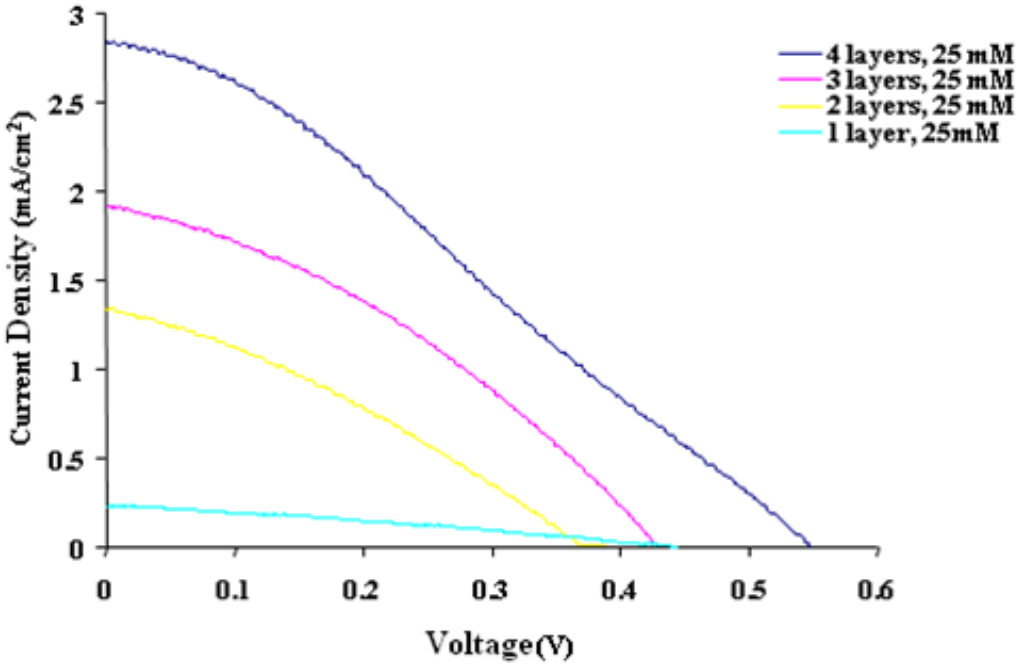

Figure 5.18 J-V curves of devices prepared with different numbers of ZnO nanowire array layers using 25 mM equimolar concentrations of Zinc Nitrate Hexahydrate and HMTA.

Table 5.3 Photovoltaic Characteristics of DSSCs based on layers of flower-like ZnO NW arrays.

Number of Layers	V_{oc} (V)	J_{sc} (mA/cm²)	FF	Efficiency (%)
4	**0.549**	**2.84**	**0.285**	**0.45 ± 0.06**
3	0.430	1.92	0.351	0.29 ± 0.02
2	0.389	1.34	0.303	0.16 ± 0.03
1	0.444	0.239	0.300	0.03 ± 0.02

Looking at Figure 5.19, a clear trend exists in that as the number of layers increases, the overall power conversion efficiency increases. With four layers of ZnO NW arrays grown using this method, an average efficiency of 0.45% was obtained. The increase in efficiency is expected for devices with more layers since it is known that the short circuit current density of photovoltaics is directly proportional to the overall efficiency.

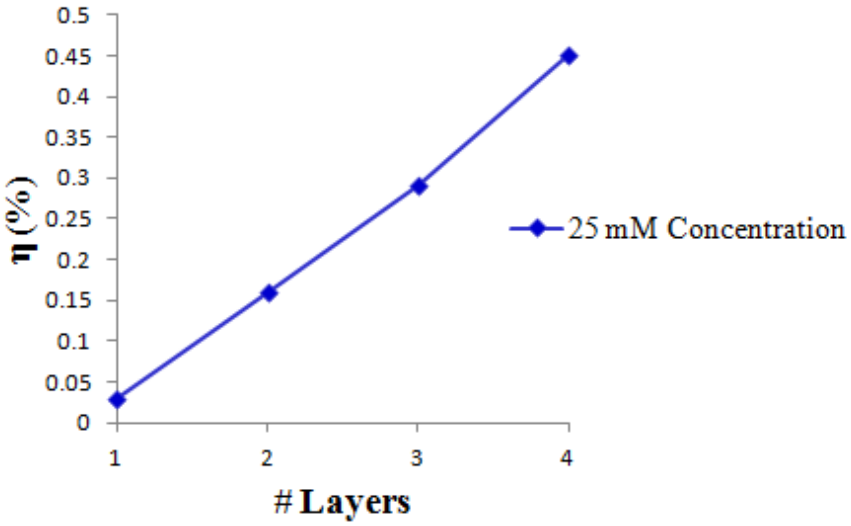

Figure 5.19 Dependence of overall power conversion efficiency with different numbers of ZnO nanowire array layers using 25 mM equimolar concentrations of Zinc Nitrate Hexahydrate and HMTA.

It is believed that an increase in precursor concentration leads to a higher density of ZnO NWs. A higher density of nanowires, in turn, typically results in an improved dye loading and better light absorption which significantly enhances the conversion efficiency of the DSSC. Thus, the purpose of the following experiment was to determine if the DSSC efficiency is influenced by the concentration of the precursor growth solution. We decided to base this study on a constant number of layers of ZnO NW arrays. Therefore, two groups of DSSCs based on 5 layers of ZnO nanowire arrays were compared to study the effect of precursor concentration on DSSC performance. The first group of devices was based on 5 layers of the ZnO NW array and

was prepared as before using 25 mM equimolar aqueous solution zinc nitrate hexahydrate and HMTA, and 5 mM PEI. The other DSSCs were also based on 5 layers of the ZnO NW array but were prepared based on twice as much concentration of the precursor solution using a 50 mM equimolar aqueous solution of zinc nitrate hexahydrate and HMTA, and 10 mM PEI. Figure 5.20 shows the SEM images of these two types of five-layered ZnO NW arrays. Figure 5.21 clearly shows that the higher concentration of starting materials produced a larger short circuit current density (J_{sc}). As expected, the data clearly showed that the higher concentration of reacting materials allowed for a higher overall power conversion efficiency. While it can be very difficult to measure and compare actual nanowire density, we believe that the increase in J_{sc} and overall efficiency was due to the increased nanowire density caused by a higher precursor concentration. The full photovoltaic characteristics of these DSSCs are provided in Table 5.4. With five layers of ZnO NW arrays grown using this method, an average efficiency of 0.72% was obtained in the case of 25 mM precursor solution concentration, and a 1.51% average efficiency was obtained in the case of 50 mM precursor solution concentration.

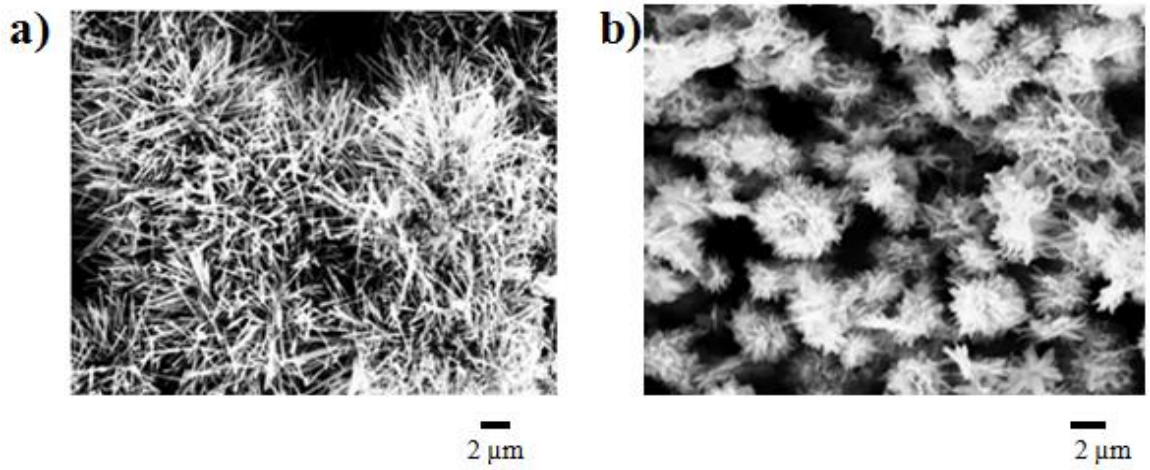

Figure 5.20 SEM images of 5 layered ZnO NW arrays. a) 25 mM equimolar precursor solution concentration; b) 50 mM equimolar precursor solution concentration.

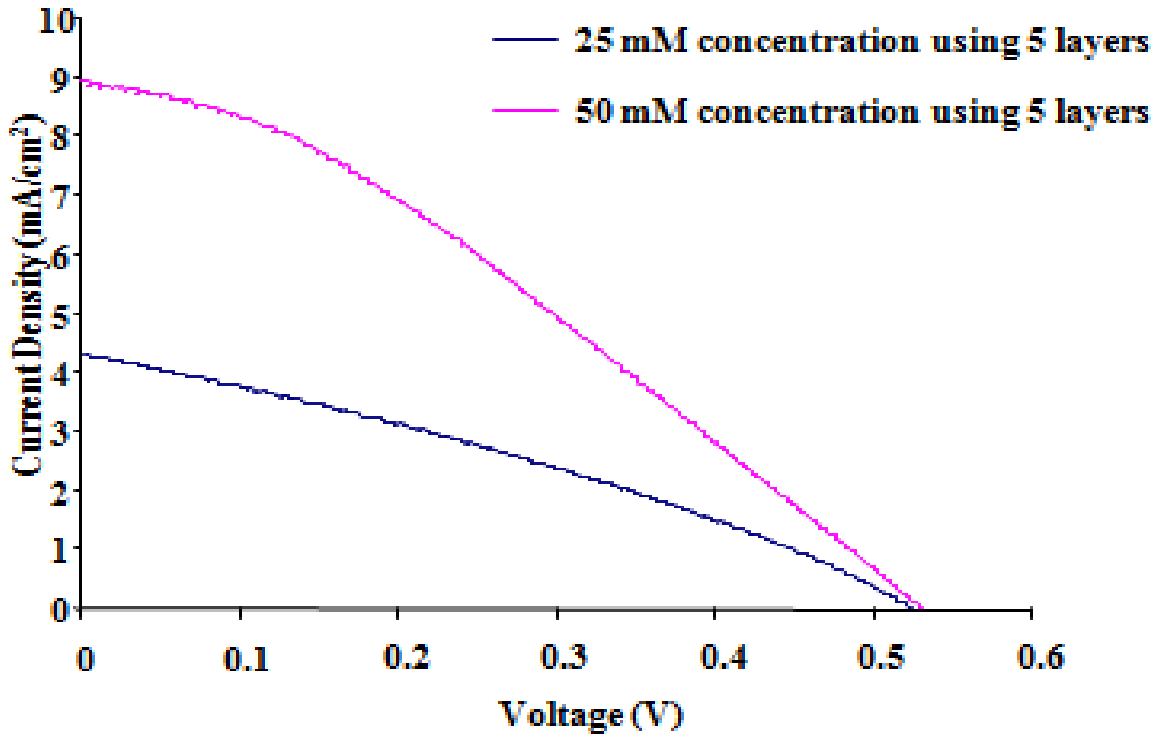

Figure 5.21 J-V curves of devices prepared using 5 layers of ZnO nanowire arrays using various equimolar concentrations of Zinc Nitrate Hexahydrate and HMTA.(Blue) 25 mM; (Pink) 50 mM.

Table 5.4 Photovoltaic characteristics of DSSCs based on 5 layers of ZnO NWs using different equimolar concentrations of Zinc Nitrate Hexahydrate and HMTA.

Concentration (mM)	V_{oc} (V)	J_{sc} (mA/cm^2)	FF	Efficiency (%)
25	0.524	4.32	0.316	0.72 ± 0.06
50	**0.529**	**8.95**	**0.319**	**1.51 ± 0.15**

The next study was to see if the block layer improved the performance of the 3D ZnO NW based DSSCs as it did with the 1D ZnO NW based DSSCs. Figure 5.22 shows the SEM images of the five-layered ZnO NW array (using 50 mM equimolar concentration of precursor solution) grown on a block layer coated FTO substrate. Although earlier studies proved that the hybrid TiO_2/P4VP BL was the optimal choice for electron recombination reduction and efficiency enhancement, the TiO_2 BL was studied here also. From Figure 5.23, it is evident that as expected, the incorporation of the block layer also improved the performance of the 3D ZnO NW based DSSC. While the inclusion of TiO_2 BL increased the average efficiency from 1.51% to 2.10%, the hybrid TiO_2/P4VP BL increased the average efficiency from 1.51 % to 2.82%. As expected, the highest V_{oc} in this particular study was produced in the case of the 50 mM-based DSSC using 5 ZnO NW layers and a hybrid TiO_2/P4VP BL. The full photovoltaic characteristics of this type of DSSC are provided in Table 5.5.

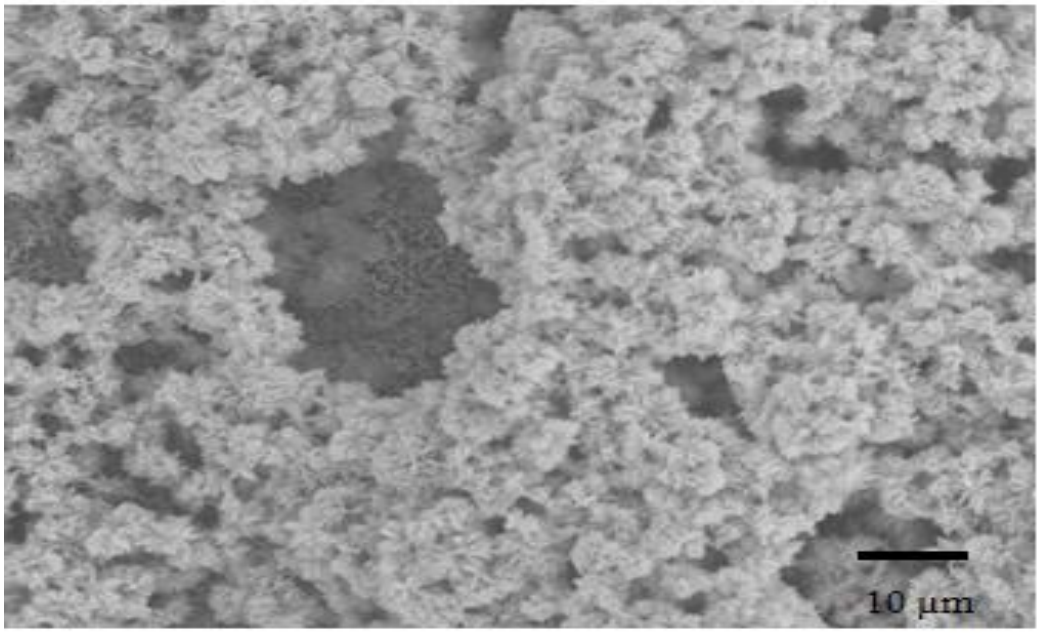

Figure 5.22 SEM image of 5 layered ZnO NW arrays using 50 mM equimolar precursor solution concentration with the hybrid TiO_2/P4VP block layer.

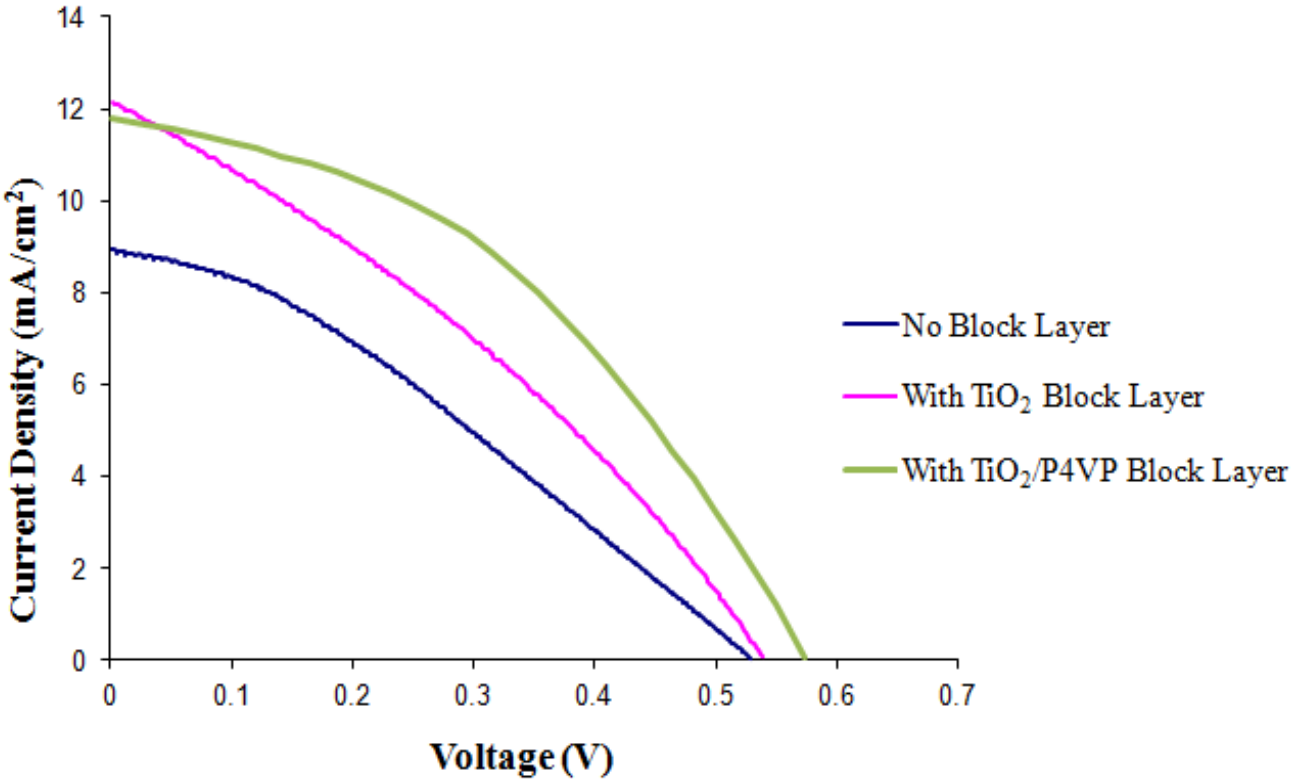

Figure 5.23 J-V curves of devices prepared using 5 layers of ZnO nanowire arrays using 50 mM equimolar concentrations of Zinc Nitrate Hexahydrate and HMTA. (Blue) without the BL; (Pink) with the TiO_2 BL; (Green) with the TiO_2/P4VP BL.

Table 5.5 Photovoltaic characteristics comparison of DSSCs based on 5 layers of ZnO NWs using 50 mM equimolar concentrations of Zinc Nitrate Hexahydrate and HMTA that are with or without the BL.

Block Layer	Concentration (mM)	Voc (V)	Jsc (mA/cm²)	FF	Efficiency (%)
No	50	0.529	8.95	0.319	1.51 ± 0.15
Yes- TiO_2 Block Layer	50	0.538	12.14	0.321	2.10 ± 0.28
Yes- TiO_2/P4VP Block Layer	50	0.573	11.79	0.418	2.82 ± 0.14

The physical characteristic data for the ZnO NWs observed in this study are shown in Table 5.6.

Table 5.6 ZnO NW Characteristic Data.

NW Array Type	Density, N	Length, L	Diameter, D
1D-25 mM-1st Layer	3.68 x 10^9 /cm^2	2.50 µm	70 nm
3D- 25 mM-2nd Layer	3.20 x 10^9 /cm^2	2.20 µm	72 nm
3D- 25 mM-3rd Layer	2.92 x 10^9 /cm^2	2.10 µm	80 nm
3D- 25 mM-4th Layer	2.78 x 10^9 /cm^2	3.60 µm	90 nm
3D- 25 mM-5th Layer	1.13 x 10^9 /cm^2	4.05 µm	150 nm
3D- 50 mM-5th Layer	2.33 x 10^9 /cm^2	4.20 µm	100 nm
3D- 50 mM-5th Layer w/ BL	1.95 x 10^9 /cm^2	4.25 µm	115 nm

Table 5.6 provides the approximate density of the top layer for varying number of layers of ZnO NW arrays. As a method of estimation of the nanowire density, SEM images were used to analyze the top layer of nanowires and the void areas to approximate the nanowire density. The data shows that there is a clear effect on the NW density and diameter as more layers are added. Earlier, it was inferred that the overall nanowire density increases as more layers of the nanowire array are added resulting in increasing J_{sc} values. However, as more layers are added, the NW density tends to decrease and the diameter tends to increase for that corresponding top

layer. This trend makes sense if you look at it from a seed layer point of view. Mentioned as a possible growth mechanism in Chapter 2, crystal sizes tend to be smaller on thicker seed layers and small crystal sizes induces the growth of nanowires with smaller diameters. Moreover, as we apply more seed layer during each layer growth, the seed layer may not lay solely on the top surface; instead, some of the seed solution percolates through to previous layers of NW arrays. Therefore, the seed layer of the top layer tends to get thinner as you grow more layers. This would explain why the seed crystals are larger, thus growing NWs of larger diameters. Furthermore, the increase in diameter of the ZnO NW arrays on the top layer will cause a decrease in the NW density of that top layer on the same size substrate. Another point of view is based on the fact that there is less space in between the nanowires in a very dense array, which increases the time it takes for complete diffusion of Zn^{2+}. This slow diffusion then allows for the slower lateral growth of the nanowires (i.e., dense nanowires tend to yield thinner nanowires). Moreover, some researchers believe dense nanowires are relatively shorter, but in this study we have found that the effect of seed layer thickness on NW length does not follow any apparent trend. Lastly, comparing the 5^{th} layer based on 25 mM to the 5^{th} layer based on 50 mM, we see that density does slightly improve. This result confirms our assumption that improving the nanowire density can be achieved by increasing the precursor concentration.

5.2.4 Brief Summary

The flowerlike 3D ZnO nanowire structures were successfully fabricated in this study in an effort to enhance the surface area and increase the density of the ZnO nanowire array and effectively improve light harvesting of the DSSC. The results of this study showed that as the number of layers in the structure increases, the average overall efficiency increases as well. With ZnO nanowires grown using a 25 mM precursor solution, five layers of the 3D arrays yielded an average efficiency of 0.72%. Then, we investigated the effect of precursor concentration of the 3D nanowire arrays formed on the efficiency. It was determined that with ZnO nanowires grown using a 50 mM precursor solution, five layers of the 3D arrays yielded an average efficiency of 1.51%. The efficiency results in the case employing the 25 mM concentration and the case employing the 50 mM concentration gave results that were more than 70 times and more than 150 times higher than that of an unmodified 1D ZnO nanowire based DSSC, respectively. Then, to confirm earlier studies exploring the effects of the block layer, this study analyzed the result of including a block layer into the design of a 3D ZnO nanowire based DSSC. The results confirmed that the efficiency results in the case employing the TiO_2 block layer and the case employing the TiO_2/P4VP hybrid block layer gave results that were more than 200 times and more than 280 times higher than that of an unmodified 1D ZnO nanowire based DSSC, respectively.

5.3 Ultra Dense Hierarchal Design of Zinc Oxide Nanowire Dye-Sensitized Solar Cells

5.3.1 Introduction

The 3D scheme has proven to enhance the conversion efficiency of the ZnO NW based DSSC greatly; therefore, it was imperative to continue investigating other 3D based designs that could further enhance its efficiency. In addition to studying the growth of 1D secondary ZnO NWs from the tips of the primary backbone of NWs, this work also looks at growing 3D secondary NWs from the primary layer of NWs. This idea stems from many reports of multi-layered and/ or branching ZnO NW structures. It is already clear that the enhanced surface area will significantly increase the conversion efficiency due to a larger amount of dye adsorption; moreover, the multiple layers of branching can increase the number of channels available for the light to pass through or get absorbed by the cell.

Xu et al. investigated specifically the benefits of synthesizing vertically aligned multilayers of ZnO NWs [103]. Their research exhibits a feasible approach to fabricating multilayer ZnO NW structures with the aid of a self-assembled monolayer (SAM) coating process. As seen in Figure 5.24, each layer grows ~10 μm length nanowires. Moreover, through the use of octadecyltrichlorosilane as the SAM, they were able to prevent wire fusion for subsequent layers [103]. The SAM on the top of the first layer is removed via ultraviolet ozone treatment, while the SAM between the nanowires remain to ensure that the growth solution does not penetrate between the sidewalls of the first layer of nanowires during the growth process of the second layer of nanowires [103]. Figure 5.25 provides SEM images of two layers of ZnO NW arrays fabricated by Xu et al.

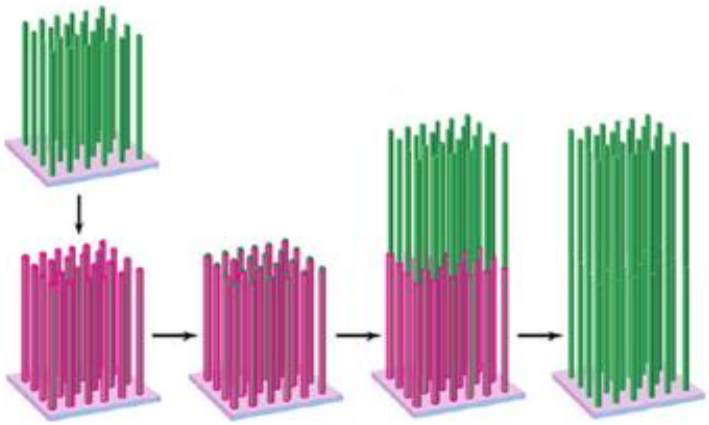

Figure 5.24 Schematic process for synthesizing a two-layer assembly of ZnO NW arrays on transparent conducting oxide, green represents NWs and pink represents SAM [103].

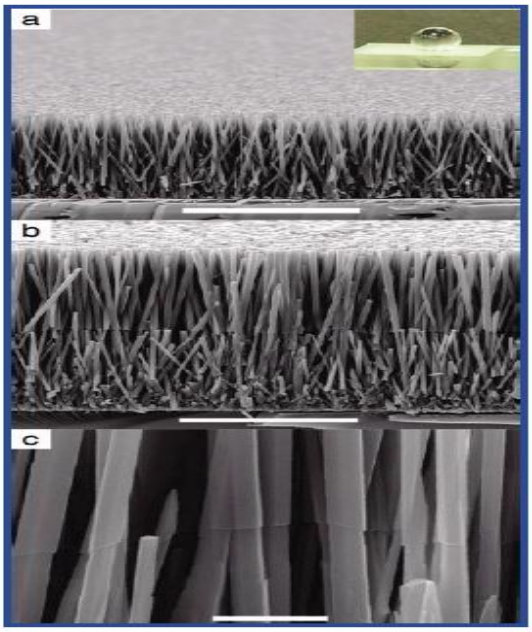

Figure 5.25 SEM images. (a) First layer ZnO NW array, scale bar 10 μm; inset-optical image of a water droplet on the array after it was coated with a SAM; (b) Two-layer assembly of ZnO NW arrays, scale bar 10 μm; (c) Junction between the first and second layer of ZnO NWs, scale bar 500 nm [103].

Branched tree-like ZnO NW structures were investigated by Ko et al [138]. Specifically, they enhance dye loading and light harvesting by synthesizing high surface area hierarchal ZnO

NW for DSSCS. Their specific growth mechanism is based on the combination of length-wise growth and branched growth, where the ZnO NWs are grown from ZnO quantum dot seeds [138]. With these hierarchal ZnO NW photoanode, they report an overall conversion efficiency of 2.63 % [138]. Figure 5.26 provides an illustration and SEM image of their branched ZnO "Nanoforest" structure.

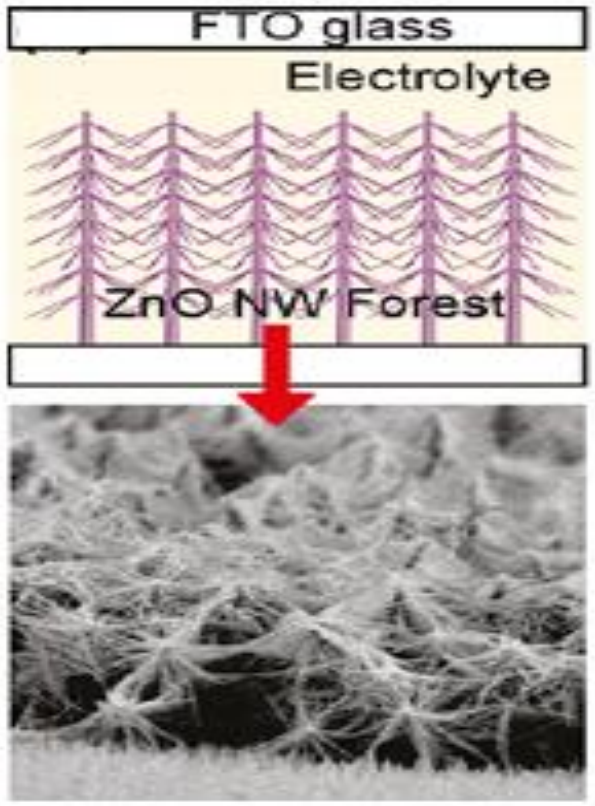

Figure 5.26 Schematic of Hierarchal ZnO Nanoforest and SEM of the ZnO Nanoforest [138].

In this work, the goal is to combine both ideas of multilayered ZnO NWs and branched NWs in order to get an optimized array of highly dense 3D ZnO NWs that will improve dye loading, increase light harvesting, and greatly increase the overall power conversion efficiency. More importantly, it is necessary to design a unique method of applying the seed layer that will

result in distinct multiple layers of the ZnO NW arrays. In the previous section the various NW arrays were based on applying the seed solution via spin coating, as done commonly in the literature, which allows the ZnO seeds to pass between the nanowires and attach to various positions along the sidewalls of the nanowires. With this type of seed application the nanowires can only grow outward and/or upward from the base nanowire. Also, it is very difficult for the nanowires to grow in between the nanowires and this can affect the density of the nanowire array. But more importantly, because the ZnO seeds will fall between the nanowires of the previous layers upon reapplication of the seed layer via spin coating, it is even more difficult to grow subsequent layers from the top of the previous layer that are visibly distinct from former layers. Figure 5.27 illustrates the limitations of applying the seed layer via spin coating of the ZnO seed solution. From this figure, it is clear that the seeds attach to random locations along the side walls of the nanowires, and some nanowires may not have seeds at the tips of the nanowires to grow distinct subsequent layers. Also, at some locations, the seed does not yield nanowires because it may be too difficult for the crystals to grow in between the nanowires, which results in the aggregation of the seeds between the nanowires as seen in the SEM image.

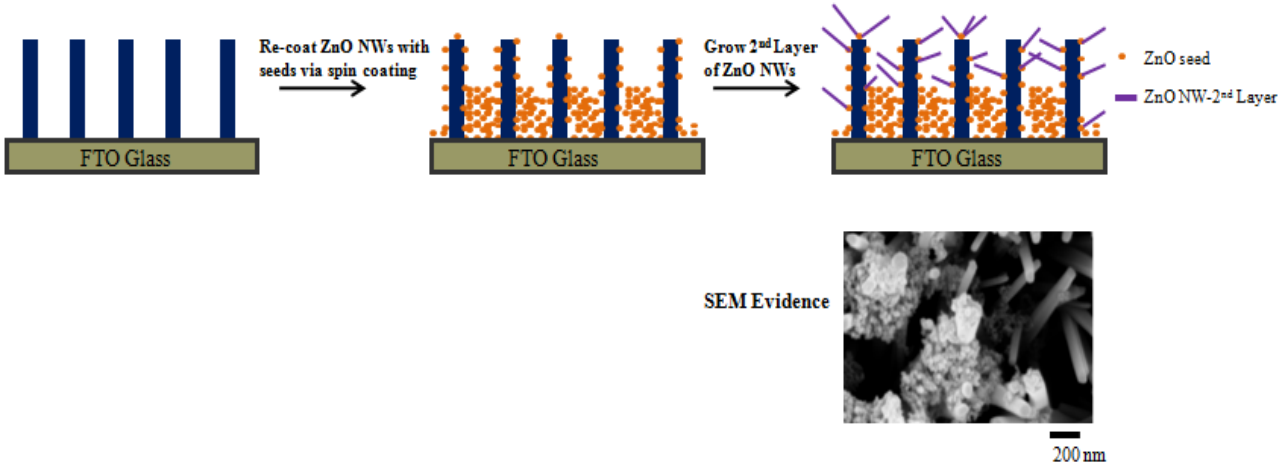

Figure 5.27 (Top) Schematic displaying limitations with using the spin coating method to reapply ZnO seeds to form subsequent layers of ZnO NW array; (Bottom) SEM image of large crystal seeds clustered on NW sidewalls.

Contrastingly, here we report a seed application method based on the electrospinning of ZnO nanofibers as seeds. This technique eliminates the occurrence of seeds penetrating along the sidewalls of the ZnO NWs. Instead, these nanofibers lie directly on top of the NW array, allowing the subsequent layers of ZnO NWs to build upward in a clear and distinct fashion. Furthermore, the multiple arrays of ZnO NWs will be able to grow in a 360° fashion along the entire length of the nanofibers, yielding multi-dimensional nanostructures. Figure 5.28 illustrates the design process based on electrospinning of the nanofiber seeds.

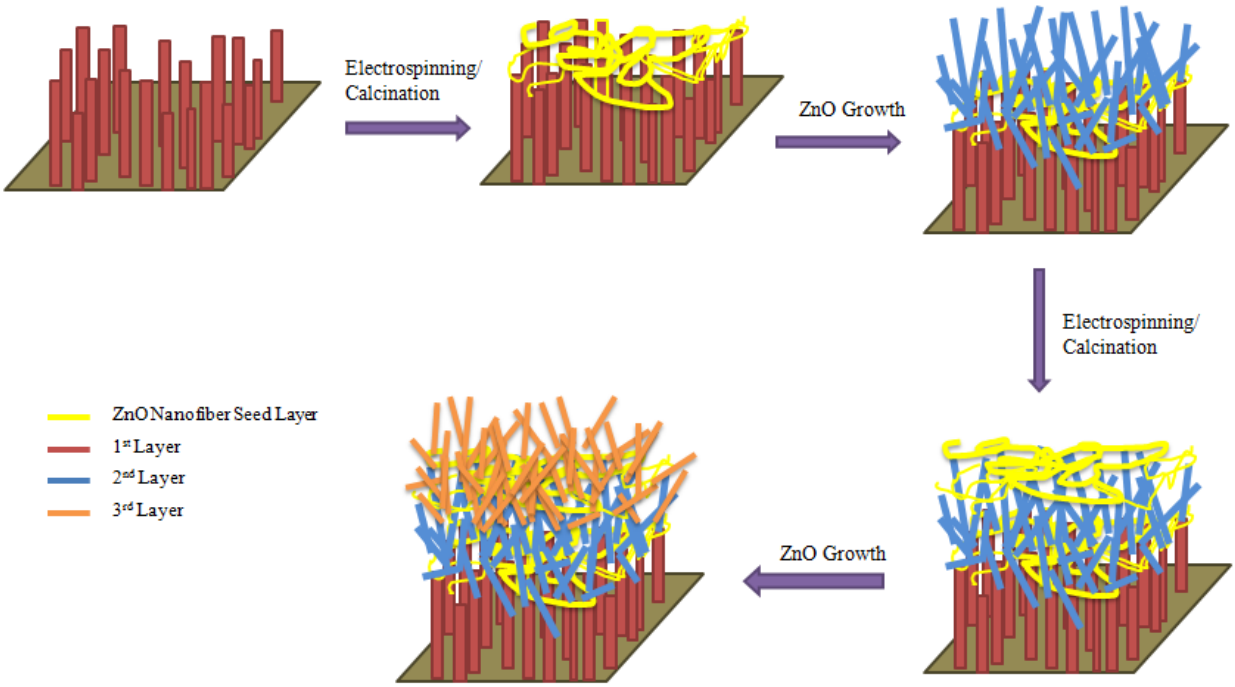

Figure 5.28 Schematic of design process for ultra dense multilayers of ZnO NW arrays via the electrospinning of ZnO nanofiber seeds.

5.3.2 Experimental Procedure

Fabrication of ZnO Nanowires

ZnO NWs were synthesized using a hydrothermal chemical solution based method. High-density ZnO NWs were grown on 1x1 cm^2 seeded fluorine-doped tin oxide (FTO) substrates via the following steps. Fabrication of the ZnO nanofibers as the seed layer on FTO was conducted via the electrospinning of a seed precursor solution containing polyvinylpyrrolidone (PVP) to form the film layer. The polymer-based seed solution was prepared by adding 0.5 g of zinc acetate dihydrate to 15 mL of pure ethanol with magnetic stirring at room temperature for 1h, followed by adding 10 g of PVP powder (Aldrich-MW 55,000) to the mixed solution with magnetic stirring at room temperature for at least 8 hrs to obtain a homogenous solution. The homogenous seed precursor-containing polymer solution was then poured into a plastic pipette tip for electrospinning. The plastic pipette tip was placed at an angle of approximately 15° to control the flow rate of the polymer solution, and the distance between the pipette tip and the collector was fixed at 15 cm. A voltage of 20 kV was applied for electrospinning for 30 sec to 1 min. The layer of seed nanofibers were collected on multiple substrates that were fastened to a secured stainless steel plate. The electrospun nanofibers were calcined at 600^oC for 4h in a muffle furnace with a heating rate of 2^oC/min to completely burn the PVP polymer and form the ZnO nanocrystalline layer. Figure 5.29 shows a schematic of the electrospinning apparatus, while Figure 5.30 provides the actual setup for the electrospinning process of the ZnO nanofiber seed layers.

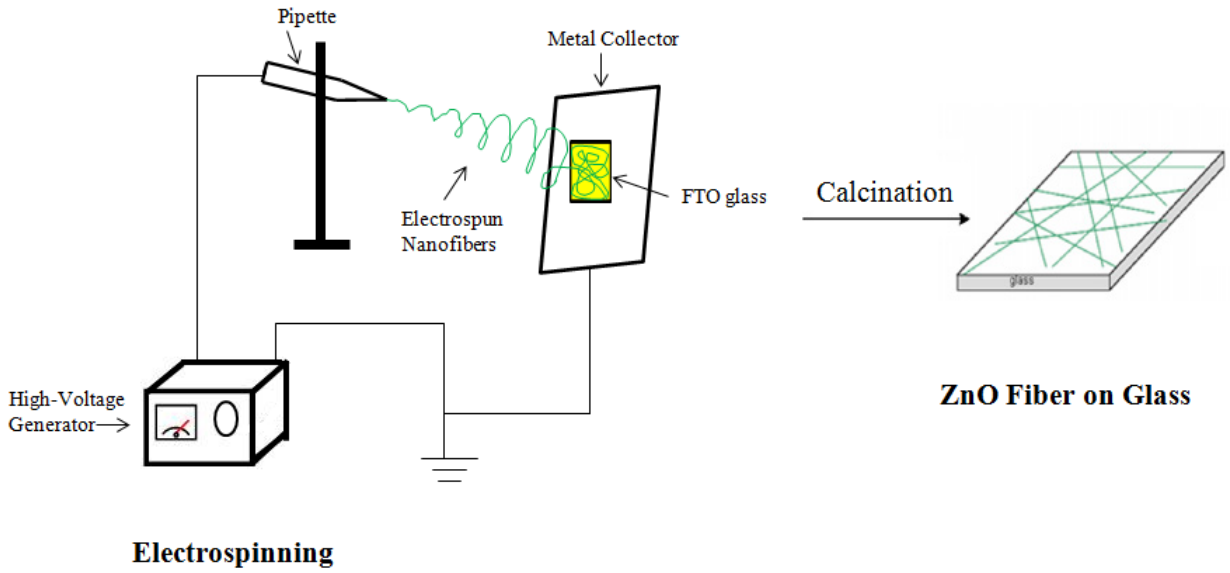

Figure 5.29 Schematic illustration for the electrospinning apparatus used in the fabrication of ZnO nanofibers. Adapted from [139].

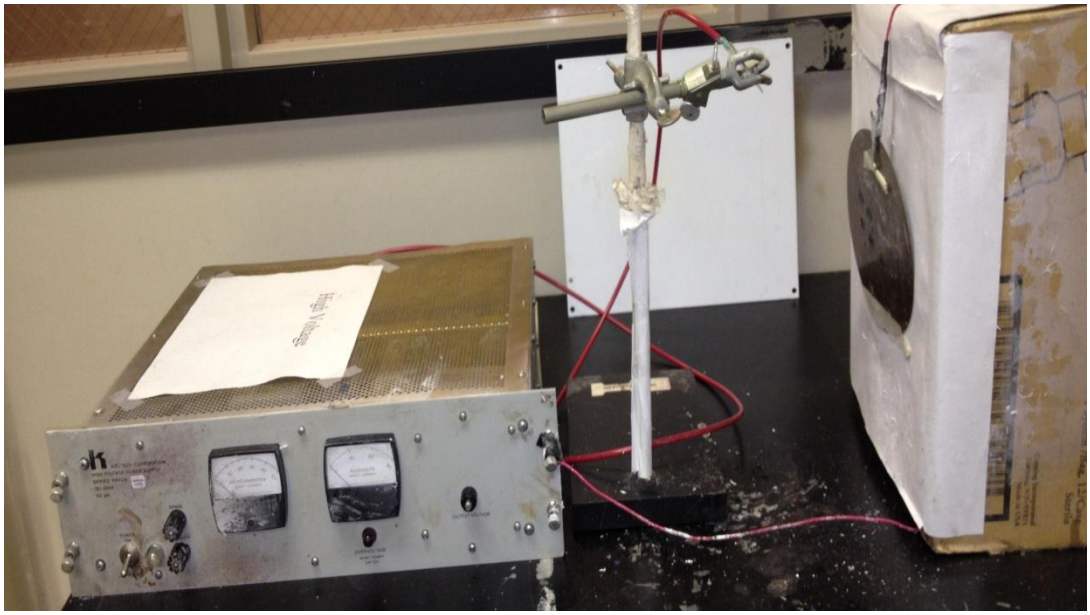

Figure 5.30 Setup for Electrospinning ZnO nanofiber seed layers.

The seeded substrates were then fastened to the top of the chemical solution in a capped vessel. ZnO NWs were grown from the seed layer using a chemical bath deposition method in a 50 mM or 75 mM equimolar aqueous solution of zinc nitrate 6-hydrate and HMTA and 10 mM PEI at 90°C for 2.5 h. The samples were then placed in another fresh growth solution (50 mM or 75 mM equimolar aqueous solution zinc nitrate 6-hydrate and HMTA) for another 2.5 hrs at 90°C. Substrates were subsequently rinsed with deionized water and ethanol and oven dried at 95° C for 30 min in air. This provided one layer of the ZnO nanowire array. To obtain subsequent layers, the same method was carried out for each layer: 1) the seed application onto the FTO substrate via the electrospinning of the polymer based seed solution; and 2) growth of another ZnO NW array from the seed layer directly on top of the previous ZnO NW array. As-grown ZnO NWs could be annealed further in air at 400°C for 30 min to improve the crystallinity of the NWs and the interfacial structures.

DSSC Assembly

The DSSC assembly and solar cell characterization process were performed in the same manner that was explained in Section 5.1.2.

5.3.3 Experimental Results and Characterization

The key concept in this particular study is the benefits gained by applying the ZnO seed layer via electrospinning of ZnO nanofibers. The use of the nanofibers as seed layers between the multiple layers of the ZnO NW arrays prevents seeds from penetrating in between the nanowires and attaching to the side walls of the nanowires. Instead, nanofibers only lie directly on top of the previous array of nanowires, which results in distinct multiple layers of the ZnO NW arrays. Figure 5.31 provides images of the first layer of ZnO NF on the bare FTO surface before and after calcination.

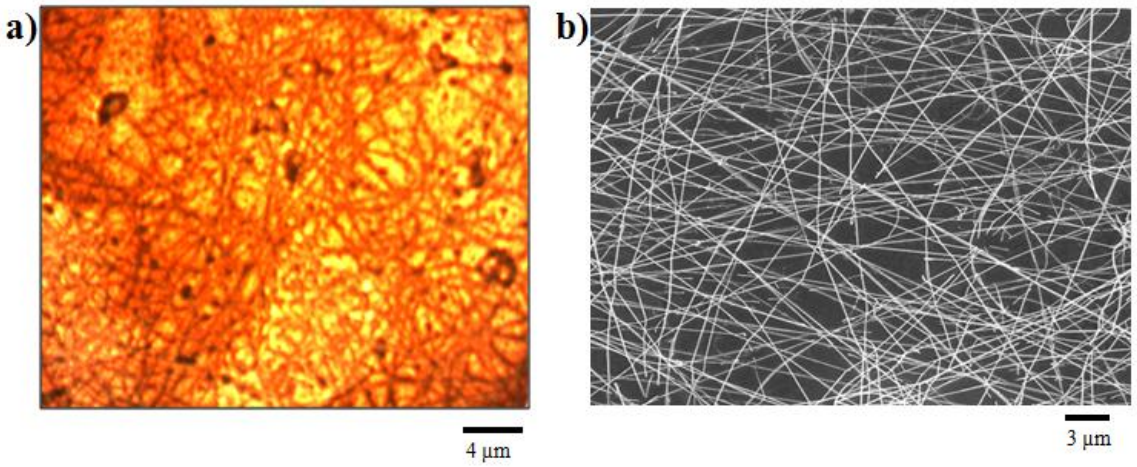

Figure 5.31 Images of the ZnO NF. (a) Microscopic image before calcination at 600°C; (b) SEM image after calcination at 600°C.

From the images, we can see that the nanofibers form a web-like pattern across the substrate. Figure 5.32 shows the SEM images of one layer of ZnO NW arrays grown on electrospun ZnO NF seeds at various magnifications. It is clear from all images that the ZnO NWs grow along the web-like pattern only and there are some empty spaces along the substrates where no nanowires exist.

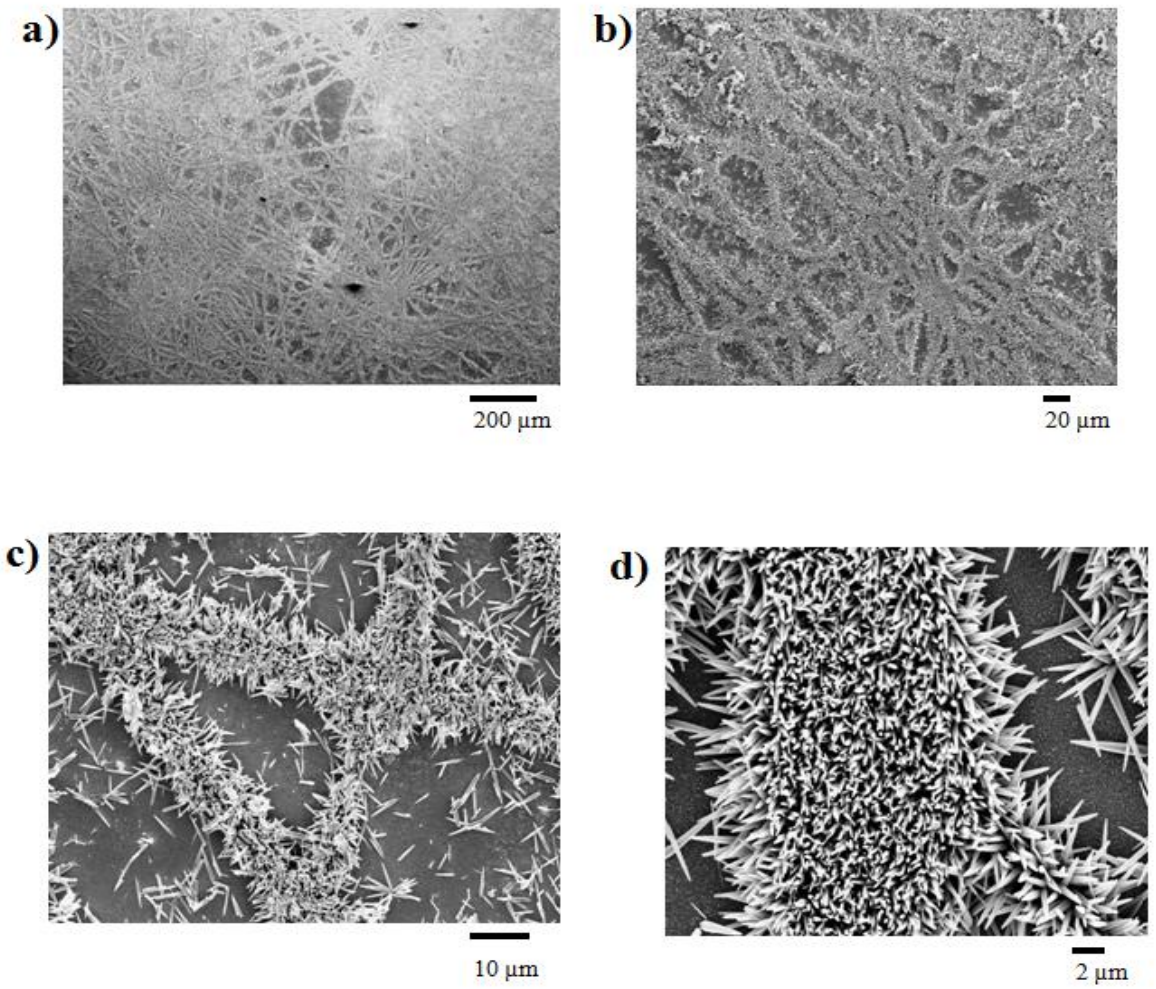

Figure 5.32 SEM images of one layer of ZnO NW arrays grown on electrospun ZnO NF as seed at various magnifications. a) 186 X magnification; b) 695 X; c) 3.09K X; d) 9.41K X.

In efforts to study this multilayer structure thoroughly, we aimed to fabricate a two layer structure of ZnO NW arrays from ZnO NF seeds, as shown in Figure 5.33, without any branching evident. The nanowires had an average length of approximately 2.5 µm, and the distinction between the separate layers was quite clear. We believe this is due to the fact that the seed layers are ZnO nanofibers.

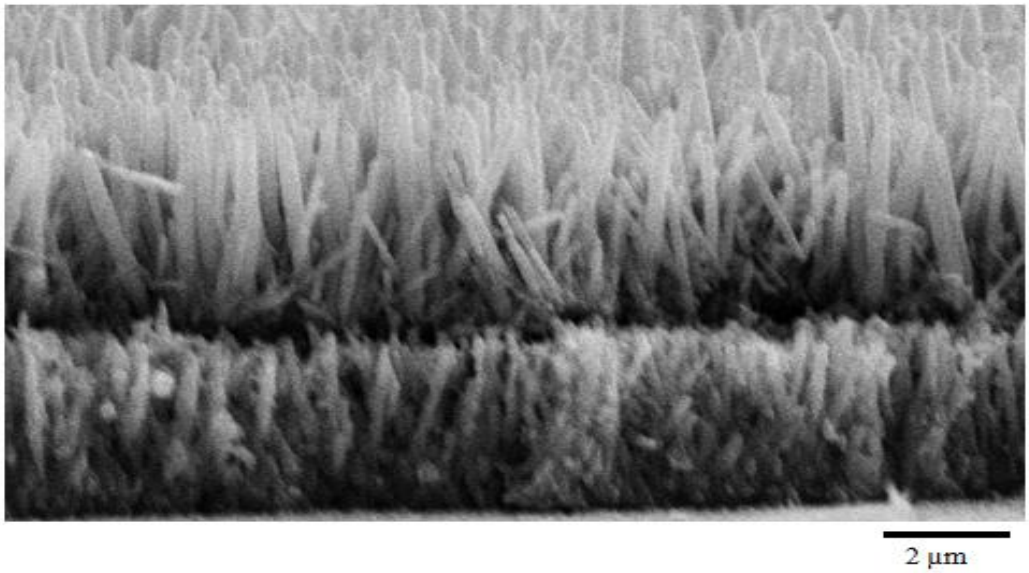

Figure 5.33 SEM image of the 2 layers of ZnO NW arrays grown using LBL method with electrospun ZnO NF as seed.

After successfully fabricating two layers via this ZnO NF approach, the next goal was to fabricate up to 5 different layers. Figures 5.34-5.35 and Figures 5.37-5.38 show SEM images of multiple layers (2-5) of unique branched ZnO NW structures.

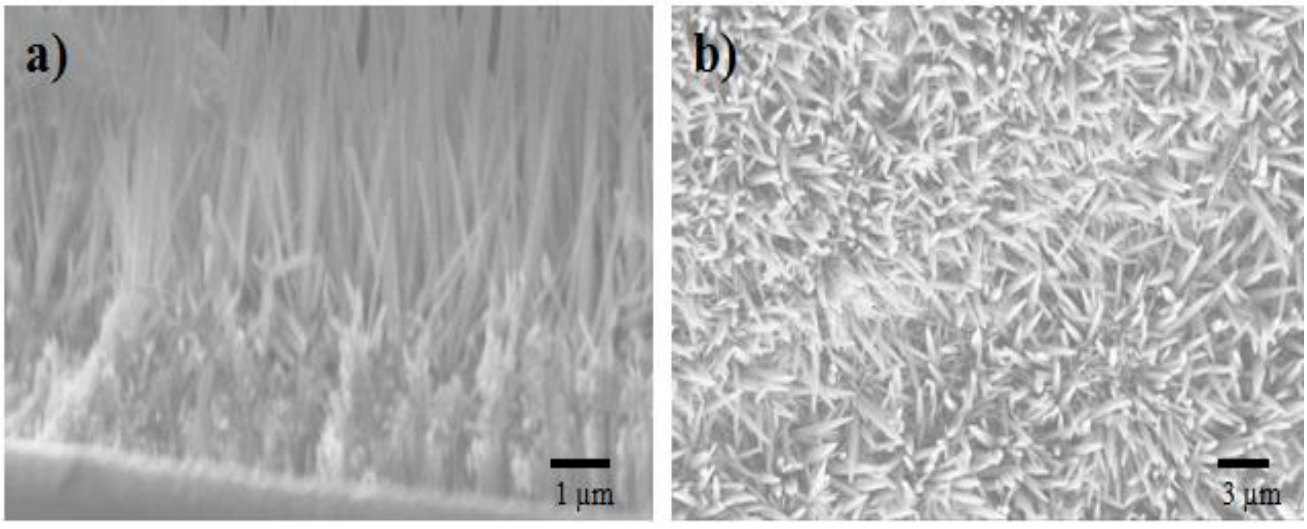

Figure 5.34 SEM images of 2 layer-branched ZnO NWs. a) Side view; b) top view.

For the third layer and subsequent layers, the ZnO NW morphology became very interesting. In particular, we began to see strong evidence of 3D "caterpillar-like" structures. These arrays were highly dense, and followed the same specific pattern of the ZnO nanofibers. The unique result here was that the ZnO NWs are able to grow in all directions around the nanofibers (see Figure 5.35).

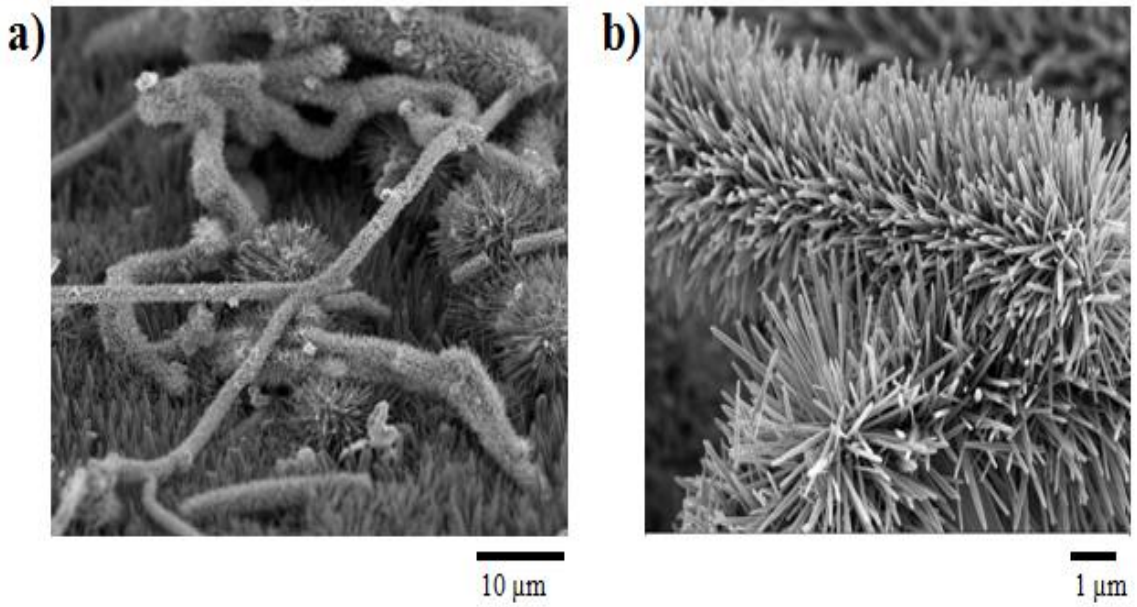

Figure 5.35 SEM images of 3D "caterpillar-like" ZnO NWs grown from ZnO NF seeds. (a) view of 3 layers of multiple "caterpillar-like" ZnO NW structures; (b) close up view of NWs grown from NF seeds to form "caterpillar-like" structure.

Because of the electrospun nanofiber seeds, these "caterpillar-like" ZnO NW structures formed literally allowed growth of the nanowires along a 360° path around the entire length of the nanofibers. More importantly, the nanowires that form were extremely high in density (varying between 8 $x10^{10}/cm^2$-1 $x10^{11}$) and small in diameter (~50 nm), and this contributes to enhanced light absorption that ultimately improves the conversion efficiency of the DSSC significantly. By comparing the most ideal synthesized 1D ZnO nanowire array to the 3D ZnO NW arrays grown in this study, it is clear that the technique that utilized electrospun nanofibers as the seeds resulted in denser and thinner nanowires (see Figure 5.36).

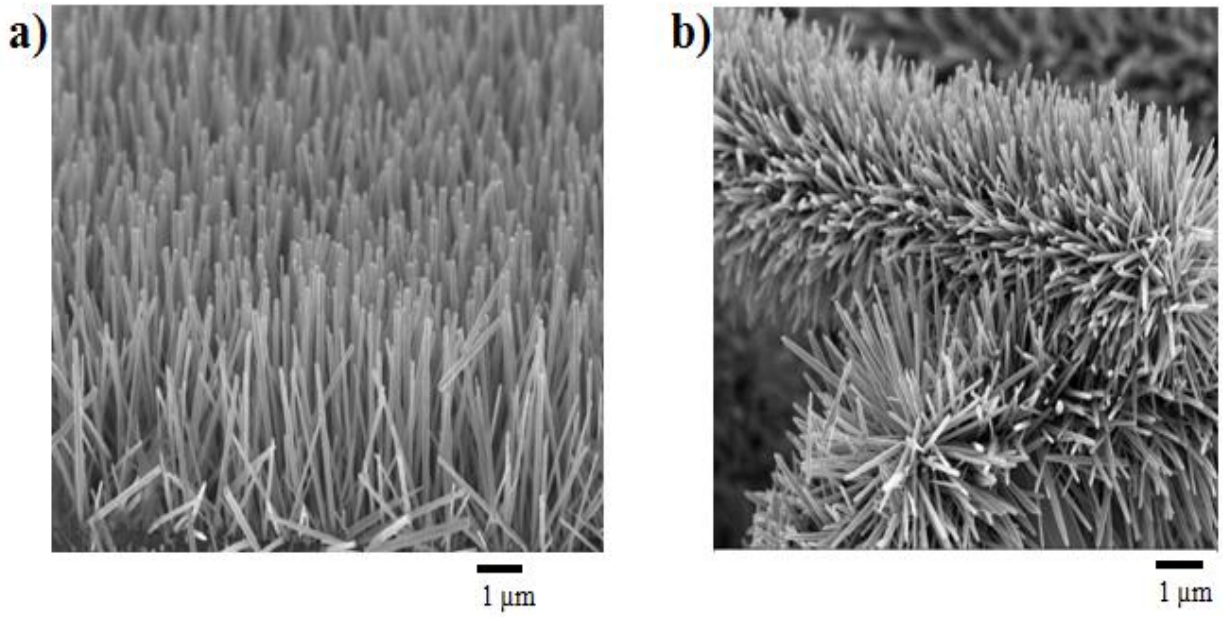

Figure 5.36 a) 1D ZnO NW array with density ~2 $x10^9/cm^2$ and diameter ~90 nm; b) 3D ZnO NW array with density ~1 $x10^{11}/cm^2$ and diameter ~50 nm.

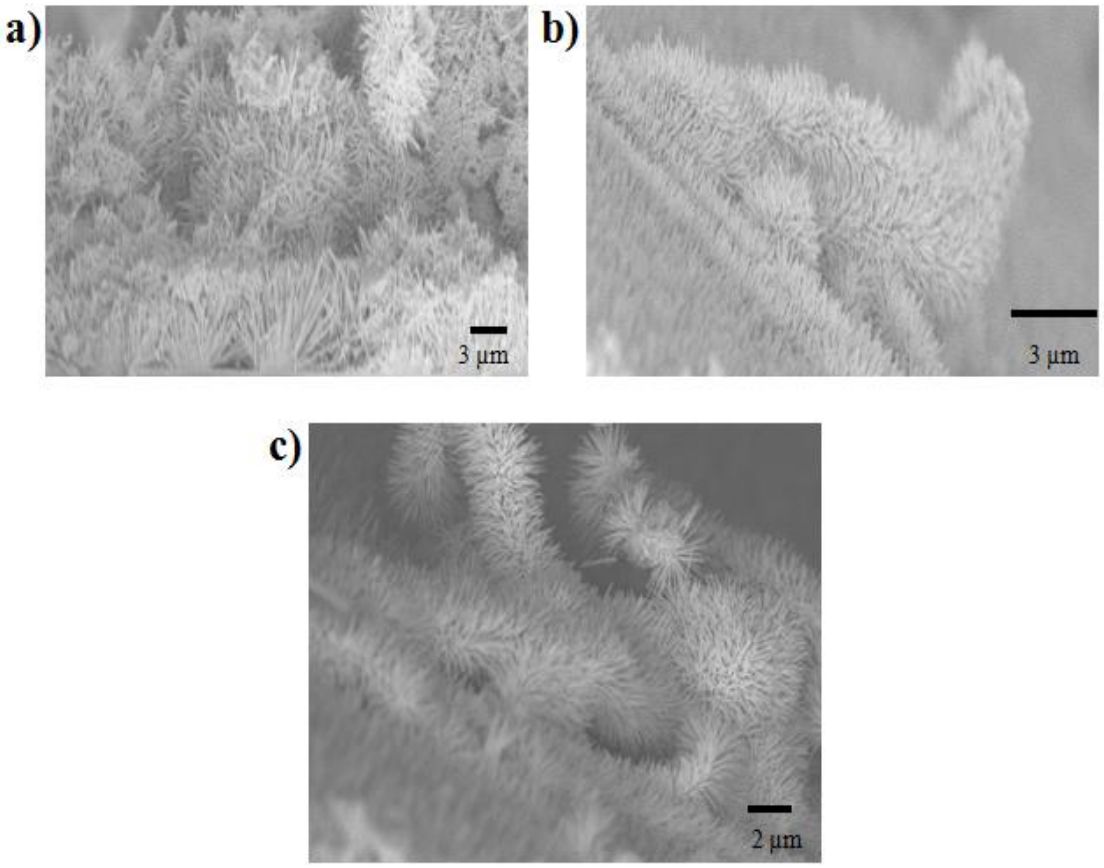

Figure 5.37 SEM images of 4 layers of ZnO NWs grown from ZnO NF seeds. a) front view; b) side view; c) side view tilted at 60°.

Again in Figure 5.37, we see the combining of multiple layers (4 layers) of these much denser and thinner nanowires. Lastly, in the case of 5 layers, we observed a portion of the substrate that was covered with these multi-dimensional flowers exhibiting grandiose budding effects in addition to the "caterpillar-like" structures. Evidence of the budding multi-dimensional flower is shown in Figure 5.38.

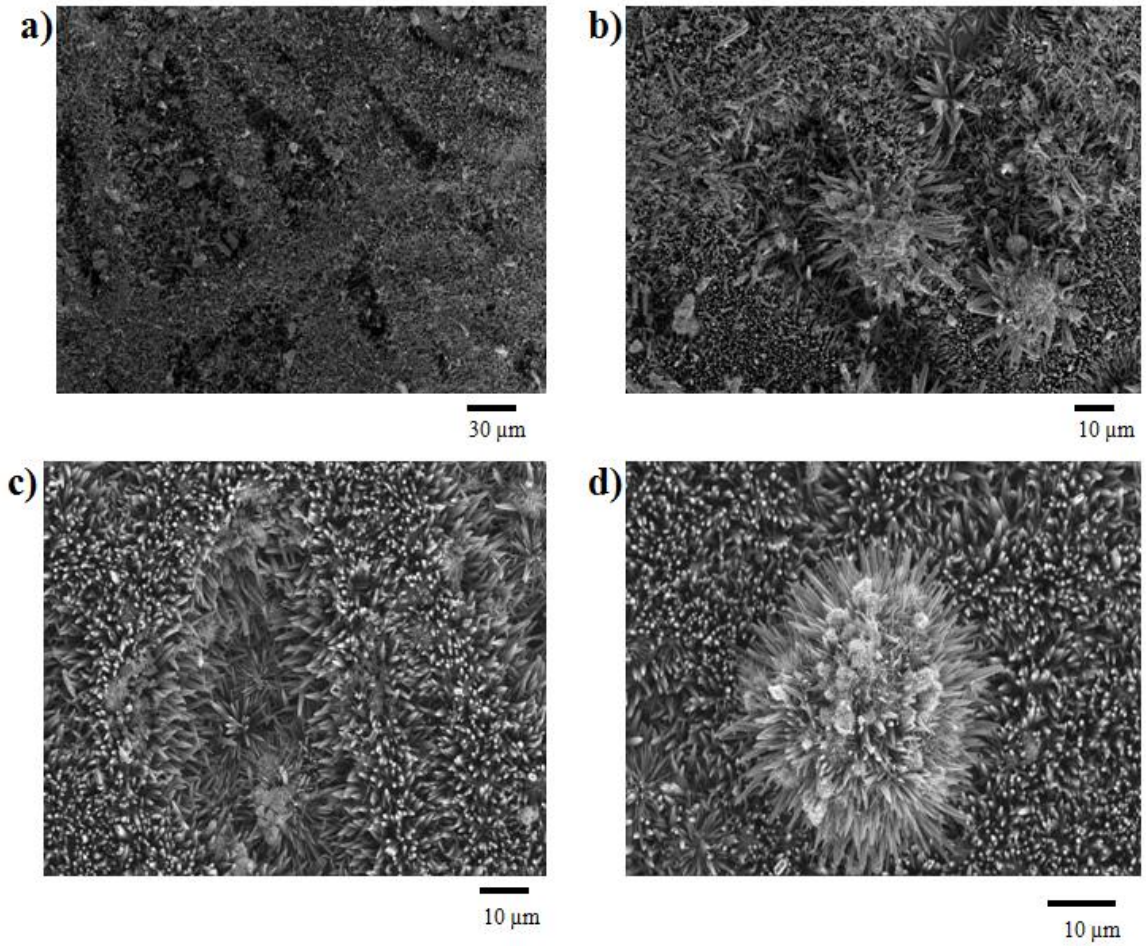

Figure 5.38 SEM images of 5 layers of ZnO NWs grown from ZnO NF seeds at various magnifications. a) 900 X magnification; b) 2.03K X; c) 2.81K X; d) 3.57K X.

For characterization purposes, XRD analysis was performed on the sample of a multilayered array of ZnO NWs in efforts to verify the presence of crystalline ZnO. The XRD spectrum is provided in Figure 5.39.

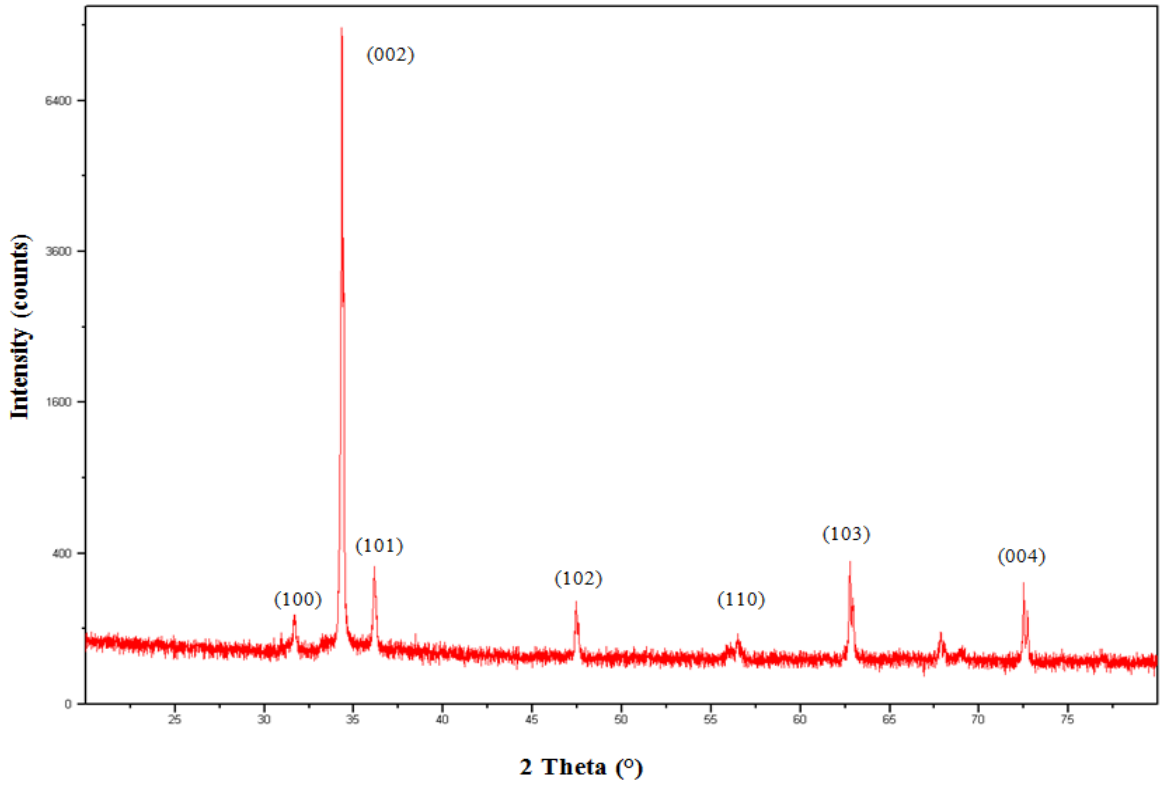

Figure 5.39 XRD spectrum of 3D multilayered array of ZnO nanowires.

The XRD displays diffraction peaks of (100), (002), (101), (102), (110), (103), and (004) planes that correspond to the ZnO hexagonal wurtzite structure in the literature. The strong appearance of the (002) diffraction peak at 34.6° confirms the [001] as the fastest growth direction and verifies the high degree of crystallinity of the ZnO NWs. Compared to the 1D case, the intensity is lower at the (002) peak, but that should be due to the affinity of the multilayered structures to grow in other directions that allow a lesser degree of vertical alignment.

More importantly, the results of the average efficiencies of these multilayered structures based on ZnO NF seeds were remarkable in comparison with results from earlier studies. In the case where the precursor solution concentration was 50 mM, the average efficiency ranged from 0.91 – 2.45 % efficiency, as seen in Figure 5.40 and Table 5.7. Furthermore, we decided to increase the precursor solution concentration to 75 mM for this particular study to see if the efficiency can be further enhanced. Figure 5.41 and Table 5.8 show that the average efficiency ranged from 3.43 – 5.20 %. And while the BL was not incorporated into these designs, based on our previous results, it is expected that the performance of these devices would be further enhanced.

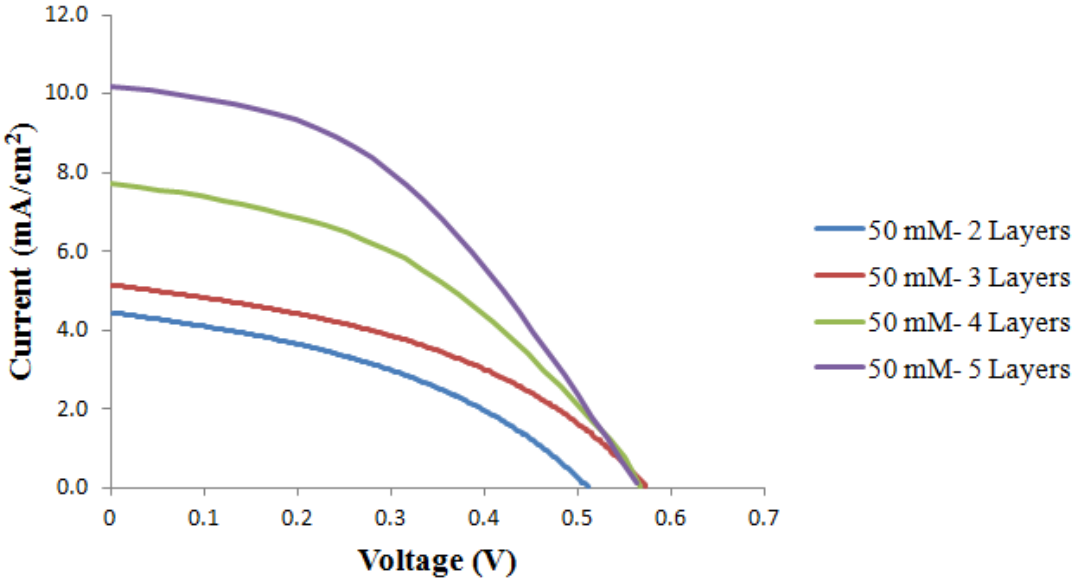

Figure 5.40 J-V curves of multilayered NW arrays grown using LBL method with electrospun ZnO NF as seed and a 50 mM precursor solution.

Table 5.7 Photovoltaic Characteristics of multilayered NW arrays grown using LBL method with electrospun ZnO NF as seed and a 50 mM precursor solution.

Number of Layers	V_{oc} (V)	J_{sc} (mA/cm²)	FF	Efficiency (%)
5	**0.56**	**10.16**	**0.43**	**2.45 ±0.21**
4	0.57	7.72	0.43	1.88 ± 0.17
3	0.57	5.15	0.42	1.23 ± 0.08
2	0.51	4.45	0.40	0.91 ± 0.11

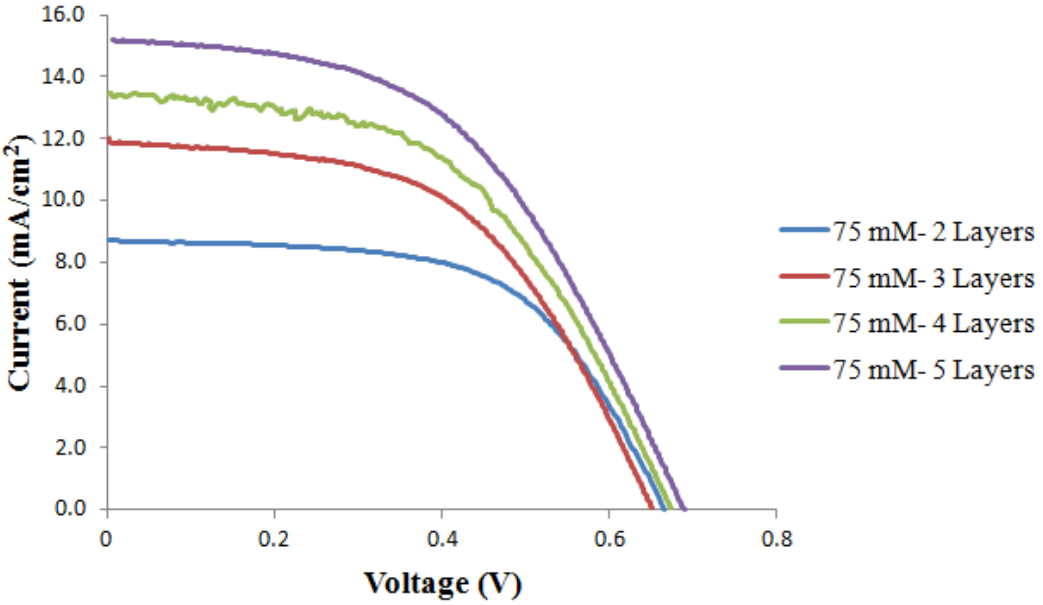

Figure 5.41 J-V curves of multilayered NW arrays grown using LBL method with electrospun ZnO NF as seed and a 75 mM precursor solution.

Table 5.8 Photovoltaic Characteristics of multilayered NW arrays grown using LBL method with electrospun ZnO NF as seed and a 75 mM precursor solution.

Number of Layers	V_{oc} (V)	J_{sc} (mA/cm²)	FF	Efficiency (%)
5	**0.69**	**15.20**	**0.50**	**5.20 ± 0.13**
4	0.68	13.47	0.51	4.67 ± 0.16
3	0.65	12.01	0.53	4.14 ± 0.12
2	0.67	8.69	0.59	3.43 ± 0.23

Ultimately, these results have shown that enhancing surface area and density through unique multilayered designs can replace the idea of synthesizing long NWs in efforts to improve the overall efficiency of the DSSC. The ultra dense nanowires formed allowed for a significant increase in J_{sc}. Moreover, the enhancement of surface area and density is directly correlated to the increase in light absorption. Moreover, applying the model in Chapter 4 using the physical dimensions of one layer of these ultra dense ZnO nanowire arrays as model parameters (i.e., length of ~3 μm, radius of ~25 nm, and density of ~$1x10^{11}/cm^2$), the light harvesting efficiency is approximated as ~96%. Thus, as expected, an enhanced light harvesting efficiency results in improved DSSC performance.

5.3.4 Brief Summary

The objective of this study was to create a 3D ZnO nanowire based DSSC design that would further enhance the light absorption of the cell and ultimately further improve the DSSC power conversion efficiency. A branched-multilayered design of ZnO nanowire arrays based on ZnO nanofiber seed layers was chosen and it was proven to be the most successful of all the investigated designs. This technique utilized electrospun nanofiber seeds, which resulted in denser and thinner nanowires that improve the light absorption of the DSSC and ultimately improves its conversion efficiency as well. More importantly, this experimental value of 5.20% is the highest reported value for 3D ZnO NW based DSSCs. The SEM images showed unique web-like patterns that the ZnO NWs grew along, which illustrate a feasible way to grow patterned aligned nanostructures on the substrate. Moreover, these arrays formed the unique "caterpillar-like" structures that occurred due to the distinctive multidirectional growth from the nanofibers. With the five layered structure of branched ZnO nanowires grown from ZnO nanofiber seed layers, the average efficiency of 5.20% is more than 500 times higher than the unmodified 1D ZnO nanowire based DSSC.

CHAPTER 6

CONCLUSIONS

There is still a lot of skepticism regarding the feasibility and effectiveness of employing DSSCs in the real world on a large industrial scale as one of the leading sources of energy. However, throughout this report, experimental data have shown that ZnO nanowire-based DSSCs in particular have a great deal of potential in the field of renewable energy. We have confirmed that the hydrothermal synthesis of the ZnO nanowires used in DSSC research has many advantages including the employment of lower reaction temperatures, inexpensive production costs, process simplicity and less rigorous synthesis conditions. The XRD spectrum verified the crystallinity and vertical alignment of the ZnO nanowires grown on FTO substrates under optimal conditions.

There were both experimental and modeling investigations performed to determine the highest possible performance abilities of specific DSSC designs based on ZnO nanowires. Specifically, the development of a theoretical model was explored in efforts to investigate how the geometry of ZnO nanowires affects the incident photon-to-current conversion efficiency of 1D ZnO nanowire-based N719-sensitized solar cells at the maximum absorption wavelength of 543 nm. This model allows one to see how the affects of geometry is coupled between both the LHE and APCE. So, it is important to understand how various combinations of the radius, length, and density affect the overall results of IPCE. This model allows you to approximate the optimal combination of the ZnO nanowire physical dimensions under specific constant parameters. The model revealed the important balance of having long enough nanowires that

contribute to the needed high surface area for greater light absorption, but at the same time are not too long where the charge collection efficiency is negatively affected due to L<<< d. The model also allows one to investigate the effects of using materials with fewer trap sites, high electron diffusivity, and slower recombination times. Additionally, from the results of the model we are able to see that the properties of the dye (e.g., the extinction coefficient) play a crucial role in the surface area needed to absorb high levels of light. Utilizing dyes with high extinction coefficient allows greater light absorption, which is very advantageous for shorter nanowire lengths. There ultimately has to be an optimal combination of the physical dimensions (i.e., surface area), dye loading, as well as recombination rate to yield both 100% LHE and 100% APCE to give the maximum obtainable IPCE. There are various combinations of the physical dimensions, dye loading, and recombination rate constants that can yield a maximum IPCE value. The model can be used to identify which specific conditions are needed to yield maximum IPCE values. For an example, using the fixed model parameters (i.e., dye loading of 2.25 $x10^{-10}/cm^2$ ZnO surface, recombination rate constant of 1000 s^{-1}, m value of 0.7, and a D_{cb} of 0.1 cm^2/s), nanowire arrays with a nanowire radius of 50 nm, nanowire length of 20 μm, and density of 1.45 $x10^{10}$ $/cm^2$ of projected surface area (where surface coverage is ~95%, surface area is ~870 cm^2, and the absorption coefficient is ~1375 cm^{-1}), the IPCE(543nm) is ~100% for a N719 sensitized ZnO nanowire DSSC. Other ideal conditions can yield maximum IPCE values. Moreover, lower dye loadings and faster recombination rates would require greater surfaces areas to yield maximum IPCE results, and vice versa.

Experimentally, we were able to design unique ZnO nanowire based DSSCs that significantly enhanced the overall power conversion efficiency. The first objective was to study the effects of a block layer in the DSSC in efforts of controlling the problem of electron back

transfer. These results showed that the inclusion of a block layer certainly increases the V_{oc}, which ultimately increases the efficiency of ZnO nanowire based DSSCs. In particular, the inclusion of a distinctive hybrid TiO_2/P4VP block layer allowed an increase of efficiency by more than 40 times. The next objective was to form 3D ZnO nanowire arrays to be used in the DSSC. These ZnO nanowire arrays formed unique flower structures and this design was able to effectively enhance the overall power conversion efficiency. Specifically, the five layered 3D structure of ZnO nanowires produced an average efficiency of 1.51%, and with the inclusion of the hybrid block layer that efficiency increased to 2.82%, which is more than 280 times higher than the unmodified 1D ZnO nanowire based DSSC. Lastly, the objective of designing multilayered ZnO nanowire arrays based on ZnO nanofiber seed layers was proven to be the most successful of all the investigated designs. In particular, these arrays formed the unique "caterpillar-like" structures that occurred due to the unique multidirectional growth from the nanofibers. With a unique structure of five layers of ultra dense and multidirectional ZnO nanowires grown from ZnO nanofiber seed layers, an average efficiency of 5.20% was obtained, which is more than 500 times higher than the unmodified 1D ZnO nanowire based DSSC. More importantly, this experimental value of 5.20% is the highest reported value for 3D and/or multidirectional ZnO nanowire-based DSSCs. This significant increase in DSSC performance is contributed to the enhancement of J_{sc} because of the highly dense ZnO NW arrays. Thus, the light harvesting efficiency was enhanced due to the presence of denser arrays of thinner ZnO nanowires, resulting in higher conversion efficiencies.

APPENDIX A: ADSORBED N719 DYE CONCENTRATION

After N719 dye was loaded onto a sample containing an array of 1D ZnO NWs for 1 h, the dye was desorbed into a 5 mL solution of 0.1M NaOH in 50:50 (v/v) of water and ethanol. The 5 mL sample of desorbed N719 in the NaOH solution was collected for absorbance measurements using a UV-Visible Spectrophotometer (Agilent Technologies 8453). Additionally, five known concentrations of N719 dye in solutions of 0.1M NaOH in 50:50 (v/v) of water and ethanol were prepared. These concentrations were 0.001 mM, 0.005 mM, 0.01 mM, 0.025 mM, and 0.05 mM, respectively. These five samples were collected for absorbance measurements as well to generate a calibration curve. The absorbance spectra of all six samples can be found in Figure A.1.

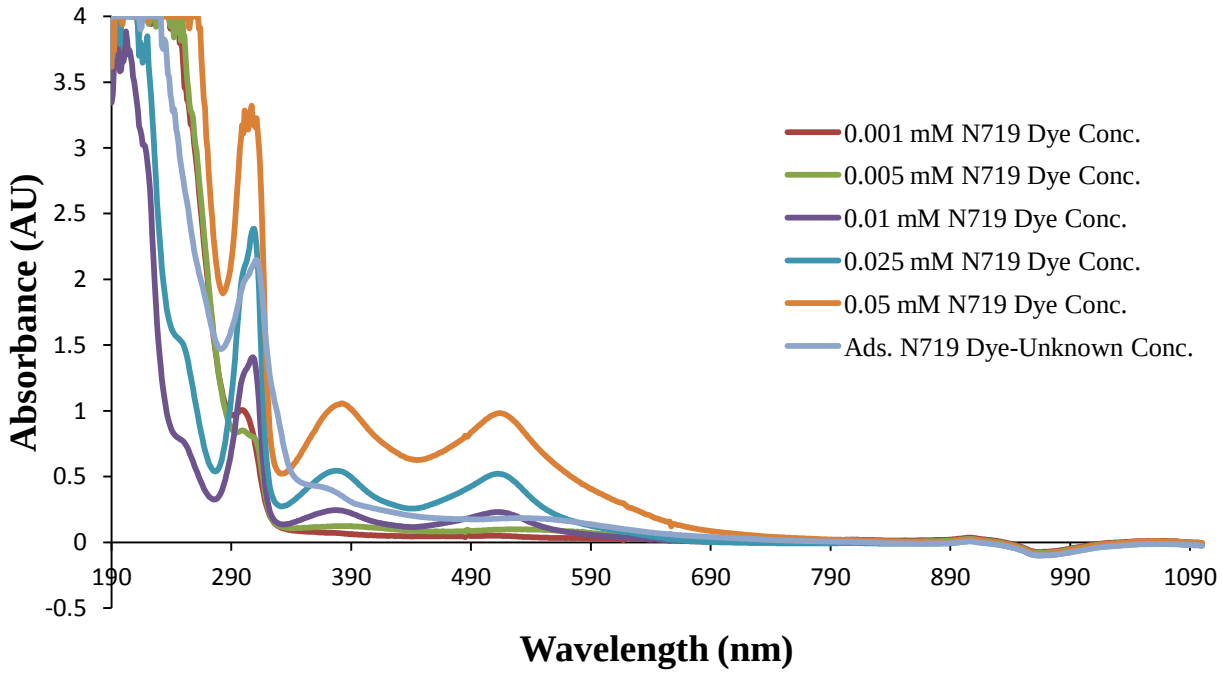

Figure A.1 Absorbance spectra for N719 dye samples.

After analyzing all the data at 190 nm, 305 nm, 377 nm, and 515 nm wavelengths, it was found that the absorbance data at the 515 nm wavelength produced the best linear fit as seen in Figure A.2 below.

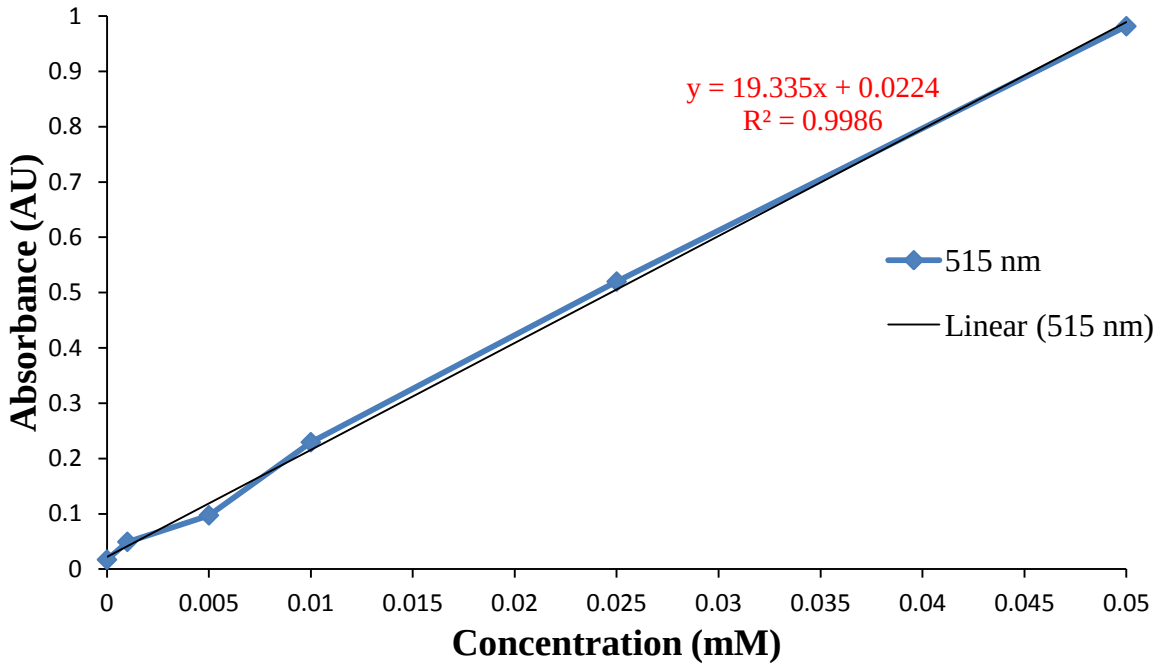

Figure A.2 Calibration curve for N719 dye samples at 515 nm along with the best fit curve.

In literature, most reports of the dye surface concentration are in units of mol/cm^2. For the model, the units of the surface concentration of the N719 dye needed to be M, which is mol dye/volume of ZnO NW array.

Calculating mol dye:

Using the equation of the fitted curve, $y = 19.335x + 0.0224$, we were able to determine the concentration of the unknown sample as $0.0082\ mM$, which equals $8.2x10^{-6}\ M$. Using the volume of our sample, we were able to determine the mol amount of the N719 dye sample.

$$\xrightarrow{yields} \frac{8.2x10^{-6}\,mol}{L} \times 0.005\,L = \underline{4.10x10^{-8}mol\,dye}$$

Calculating surface area of ZnO NW array and Adsorbed N719 Concentration:

$Radius, r = 70\,nm = 7x10^{-6}\,cm;$ $\quad Length, l = 3\,um = 3x10^{-4}\,cm$

$Density, N = 6.35x10^{8}/cm^2;$ $\quad Active\ Area, A_a = 2\,cm^2$

$Surface\ Area_{\ single\ nanowire} = 6\left(\frac{2r}{\sqrt{3}}\right)(r + l)$

$Surface\ Area_{\ NW\ array} = Surface\ Area_{single\ nanowire}\ x\ N\ x\ A_a$

$Surface\ Area_{NW\ aray} = (1.49x10^{-8}cm^2)(6.35x10^{8}/cm^2)(2\,cm^2) = 18.92\,cm^2$

$$Adsorbed\ N719\ Concentration = \frac{4.10x10^{-8}mol\,dye}{18.92cm^2\,ZnO\ NW\ array} = \boxed{2.17x10^{-9}\,mol/cm^2}$$

Calculating volume of ZnO NW array and Adsorbed N719 Concentration:

$Radius, r = 70\,nm = 7x10^{-6}\,cm;$ $\quad Length, l = 3\,um = 3x10^{-4}\,cm$

$Density, N = 6.35x10^{8}/cm^2;$ $\quad Active\ Area, A_a = 2\,cm^2$

$Volume_{\ single\ nanowire} = 2\sqrt{3}\,r^2\,l$

$Volume_{\ NW\ array} = Volume_{single\ nanowire}\ x\ N\ x\ A_a$

$Volume_{NW\ aray} = (6.0x10^{-14}cm^3)(6.35x10^{8}/cm^2)(2\,cm^2) = 7.62x10^{-5}\,cm^3$

$Volume_{NW\ aray} = 7.62x10^{-8}\,L$

$$Adsorbed\ N719\ Concentration = \frac{4.10x10^{-8}mol\,dye}{7.62x10^{-5}\,cm^3\,ZnO\ NW\ array}$$

$$= \boxed{5.38x10^{-4}\,mol/cm^3}$$

$$Adsorbed\ N719\ Concentration = \frac{4.10x10^{-8}mol\,dye}{7.62x10^{-8}\,L\,ZnO\ NW\ array} = \boxed{0.54M}$$

REFERENCES

[1] Tuttle, J.R., *The terawatt challenge.* Power Engineering International, 2005. 13(12): p. 28-30.

[2] Smalley, R., *Future Global Energy Prosperity: The Terawatt Challenge.* MRS Bulletin, 2005. 30: p. 412-417.

[3] Goncalves, L.M., et al., *Dye-sensitized solar cells: A safe bet for the future.* Energy & Environmental Science, 2008. 1(6): p. 655-667.

[4] Crabtree, G.W. and N. Lewis, *Solar Energy Conversion.* Physics Today, 2007. 60(3): p. 37-41.

[5] Lewis, N. *Powering the Plant*, in *Materials Research Society Spring Meeting*. 2007. San Francisco, CA.

[6] Nazeeruddin, M.K., et al., *Combined experimental and DFT-TDDFT computational study of photoelectrochemical cell ruthenium sensitizers.* Journal of the American Chemical Society, 2005. 127(48): p. 16835-16847.

[7] Yella, A., et al., *Porphyrin-Sensitized Solar Cells with Cobalt (II/III)-Based Redox Electrolyte Exceed 12 Percent Efficiency.* Science, 2011. 334(6056): p. 629-634.

[8] Xu, F. and L.T. Sun, *Solution-derived ZnO nanostructures for photoanodes of dye-sensitized solar cells.* Energy & Environmental Science, 2011. 4(3): p. 818-841.

[9] Baxter, J.B. and E.S. Aydil, *Nanowire-based dye-sensitized solar cells.* Applied Physics Letters, 2005. 86: p. 053114-1:3.

[10] Law, M., L.E. Greene, and P. Yang, *Nanowire dye-sensitized solar cells.* Nature Materials, 2005. 4: p. 455-459.

[11] Gao, Y., *Solution-Derived ZnO Nanowire Array Film as Photoelectrode in Dye-Sensitized Solar Cells.* Crystal Growth and Design, 2007. 7(12): p. 2467-2471.

[12] Kaidashev, E.M., et al., *High electron mobility of epitaxial ZnO thin films on c-plane sapphire grown by multistep pulsed-laser deposition.* Applied Physics Letters, 2003. 82(22): p. 3901-3903.

[13] Hendry, E., et al., *Local field effects on electron transport in nanostructured TiO2 revealed by terahertz spectroscopy.* Nano Letters, 2006. 6(4): p. 755-759.

[14] Wang, Z.L., *ZnO nanowire and nanobelt platform for nanotechnology.* Materials Science & Engineering R-Reports, 2009. 64(3-4): p. 33-71.

[15] Ozgur, U., et al., *A comprehensive review of ZnO materials and devices.* Journal of Applied Physics, 2005. 98(4).

[16] Yi, G.C., C.R. Wang, and W.I. Park, *ZnO nanorods: synthesis, characterization and applications.* Semiconductor Science and Technology, 2005. 20(4): p. S22-S34.

[17] Xu, S. and Z.L. Wang, *One-dimensional ZnO nanostructures: Solution growth and functional properties.* Nano Research, 2011. 4(11): p. 1013-1098.

[18] Wan, Q., et al., *Fabrication and ethanol sensing characteristics of ZnO nanowire gas sensors.* Applied Physics Letters, 2004. 84(18): p. 3654-3656.

[19] Wan, Q., et al., *Positive temperature coefficient resistance and humidity sensing properties of Cd-doped ZnO nanowires.* Applied Physics Letters, 2004. 84(16): p. 3085-3087.

[20] Li, Q.H., et al., *Oxygen sensing characteristics of individual ZnO nanowire transistors.* Applied Physics Letters, 2004. 85(26): p. 6389-6391.

[21] Li, Q.H., et al., *Electronic transport through individual ZnO nanowires.* Applied Physics Letters, 2004. 84(22): p. 4556-4558.

[22] Harnack, O., et al., *Rectifying behavior of electrically aligned ZnO nanorods.* Nano Letters, 2003. 3(8): p. 1097-1101.

[23] Keem, K., et al., *Photocurrent in ZnO nanowires grown from Au electrodes.* Applied Physics Letters, 2004. 84(22): p. 4376-4378.

[24] Kind, H., et al., *Nanowire ultraviolet photodetectors and optical switches.* Advanced Materials, 2002. 14(2): p. 158-+.

[25] Ohta, H., et al., *UV-detector based on pn-heteroj unction diode composed of transparent oxide semiconductors, p-NiO/n-ZnO.* Thin Solid Films, 2003. 445(2): p. 317-321.

[26] Ahn, S.E., et al., *Photoresponse of sol-gel-synthesized ZnO nanorods.* Applied Physics Letters, 2004. 84(24): p. 5022-5024.

[27] Park, W.I. and G.C. Yi, *Electroluminescence in n-ZnO nanorod arrays vertically grown on p-GaN.* Advanced Materials, 2004. 16(1): p. 87-+.

[28] Arnold, M.S., et al., *Field-effect transistors based on single semiconducting oxide nanobelts.* Journal of Physical Chemistry B, 2003. 107(3): p. 659-663.

[29] Liu, C.H., et al., *Electrical properties of zinc oxide nanowires and intramolecular p-n junctions.* Applied Physics Letters, 2003. 83(15): p. 3168-3170.

[30] Wang, Y.X., et al., *Fabrication of ZnO nanowire-based diodes and their light-emitting properties.* Acta Physica Sinica, 2008. 57(2): p. 1141-1144.

[31] Johnson, J.C., et al., *Near-field imaging of nonlinear optical mixing in single zinc oxide nanowires.* Nano Letters, 2002. 2(4): p. 279-283.

[32] Weintraub, B., Y.G. Wei, and Z.L. Wang, *Optical Fiber/Nanowire Hybrid Structures for Efficient Three-Dimensional Dye-Sensitized Solar Cells.* Angewandte Chemie-International Edition, 2009. 48(47): p. 8981-8985.

[33] Zhou, J., N.S. Xu, and Z.L. Wang, *Dissolving behavior and stability of ZnO wires iin biofluids: A study on biodegradability and biocompatibility of ZnO nanostructures.* Advanced Materials, 2006. 18(18): p. 2432-+.

[34] Li, Z., et al., *Cellular Level Biocompatibility and Biosafety of ZnO Nanowires.* Journal of Physical Chemistry C, 2008. 112(51): p. 20114-20117.

[35] Ronning, C., et al., *Manganese-doped ZnO nanobelts for spintronics.* Applied Physics Letters, 2004. 84(5): p. 783-785.

[36] Li, S.Y., C.Y. Lee, and T.Y. Tseng, *Copper-catalyzed ZnO nanowires on silicon (1 0 0) grown by vapor-liquid-solid process.* Journal of Crystal Growth, 2003. 247(3-4): p. 357-362.

[37] Gao, P.X., Y. Ding, and Z.L. Wang, *Crystallographic Orientation-Aligned ZnO Nanorods Grown by a Tin Catalyst.* Nano Letters, 2003. 3(9): p. 1315-1320.

[38] Zhao, Q.X., et al., Applied Physics Letters, 2003. 83: p. 165.

[39] Lee, C.J., et al., *Field emission from well-aligned zinc oxide nanowires grown at low temperature.* Applied Physics Letters, 2002. 81(19): p. 3648.

[40] Hsu, H.C., et al., J. Cryst. Growth, 2004. 261: p. 520.

[41] Ma, T., et al., Nanotechnology, 2007. 18: p. 035605.

[42] Xu, S., et al., J. Mater. Res., 2008. 23: p. 2072.

[43] Xu, S., et al., J. Am. Chem. Soc., 2008. 130: p. 14958.

[44] GraceLu, J., P. Chang, and Z. Fan, *Quasi-one-dimensional metal oxide materials-Synthesis, properties and applications.* Materials Science and Engineering R, 2006. 52: p. 49-91.

[45] Greene, L.E., M. Law, and P. Yang, *General route to Vertical ZnO Nanowire arrays using textured ZnO seeds.* Nano Letters, 2005. 5(7): p. 1231-1236.

[46] Chik, H., et al., Appl. Phys. Lett., 2004. 84: p. 3376.

[47] Yan, M., et al., J. Appl. Phys, 2003. 94: p. 5240.

[48] Ng, H.T., et al., Nano. Lett., 2004. 4: p. 1247.

[49] Geng, C., et al., Adv. Funct. Mater., 2004. 14: p. 589.

[50] Wang, X.D., C.J. Summers, and Z.L. Wang, *Large-scale hexagonal-patterned growth of aligned ZnO nanorods for nano-optoelectronics and nanosensor arrays.* Nano Letters, 2004. 4(3): p. 423-426.

[51] Binh, N.T., et al., *Structural and optical properties of ZnO epitaxial films grown on Al2O3 (1120) substrates by metalorganic chemical vapor deposition.* Japanese Journal of Applied Physics Part 1-Regular Papers Short Notes & Review Papers, 2004. 43(7A): p. 4110-4113.

[52] Zhang, B.P., et al., *Formation of highly aligned ZnO tubes on sapphire (0001) substrates.* Applied Physics Letters, 2004. 84(20): p. 4098-4100.

[53] Zhang, B.P., et al., *Low-temperature growth of single-crystalline ZnO tubes on sapphire(0001) substrates.* Applied Physics a-Materials Science & Processing, 2004. 79(7): p. 1711-1714.

[54] Zhang, B.P., et al., *Low-temperature growth of ZnO nanostructure networks.* Journal of Applied Physics, 2004. 96(1): p. 340-343.

[55] Zhang, B.P., et al., *Pressure-dependent ZnO nanocrsytal growth in a chemical vapor deposition process.* Journal of Physical Chemistry B, 2004. 108(30): p. 10899-10902.

[56] Zhang, B.P., et al., *Synthesis and optical properties of single crystal ZnO nanorods.* Nanotechnology, 2004. 15(6): p. S382-S388.

[57] Zhang, B.P., et al., *Epitaxial growth and polarity of ZnO films on sapphire (0001) substrates by low-pressure metal organic chemical vapor deposition.* Japanese Journal of Applied Physics Part 1-Regular Papers Short Notes & Review Papers, 2003. 42(4B): p. 2291-2295.

[58] Guo, M., P. Diao, and S.M. Cai, *Hydrothermal growth of perpendicularly oriented ZnO nanorod array film and its photoelectrochemical properties.* Applied Surface Science, 2005. 249(1-4): p. 71-75.

[59] Greene, L.E., et al., *Low-temperature wafer-scale production of ZnO nanowire arrays.* Angewandte Chemie-International Edition, 2003. 42(26): p. 3031-3034.

[60] Li, Y.H., et al., *I-V characteristics of the p-n junction between vertically aligned ZnO nanorods and polyaniline thin film.* Synthetic Metals, 2010. 160(5-6): p. 499-503.

[61] Govender, K., et al., *Understanding the factors that govern the deposition and morphology of thin films of ZnO from aqueous solution.* Journal of Materials Chemistry, 2004. 14(16): p. 2575-2591.

[62] Trindade, T., J.D.P. Dejesus, and P. Obrien, *PREPARATION OF ZINC-OXIDE AND ZINC-SULFIDE POWDERS BY CONTROLLED PRECIPITATION FROM AQUEOUS-SOLUTION.* Journal of Materials Chemistry, 1994. 4(10): p. 1611-1617.

[63] Chittofrati, A. and E. Matijevic, *UNIFORM PARTICLES OF ZINC-OXIDE OF DIFFERENT MORPHOLOGIES.* Colloids and Surfaces, 1990. 48(1-3): p. 65-78.

[64] Mende, L.S. and J.L. MacManus-Driscoll, *ZnO – nanostructures, defects, and devices.* Materials Today, 2007. 10(5): p. 40-48.

[65] Vayssieres, L., *Growth of arrayed nanorods and nanowires of ZnO from aqueous solutions.* Advanced Materials, 2003. 15(5): p. 464-466.

[66] Vayssieres, L., et al., *Purpose-built anisotropic metal oxide material: 3D highly oriented microrod array of ZnO.* Journal of Physical Chemistry B, 2001. 105(17): p. 3350-3352.

[67] Sun, Y., D.J. Riley, and M.N.R. Ashfold, *Mechanism of ZnO nanotube growth by hydrothermal methods on ZnO film-coated Si substrates.* Journal of Physical Chemistry B, 2006. 110(31): p. 15186-15192.

[68] Greene, L.E., et al., *General route to vertical ZnO nanowire arrays using textured ZnO seeds.* Nano Letters, 2005. 5(7): p. 1231-1236.

[69] Tian, Z.R.R., et al., *Complex and oriented ZnO nanostructures.* Nature Materials, 2003. 2(12): p. 821-826.

[70] Chen, Z.T. and L. Gao, *A facile route to ZnO nanorod arrays using wet chemical method.* Journal of Crystal Growth, 2006. 293(2): p. 522-527.

[71] Boyle, D.S., K. Govender, and P. O'Brien, *Novel low temperature solution deposition of perpendicularly oriented rods of ZnO: substrate effects and evidence of the importance of counter-ions in the control of crystallite growth (vol 15, pg 80, 2002).* Chemical Communications, 2002(15): p. 1651-1651.

[72] Wang, Z., et al., *Large-scale fabrication of tower-like, flower-like, and tube-like ZnO arrays by a simple chemical solution route.* Langmuir, 2004. 20(8): p. 3441-3448.

[73] Zhang, M.L., et al., *Novel preparation of nanosized ZnO-SnO2 with high photocatalytic activity by homogeneous co-precipitation method.* Materials Letters, 2005. 59(28): p. 3641-3644.

[74] Xu, F., et al., *A low-temperature aqueous solution route to large-scale growth of ZnO nanowire arrays.* Journal of Non-Crystalline Solids, 2006. 352(23-25): p. 2569-2574.

[75] Lu, C.H., et al., *Hydrothermal growth of large-scale micropatterned arrays of ultralong ZnO nanowires and nanobelts on zinc substrate.* Chemical Communications, 2006(33): p. 3551-3553.

[76] Verges, M.A., A. Mifsud, and C.J. Serna, *FORMATION OF ROD-LIKE ZINC-OXIDE MICROCRYSTALS IN HOMOGENEOUS SOLUTIONS.* Journal of the Chemical Society-Faraday Transactions, 1990. 86(6): p. 959-963.

[77] Liu, J., et al., *Ultrathin seed-layer for tuning density of ZnO nanowire arrays and their field emission characteristics.* Journal of Physical Chemistry C, 2008. 112(31): p. 11685-11690.

[78] Song, J. and S. Lim, *Effect of seed layer on the growth of ZnO nanorods.* Journal of Physical Chemistry C, 2007. 111(2): p. 596-600.

[79] Xu, C.K., et al., *Preferential Growth of Long ZnO Nanowire Array and Its Application in Dye-Sensitized Solar Cells.* Journal of Physical Chemistry C, 2010. 114(1): p. 125-129.

[80] Greene, L.E., et al., *Solution-grown zinc oxide nanowires.* Inorganic Chemistry, 2006. 45(19): p. 7535-7543.

[81] Baxter, J.B., et al., *Synthesis and characterization of ZnO nanowires and their integration into dye-sensitized solar cells.* Nanotechnology, 2006. 17(11): p. S304-S312.

[82] Becquerel, A.E., *Acad. Sci. Paris*, 1839. 9.

[83] Siemens, W., in *Van Nostrand's Eng. Mag.*1885.

[84] Einstein, A., *Ann. Phys.*, 1905. *17*.

[85] Fuller, C., in *AT&T Archives*. 1953. Warren, NJ.

[86] Chapin, D., in *AT&T Archives*. 1954. Warren, NJ.

[87] Perlin, J., *From Space to Earth: The Story of Solar Electricity*. 2002.

[88] Garnett, E.C. and P. Yang, *Silicon Nanowire Radial p-n junction solar cells.* Journal of American Chemical Society, 2008. 130: p. 9224-9225.

[89] Hoppe, H. and N.S. Sariciftci, *Polymer Solar Cells.* Adv Polym Sci, 2008. 214: p. 1-86.

[90] Kazmerski, L.L., in *National Renewable Energy Laboratory (NREL)*2011: Golden, CO.

[91] Bard, A.J., *Photoelectrochemistry.* Science, 1980. 207: p. 139-144.

[92] Snaith, H.J., et al., *Efficiency Enhancements in Solid-State Hybrid Solar Cells via Reduced Charge Recombination and Increased Light Capture.* Nano Letters, 2007. 7: p. 3372.

[93] Heller, A., Acc. chem. Res., 1981. 14: p. 154-162.

[94] Honda, K. and A. Fujishima, *Electrochemical Photolysis of Water at a Semiconductor Electrode.* Nature, 1972. 238: p. 37-38.

[95] Tufts, B.J., Nature, 1987. 326: p. 681-683.

[96] Licht, S., et al., Nature, 1987. 326: p. 863-864.

[97] Wrighton, M.S., Acc. chem. Res., 1979. 12: p. 303-310.

[98] B.O'Regan and M.Grätzel, *A low-cost, high efficiency solar cell based on dye-sensitized colloidal TiO2 films.* Nature, 1991. 353: p. 737-740.

[99] Jose, R., V. Thavasi, and S. Ramakrishna, *Metal Oxides for Dye-Sensitized Solar Cells.* J. American Ceramic Society, 2009. 92(2): p. 289-301.

[100] Bisquert, J., et al., *Physical chemical principles of photovoltaic conversion with nanoparticulate, mesoporous dye-sensitized solar cells.* J. of Physical Chemistry B, 2004. 108: p. 8106-8118.

[101] Gratzel, M., *Dye-sensitized solar cells.* Journal of Photochemistry and Photobiology C-Photochemistry Reviews, 2003. 4(2): p. 145-153.

[102] Snaith, H. and L. Schmidt-Mende, *Advances in Liquid-Electrolyte and Solid-State Dye-Sensitized Solar Cells.* Advanced Materials, 2007. 19: p. 3187-3200.

[103] Xu, C.K., et al., *Multilayer Assembly of Nanowire Arrays for Dye-Sensitized Solar Cells.* Journal of the American Chemical Society, 2011. 133(21): p. 8122-8125.

[104] Xu, F., et al., *Hierarchical ZnO Nanowire-Nanosheet Architectures for High Power Conversion Efficiency in Dye-Sensitized Solar Cells.* Journal of Physical Chemistry C, 2010. 114(6): p. 2776-2782.

[105] Baxter, J.B. and E.S. Aydil, *Dye-sensitized solar cells based on semiconductor morphologies with ZnO nanowires.* Solar Energy Materials and Solar Cells, 2006. 90(5): p. 607-622.

[106] Wu, M.K., et al., *Performance comparison of dye-sensitized solar cells with different ZnO photoanodes.* Semiconductor Science and Technology, 2011. 26(10).

[107] Guo, M., P. Diao, and S.M. Cai, *Photoelectrochemical properties of highly oriented ZnO nanotube array films on ITO substrates.* Chinese Chemical Letters, 2004. 15(9): p. 1113-1116.

[108] Darling, D. *I-V Curve of a Photovoltaic Device*, Cited 2011-2012; Available from: http://www.daviddarling.info/encyclopedia/I/AE_I-V_curve.html.

[109] Martinson, A.B.F., et al., *Electron Transport in Dye-Sensitized Solar Cells Based on ZnO Nanotubes: Evidence for Highly Efficient Charge Collection and Exceptionally Rapid Dynamics.* Journal of Physical Chemistry A, 2009. 113(16): p. 4015-4021.

[110] Kroon, J.M., et al., *Nanocrystalline dye-sensitized solar cells having maximum performance.* Progress in Photovoltaics, 2007. 15(1): p. 1-18.

[111] Wang, Z.S., et al., *Significant influence of TiO2 photoelectrode morphology on the energy conversion efficiency of N719 dye-sensitized solar cell.* Coordination Chemistry Reviews, 2004. 248(13-14): p. 1381-1389.

[112] Wang, P., et al., *A high molar extinction coefficient sensitizer for stable dye-sensitized solar cells.* Journal of the American Chemical Society, 2005. 127(3): p. 808-809.

[113] Nazeeruddin, M.K., et al., *Synthesis of novel ruthenium sensitizers and their application in dye-sensitized solar cells.* Coordination Chemistry Reviews, 2005. 249(13-14): p. 1460-1467.

[114] Giannouli, M. and F. Spiliopoulou, *Effects of the morphology of nanostructured ZnO films on the efficiency of dye-sensitized solar cells.* Renewable Energy, 2011.

[115] Lu, L., et al., *Effects of annealing conditions on the photoelectrochemical properties of dye-sensitized solar cells made with ZnO nanoparticles.* Solar Energy, 2010. 84(5): p. 844-853.

[116] Weintraub, B. *One Dimensional Zinc Oxide Nanomaterials Synthesis and Photovoltaic Applications*, in *Materials Science and Engineering*. 2010. Atlanta, GA: Georgia Institute of Technology.

[117] *Photoresist: SPECIALTY COATING SYSTEMS / SCS P 6000*, Cited 2012; Available from: http://www.caeonline.com/listing/product/130115/specialty-coating-systems-scs-p-6000.

[118] *VWR Scientific 1400E Benchtop Vacuum Oven*, Cited 2012; Available from: http://www.bid-on-equipment.com/detail~id~81191.htm.

[119] *Fisher Scientific Isotemp Programmable Muffle Furnaces*, Cited 2012; Available from: https://new.fishersci.com/ecomm/servlet/fsproductdetail?tab=Items&productId=623148&fromSearch=&highlightProductsItemsFlag=null&crossRefPartNo=null&crossRefData=null&catlogId=29104&catCode=RE_SC&&storeId=10652.

[120] Nazeeruddin, M.K., et al., *CONVERSION OF LIGHT TO ELECTRICITY BY CIS-X2BIS(2,2'-BIPYRIDYL-4,4'-DICARBOXYLATE)RUTHENIUM(II) CHARGE-TRANSFER SENSITIZERS (X = CL-, BR-, I-, CN-, AND SCN-) ON NANOCRYSTALLINE TIO2 ELECTRODES.* Journal of the American Chemical Society, 1993. 115(14): p. 6382-6390.

[121] Schlichthorl, G., N.G. Park, and A.J. Frank, *Evaluation of the charge-collection efficiency of dye-sensitized nanocrystalline TiO2 solar cells.* Journal of Physical Chemistry B, 1999. 103(5): p. 782-791.

[122] Penny, M., T. Farrell, and G. Will, *A mathematical model for the anodic half cell of a dye-sensitised solar cell.* Solar Energy Materials and Solar Cells, 2008. 92(1): p. 24-37.

[123] Barnes, P.R.F., et al., *Simulation and measurement of complete dye sensitised solar cells: including the influence of trapping, electrolyte, oxidised dyes and light intensity on steady state and transient device behaviour.* Physical Chemistry Chemical Physics, 2011. 13(13): p. 5798-5816.

[124] Hill, J.J., et al., *An Interfacial and Bulk Charge Transport Model for Dye-Sensitized Solar Cells Based on Photoanodes Consisting of Core-Shell Nanowire Arrays.* Journal of the American Chemical Society, 2011. 133(46): p. 18663-18672.

[125] Hamann, T.W., et al., *Advancing beyond current generation dye-sensitized solar cells.* Energy & Environmental Science, 2008. 1(1): p. 66-78.

[126] *Calculate Volume of Hexagonal Prism*, Cited 2012; Available from: http://www.aqua-calc.com/calculate/volume-hexagonal-prism.

[127] *Radius of Regular Polygon*, Cited 2012; Available from: http://www.mathopenref.com/polygonradius.html.

[128] Cited 2012; Available from: http://etc.usf.edu/clipart/43100/43123/prism-hex1_43123.htm.

[129] Barnes, P.R.F., et al., *Electron Injection Efficiency and Diffusion Length in Dye-Sensitized Solar Cells Derived from Incident Photon Conversion Efficiency Measurements.* Journal of Physical Chemistry C, 2009. 113(3): p. 1126-1136.

[130] Ong, K.G., et al., *Application of finite-difference time domain to dye-sensitized solar cells: The effect of nanotube-array negative electrode dimensions on light absorption.* Solar Energy Materials and Solar Cells, 2007. 91(4): p. 250-257.

[131] Fisher, A.C., et al., *Intensity dependence of the back reaction and transport of electrons in dye-sensitized nanacrystalline TiO2 solar cells.* Journal of Physical Chemistry B, 2000. 104(5): p. 949-958.

[132] Wong, D.K.P., et al., *Enhancing Electron Collection Efficiency and Effective Diffusion Length in Dye-Sensitized Solar Cells.* Chemphyschem, 2009. 10(15): p. 2698-2702.

[133] Quintana, M., et al., *Comparison of dye-sensitized ZnO and TiO2 solar cells: Studies of charge transport and carrier lifetime.* Journal of Physical Chemistry C, 2007. 111(2): p. 1035-1041.

[134] Martinson, A.B.F., et al., *Dynamics of charge transport and recombination in ZnO nanorod array dye-sensitized solar cells.* Physical Chemistry Chemical Physics, 2006. 8(40): p. 4655-4659.

[135] Zu, X.H., et al., *In situ fabrication of ordered nanoring arrays via the reconstruction of patterned block copolymer thin films.* Chemical Communications, 2010. 46(42): p. 7927-7929.

[136] Kavan, L. and M. Gratzel, *HIGHLY EFFICIENT SEMICONDUCTING TIO2 PHOTOELECTRODES PREPARED BY AEROSOL PYROLYSIS.* Electrochimica Acta, 1995. 40(5): p. 643-652.

[137] Sun, K., et al., *Solution Synthesis of Large-Scale, High-Sensitivity ZnO/Si Hierarchical Nanoheterostructure Photodetectors.* Journal of the American Chemical Society, 2010. 132(44): p. 15465-15467.

[138] Ko, S.H., et al., *Nanoforest of Hydrothermally Grown Hierarchical ZnO Nanowires for a High Efficiency Dye-Sensitized Solar Cell.* Nano Letters, 2011. 11(2): p. 666-671.

[139] Li, Y., J. Gong, and Y. Deng, *Hierarchical structured ZnO nanorods on ZnO nanofibers and their photoresponse to UV and visible lights.* Sensors and Actuators A: Physical, 2010. 158(2).

VITA
MALLARIE D. MCCUNE

MCCUNE was born on March 23, 1984 in McComb, MS. She attended public schools in Jackson, MS and graduated Valedictorian of her Senior Class at William B. Murrah High School. She went on to pursue a dual degree program through the Atlanta University Center; she received a B.S. in Chemistry from Spelman College, Atlanta, Georgia and a B.S. in Chemical Engineering from Georgia Institute of Technology, Atlanta, GA in 2007. She continued her studies at Georgia Tech where she then pursued a doctorate in Chemical and Biomolecular Engineering. When she is not working on her research, Ms. McCune enjoys spending quality time with her family, acting, writing songs and poetry, and performing various forms of dance.